

Opto-electrical modelling of CIGS solar cells

Rezaei, Nasim

DOI

[10.4233/uuid:952c6c51-911b-4bab-a844-af23210dcfcf](https://doi.org/10.4233/uuid:952c6c51-911b-4bab-a844-af23210dcfcf)

Publication date

2020

Document Version

Final published version

Citation (APA)

Rezaei, N. (2020). *Opto-electrical modelling of CIGS solar cells*. [Dissertation (TU Delft), Delft University of Technology]. <https://doi.org/10.4233/uuid:952c6c51-911b-4bab-a844-af23210dcfcf>

Important note

To cite this publication, please use the final published version (if applicable).
Please check the document version above.

Copyright

Other than for strictly personal use, it is not permitted to download, forward or distribute the text or part of it, without the consent of the author(s) and/or copyright holder(s), unless the work is under an open content license such as Creative Commons.

Takedown policy

Please contact us and provide details if you believe this document breaches copyrights.
We will remove access to the work immediately and investigate your claim.

Opto-electrical Modelling of CIGS Solar Cells

Nasim REZAEI

Opto-electrical Modelling of CIGS Solar Cells

Proefschrift

ter verkrijging van de graad van doctor
aan de Technische Universiteit Delft,
op gezag van de Rector Magnificus Prof. dr. ir. T.H.J.J. van der Hagen,
voorzitter van het College voor Promoties,
in het openbaar te verdedigen op
Maandag 5 October 2020 om 12:30 uur

door

Nasim REZAEI

Master of Electrical Engineering, Shiraz University, Iran
geboren te Jahrom, Iran

This dissertation has been approved by the promotor:

Prof.dr. M. Zeman

promotor:

Dr.ir. O. Isabella

Composition of the doctoral committee:

Rector Magnificus

chairperson

Prof.dr. M. Zeman

Technische Universiteit Delft, promotor

Dr.ir. O. Isabella

Technische Universiteit Delft, promotor

Independent members:

Prof.dr. A. Weeber

Technische Universiteit Delft

Prof.dr. M. Schmid

University of Duisburg-Essen, Germany

Prof.dr. M. Topič

University of Ljubljana, Slovenia

Prof.dr. B. Vermang

University of Hasselt, Belgium / imec, Belgium

Dr. Z. Vroon

TNO-Brightlands Materials Center, TNO

Prof.dr. A.H.M. Smets

Technische Universiteit Delft, reserve member



ISBN: 978-94-6384-161-0

Copyright © 2020 N. Rezaei

All rights reserved. No part of this publication may be reproduced, stored in a retrieval system, or transmitted in any form or by any means without the prior written permission of the copyright owner.

Printed by *Ipskamp Printing*, the Netherlands.

To my parents

"Nothing in life is to be feared, it is only to be understood. Now is the time to understand more, so that we may fear less."

Marie Curie

Contents

1	Introduction	1
1.1	The photovoltaic effect	2
1.1.1	p - n junctions and solar cells	3
1.1.2	Direct and indirect bandgap semiconductors	5
1.2	Absorber categories	6
1.2.1	Wafer-based solar cells	6
1.2.2	Thin-film solar cells	7
1.3	CIGS solar cells	7
1.3.1	State of the art	8
1.3.2	Structure of CIGS solar cells	10
1.3.3	Optical losses	13
1.3.4	Electrical losses	15
1.4	Aim and scope of this thesis	16
1.5	Outline	16
1.6	Main contributions to the field	17
2	Modelling Approaches	19
2.1	Introduction	19
2.2	Solar cell characteristics	19
2.2.1	Current density versus voltage curve	19
2.2.2	The external quantum efficiency	20
2.3	Optical limits	21
2.4	Optical simulation tools	22
2.4.1	Finite-difference time domain (FDTD) method	23
2.4.2	Rigorous coupled wave analysis (RCWA)	24
2.4.3	Finite integration technique (FIT)	24
2.4.4	Transfer matrix method (TMM)	24
2.4.5	Net-radiation method	25
2.4.6	Finite element method (FEM)	25
2.5	Electrical simulation tools	27
3	Quenching Mo optical losses in CIGS solar cells by a point contacted dual-layer dielectric spacer: a 3-D optical study	29
3.1	Introduction	30
3.2	Optical modelling	30
3.3	Results and discussion	33
3.3.1	Nature of the optical losses at the back contact	33
3.3.2	Synthetic dielectric spacer	34
3.3.3	Al_2O_3 vs MgF_2	36
3.3.4	Electric field investigation	39
3.3.5	Point contact optimization	40
3.4	Conclusions	43

4	A multi-layer wideband antireflection coating	45
4.1	Introduction	46
4.2	Methodology	48
4.3	Contribution of the front reflectance in optical losses	49
4.4	Optical optimization of ARC with reflectance as the cost function	50
4.4.1	Optimum combination of ARC properties for maximum photo-generated current density	50
4.4.2	Optimum combination of ARC properties for maximum photo-generated current density	54
4.4.3	Single- or double-layer ARC?	55
4.5	Improvement of optical performance in the whole incident spectrum	56
4.6	Conclusions and outlook	57
5	IBC CIGS solar cells, Part I: optical study	61
5.1	Introduction	62
5.2	Modelling platform	62
5.3	Results and discussion	63
5.3.1	Design considerations	63
5.3.2	IBC solar cells with antireflective front textures	64
5.3.3	IBC solar cell with as-grown absorber morphology	65
5.4	conclusions	67
6	IBC CIGS solar cells, Part II: opto-electrical study	69
6.1	Introduction	70
6.2	Modelling approach	70
6.3	Model calibration	71
6.4	IBC design considerations	72
6.5	Results and discussion	74
6.5.1	TCO width	74
6.5.2	Absorber thickness	75
6.5.3	Bandgap grading	76
6.5.4	TCO coverage	77
6.5.5	Bulk trap density in CIGS	78
6.5.6	Gap width	79
6.5.7	Optimal IBC vs reference FBC	80
6.6	Conclusion	81
7	Conclusion and Outlook	83
7.1	Conclusions	83
7.2	Outlook	85
	Bibliography	87
	Acknowledgments	107
	List of Publications	109

Curriculum Vitae

111

Summary

One of the key approaches to slow down and eventually prevent dramatic climate change is direct electricity generation from sunlight. Thin-film copper indium gallium (di)selenide (CIGS) is an excellent candidate for highly efficient and stable solar cells. A tuneable and direct bandgap as well as a high absorption coefficient allow for CIGS solar cells to be nearly 100 times thinner than their crystalline silicon (c-Si) counterparts; a feature suitable for flexible photovoltaic (PV) applications. In this thesis, light management for sub-micron CIGS solar cells is studied with the help of opto-electrical simulations.

In Chapter 2, the theoretical optical limits for CIGS solar cells as well as the various available opto-electrical modelling platforms are briefly discussed. We study the Green absorption benchmark as a function of thickness and bandgap. Our modelling tools of choice, namely Ansys HFSS for the optical simulations, and Sentaurus TCAD for the electrical simulations are introduced in more details.

The interface between CIGS and molybdenum (Mo) back contact is subject to a considerable amount of optical and electrical loss. This issue is investigated in Chapter 3, where we firstly discuss the plasmonic nature of the optical losses. Later, we introduce a double-layer dielectric spacer consisting of MgF_2 and Al_2O_3 with periodic point contacts to quench the Mo-associated losses. We optimize the spacer thickness and the point contact area coverage for maximal photo-current density (J_{ph}) in a CIGS solar cell with 750-nm thick absorber.

The front reflection losses, contributing to roughly 10% of optical losses, are addressed in Chapter 4. We show that an MgF_2 -based double-layer porous-on-compact anti-reflection coating (ARC) allows for gradual refractive index change from air to CIGS and, therefore, according to the Rayleigh effect leads to a wideband anti-reflection effect. This is done by means of Bruggemann's effective medium approximation and sequential nonlinear programming (SNLP) for the optimization process. Our models suggest that the proposed ARC surpasses the conventional single-layer ARC in resiliency against angle of incidence. A hybrid light management, employing both the suggested ARC at the front side and $\text{MgF}_2 / \text{Al}_2\text{O}_3$ dielectric spacer at the rear side, proves to increase J_{ph} of a 750-nm thick CIGS solar cell beyond that of a 1600-nm thick absorber (without light management).

In the rest of the thesis, we take an approach beyond the state-of-the-art architecture of CIGS solar cells and, for the first time, introduce the inter-digitated back-contacted (IBC) structure for CIGS technology. This structure, which no longer suffers from parasitic absorption (associated with the buffer and window layers), is optically studied in Chapter 5. We compare the results with a reference front- and back-contacted (FBC) solar cell with the same absorber volume, and take the Green limit as the benchmark. Two ARC schemes are studied; (i) high-aspect ratio features at the front side of the absorber and, (ii) the as-grown CIGS morphology with optimized $\text{MgF}_2 / \text{Al}_2\text{O}_3$ layers.

Once the optical potential of the IBC CIGS solar cells is realized, we continue our studies with an opto-electrical analysis in TCAD Sentaurus environment (Chapter 6).

We not only optimize the geometry of electron- and hole-contacts, the gap between them and the contacts' period, but also, study the CIGS bandgap grading and its defect density. The electric field map around the gap region is used to highlight the importance of electrical passivation in achieving a high performance. Our models (calibrated with real FBC solar cells fabricated at Solliance at the High-tech campus in Eindhoven) show the high potential of IBC CIGS solar cells for high efficiency PV applications.

Samenvatting

Dutch translation by Thierry de Vrijer

Een van de belangrijkste manieren om drastische klimaatveranderingen te voorkomen is door elektriciteit op te wekken direct uit zonlicht. Dunne film Koper Indium Gallium (di)Selenide (CIGS) is een uitstekende kandidaat voor stabiele zonnecellen met hoge efficiëntie. Een bandgap die afstembaar is in combinatie met een hoge absorptie coëfficiënt zorgen ervoor dat een CIGS-zonnecel bijna 100x dunner kan zijn in vergelijking met gelijksoortige kristallijn Silicium zonnecellen; een eigenschap die CIGS geschikt maakt voor flexibele applicaties. In dit proefschrift is het manipuleren van licht voor sub-micron CIGS-zonnecellen bestudeerd met behulp van opto-elektrische simulaties.

In Hoofdstuk 2 worden de theoretische optische limieten voor CIGS-zonnecellen kort besproken, evenals de verscheidene beschikbare opto-elektrische modelleerplatforms. We bestuderen de Green-absorptie benchmark als een functie van de dikte en de bandgap. Ons gekozen modelleerplatform, namelijk Ansys HFSS voor optische simulaties en Sentaurus TCAD voor elektrische simulaties, worden in meer detail geïntroduceerd.

De interface tussen CIGS en de Molybdenum (Mo) achtercontact is de locatie van aanzienlijke optische en elektrische verliezen. Dit probleem is onderzocht in Hoofdstuk 3, waar we eerst de plasmonische aard van de optische verliezen bespreken. Vervolgens introduceren we een dubbellaags diëlektrische afstandhouder, bestaande uit MgF_2 en Al_2O_3 , met periodische puntcontacten om de Mo-gerelateerd verliezen te verminderen. We optimaliseren de dikte van de afstandhouder en de dekkingsgraad van de puntcontacten om maximale foto-stroomdichtheid (J_{ph}) te bereiken in een CIGS-zonnecel met een 750 nm dikke absorptie-laag.

De reflectie verliezen aan de voorzijde, die voor ongeveer 10% bijdragen aan de optische verliezen, worden besproken in Hoofdstuk 4. Wij laten zien dat een dubbellaags anti-reflectie coating (ARC), gebaseerd op een poreuze laag op een compacte laag MgF_2 , een geleidelijke brekingsindex verandering van lucht naar CIGS bewerkstelligt, wat volgens het Rayleigh-principe leidt tot een breedband anti-reflectie effect. Dit is bereikt door middel van de Bruggemann's effectieve gemiddelde benadering en sequentieel non-lineair programmeren (SNLP). Ons model suggereert dat de voorgestelde ARC de conventionele enkellaags ARC overtreft in dat hij minder afhankelijk is van de invalshoek. Een hybride licht manipulatie benadering, die gebruik maakt van de voorgestelde ARC aan de voorzijde en de $\text{MgF}_2/\text{Al}_2\text{O}_3$ diëlektrische afstandhouder aan de achterzijde, verhoogt de J_{ph} van een 750-nm dikke CIGS-zonnecel ten opzichte van de J_{ph} van een 1600 nm dikke absorptie-laag (zonder licht manipulatie).

In de rest van dit proefschrift nemen we een buiten-de-gebaande-paden benadering voor het ontwerp van een CIGS-zonnecel en, voor de eerst keer, introduceren we de "interdigitated back-contacted" (IBC) structuur voor de CIGS-technologie. Deze structuur, die geen hinder ondervindt van parasitaire absorptie verliezen, is optisch bestudeerd in Hoofdstuk 5. We vergelijken de resultaten met een referentie cel met contacten aan de voor- en achterzijde (FBC) met dezelfde absorptie-laag volume en

gebruiken de Green-limiet als benchmark. Twee ARC-ontwerpen zijn bestudeerd, (i) een ontwerp met elementen aan de voorzijde met een hoog aspectverhouding en (ii) de natuurlijke morfologie van de CIGS laag met geoptimaliseerde $\text{MgF}_2/\text{Al}_2\text{O}_3$ lagen.

Als de optische potentie van IBC CIGS zonnecellen eenmaal is gerealiseerd, gaan we door met de opto-elektrische analyse in de TCAD Sentaurus omgeving (Hoofstuk 6). We optimaliseren niet alleen de geometrie van de elektron- en gat-contacten, met name de opening tussen de contacten en de periode, maar bestuderen ook het graderen van de CIGS bandgap en de defect-dichtheid. Een map van het elektrische veld rond het bandgap-gebied is gebruikt om het belang van de elektrische passivatie te belichten om een hoge prestatie te bereiken. Onze modellen (gekalibreerd met echte FBC zonnecellen gefabriceerd door Solliance op de High-tech campus in Eindhoven) tonen de grote potentie aan voor IBC CIGS zonnecellen voor hoog-efficiënte PV applicaties.

1

Introduction

One of the most important challenges of our time is the ever growing demand for energy. Almost exponential population growth together with increasing energy consumption per capita are challenging the world's energy production capabilities as never before [1], [2]. According to the BP Statistical Review of World Energy from 2019, "Primary energy consumption grew at a rate of 2.9% last year, almost double its 10-year average of 1.5% per year, and the fastest since 2010" [3]. So far, the main source of energy production has been the burning of fossil fuels, such as oil, gas and coal, accounting for 79.7% of total final energy consumption in the year 2017 [4]. As a result, the amount of greenhouse gas emissions has experienced an unprecedented increase and has led to inevitable climate change and global warming, according to several independent reports [5], [6]. Not only causes the burning of limited resources environmental problems in form of climate change, but it is also a main factor in today's geopolitical tensions in oil- and gas-rich parts of the world. In this respect, renewable, abundant and cleaner sources of energy such as solar and wind energy, biogas and hydropower are increasingly used to reduce the greenhouse emissions. Furthermore, the combination of renewable energy sources has the high potential to enable countries with limited access to fossil fuels, to become more independent in their energy production. Solar energy is of particular interest, as it is the most abundant renewable source of energy. Although only a fraction of the sun's energy can be harnessed on earth, it amounts to significantly more than the global annual energy consumption [7]. One way to harness solar energy is to generate electrical power, by converting the incident solar irradiation into electricity, using photovoltaic (PV) technology. In the race between renewable energy sources and fossil fuels, policy management, cost reduction and public awareness play a key role. Recently, the cost of useful energy generated by PV technology has become competitive to and in some cases cheaper than that of fossil fuels [4]. In 2018, the highest installed renewable power capacity (100 GW) belonged to PV technology, followed by wind power technology. This is due to the fact that, compared to other renewable technologies such as hydropower, the levelized cost of electricity (LCOE)¹ from PV and wind power technologies is becoming more and more competitive to that of fossil fuels [4]. The thesis at hand is focusing on further improvement of PV technology, with the emphasis on copper indium gallium (di)selenide (CIGS) solar cells.

¹LCOE defines the cost of electricity produced by a power generation facility in the units of cost per kWh [8].

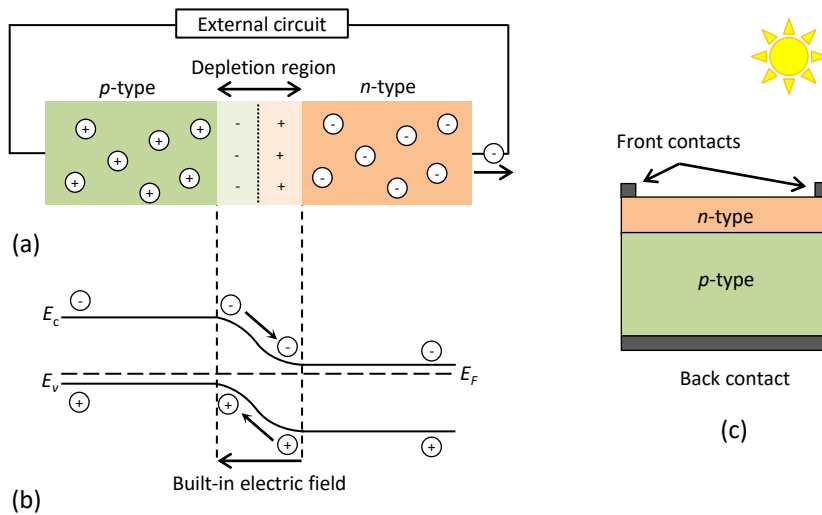


Figure 1.1: a) Charge distribution in a p - n junction and the formation of an electric field in the depletion region due to the presence of ionized atoms on both sides of the junction, b) the corresponding band diagram, and c) schematic of a typical solar cell structure.

1.1 The photovoltaic effect

A solar cell, a simple schematic structure of which is illustrated in Figure 1.1, is an electronic device that directly converts incident light into electricity. Upon illumination of light on the solar cell it produces an electric potential difference (voltage) and a current, provided that its electrodes are connected to each other via an external circuit. The underlying working principle of solar cells is the so-called photovoltaic effect, which describes the conversion of light (photons) into a voltage across a junction between two dissimilar materials. It consists of the following steps: i) the absorption of photons in an absorber material (typically, a semiconductor) and generation of mobile charge carriers, ii) separation of the photo-generated charge carriers and iii) their collection at the terminals of the solar cell to generate electricity. These steps are explained in more detail below. The photovoltaic effect, like many other scientific breakthroughs, was discovered rather accidentally in 1839 by Edmond Becquerel. He noticed that the voltage produced by his electro-chemical cells increased by exposure to sunlight [9].

In an ideal semiconductor at absolute zero temperature ($T = 0$ K), electrons are typically bound to their corresponding atoms and cannot contribute to any charge transport. The range of energy levels that electrons can have in a solid are described by the *energy band model*. In this model, the energy of the outermost (with respect to the atom's nucleus) electrons that are bonded to the neighbouring atoms is represented by allowed energy states in the so-called valence band. These electrons are called valence electrons. In order to transport electrical charge across a certain structure, electrons that are free from bonding states are required, which can move between

atoms. The energy levels of such free electrons form the conduction band in the energy band model. In a typical semiconductor, valence band and conduction band are separated from each other by a certain amount of energy, which is called bandgap (Figure 1.2). Since ideally, there are no available energy states between the valence band maximum and the conduction band minimum, the energy gap between them is known as the forbidden gap. In order for a valence electron to break from its bonding state, leave the bound state of its atom and become a free electron (a conduction electron, according to this model), this electron needs to absorb additional energy as high as the bandgap energy. Einstein's remarkable achievement was, to define light into finite energy quanta, discrete states of energy, which are called photons [10]. Each photon has an energy $E = h\nu$ (h is Plank's constant and ν is the frequency). Photons with energy larger than the bandgap of a semiconductor material can give enough energy to electrons to leave the valence band and become free electrons. This process leaves a missing electron – a so-called hole – in the valence band, which despite not being a particle, displays the physical properties of such, and has a positive electronic charge. Holes are denoted as empty energy states in the valence band in the energy band model. The generation of electron-hole pairs is shown in Figure 1.2. If the energy of the incident photon is larger than the bandgap, the electron will initially be excited to an energy level higher than the conduction band minimum. The excited electron will then lose its excess energy (the energy difference between the photon energy and the bandgap) as heat in a process called thermalization and reaches a relaxed energy state at conduction band minimum. When a free electron refills a bonding state in the valence band, in other words, when a conduction electron takes the available energy state of a hole in the valence band (see Figure 1.2), this process is called recombination. Recombination leads to radiative or non-radiative emission of the extra energy, depending on the arrangement of atoms in the semiconductor material. The typical time a charge carrier (electron or hole) survives before recombining with the opposite charge carrier is called lifetime. Lifetime is related to diffusion length, which is the typical length in the semiconductor that each charge carrier travels before recombination.

In solar cells, it is desired that the recombination of photo-generated charge carriers occurs not in the bulk of the solar cell, but after the free electrons have moved through the external circuit (participated in electrical current) and reached the other side of the solar cell (see Figure 1.1). For this reason, solar cells are designed such that electrons and holes are separated from each other by semipermeable membranes, meaning that each charge carrier flows towards a different membrane to reach its corresponding contact and participate in electrical current. Such separation that reduces the chance of recombination before extraction of charge carriers at the contacts is facilitated by forming a so-called *p-n* junction and will be explained in the following section.

1.1.1 *p-n* junctions and solar cells

It is instructive to first introduce the concept of doping in semiconductors. In intrinsic semiconductors at temperatures higher than 0 K, some of the valence band electrons may gain sufficient thermal energy by interactions with the vibrations of the atoms in the semiconductor material to be excited to the conduction band, a phenomenon

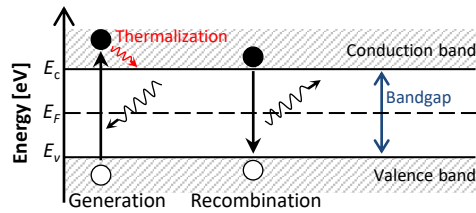


Figure 1.2: Schematic representation of carrier generation and recombination. Black and white circles represent electrons and holes, respectively. E_c and E_v and E_F are the energies of the conduction band minimum and valence band maximum and Fermi level, respectively.

known as thermal excitation. In this case, electrons and holes have an equal concentration, a value that at 300 K is known as intrinsic carrier concentration and is measured in units of $1/\text{cm}^3$. For example, the charge carrier concentration of intrinsic crystalline silicon is about $1.5 \times 10^{10} 1/\text{cm}^3$. It is also worth noting that the Fermi energy level² of the intrinsic semiconductors is almost in the middle of the forbidden gap [11], as can be seen in Figure 1.2. The carrier concentration of semiconductors can be manipulated by adding impurity atoms to them. The process of substituting some of the intrinsic atoms of a semiconductor with impurity atoms that have different number of valence band electrons is called doping. This process is done to increase the concentration of one of the charge carriers, electrons or holes. If the impurity atoms have more (less) valence band electrons than the intrinsic semiconductor, the doping is *n*-type (*p*-type) and electrons (holes) are majority charge carriers in the resulting material. In doped semiconductors, the Fermi energy is not nearly in the middle of the forbidden gap, but instead, is located closer to the conduction band minimum energy for *n*-type and to the valence band maximum energy for *p*-type materials, as shown in the energy band diagram (or simply, band diagram) in Figure 1.1(b).

As mentioned before, the separation of the charge carriers is facilitated by forming a *p-n* junction between an *p*-doped and a *n*-doped semiconductor, as shown in Figure 1.1. The *p-n* junction between the same materials with different types of doping is called a homojunction (the case of Figure 1.1). On the contrary, a heterojunction is formed between two different materials, for instance between *p*-type CIGS and *n*-type Cadmium sulfide (CdS). Regardless, the formation of the *p-n* junction results in charge carrier diffusion, due to the difference in the concentration of free charge carriers on both sides of the junction as shown in Figure 1.1. Electrons will diffuse from the *n*-type to the *p*-type material and likewise, holes will leave the *p*-type semiconductor for the *n*-type side of the junction. This disturbs the charge neutrality in the regions, which are being depleted from the majority charge carriers and leads to the formation of a built-in electric field, driving the charge carriers in two opposite directions and acting against the diffusion of charge carriers. This electric field is illustrated by the slope

²The Fermi energy level, or simply Fermi level, which represents the electrochemical potential of the electrons, is a hypothetical energy level that has a 50% probability of being occupied by an electron at any time in thermodynamic equilibrium [8].

of the conduction band minimum and valence band maximum in the band diagram in Figure 1.1. Since almost no free carriers are present in this part of the junction, it is called *depletion region* or *space charge region*. Upon light illumination, excess electrons and holes are generated in the semiconductor, increasing the concentration of the minority charge carriers in both sides of the *p-n* junction. These photo-generated electrons and holes are driven under the influence of the built-in electric field to the *n*-doped and the *p*-doped regions, respectively, where they become majority charge carriers and the chance of recombination is reduced. Now, these charge carriers can move towards the corresponding contacts, where they can contribute to the current in an external circuit as depicted in Figure 1.1(a).

A simplified solar cell structure is shown in Figure 1.1(c). In this context, the light-facing side of the solar cell is known as the *front side*. The electrons are driven to the front metallic grid, whereas the hole are driven to and collected at the metallic contact at the *back side*. Albeit in reality, solar cells consist of more layers and materials, in order to achieve high output power. The abovementioned schematic serves only as a tool to visualize the concept of electricity generation by solar cells.

1.1.2 Direct and indirect bandgap semiconductors

A brief introduction on crystalline materials is helpful for further discussions on semiconductors. Generally speaking, in a crystal, atoms are bonded in a periodic and ordered manner. It is such order and periodicity that gives different materials their individual properties, such as bandgap and electric conductivity. A crystal lattice or unit cell is the smallest arrangement of atoms that is repeated throughout the whole crystal. Unit cells can have different shapes, including and not limited to diamond cubic, zincblende and Wurtzite [11]. Silicon for example, crystallizes in a diamond cubic structure. Most important semiconductors crystallize in a diamond or zincblende form [11]. The energy of an electron in a semiconductor crystal is dependent on its momentum. This dependency is usually illustrated in the energy dispersion diagram, an example of which can be seen in Figure 1.3.

Depending on the crystal structure, a semiconductor material can have a *direct* or *indirect* bandgap. It has a direct bandgap if the valence band maximum and conduction band minimum have the same crystal momentum (Figure 1.3(a)). Otherwise, the material has an indirect bandgap (Figure 1.3(b)). In indirect bandgap semiconductors, an electron cannot shift from a valence band maximum energy state to a conduction band minimum energy state without a change in momentum. This means that the electron must give or receive momentum to/from the vibrations of the crystal lattice to be able to reach the conduction band energy state and become a free electron [11]. Lattice vibrations can also be described as phonons, quanta of vibration modes. Therefore, in an indirect bandgap material, an electron shifts from the valence band to the conduction band via absorbing energy from a photon and exchanging a phonon with the crystal lattice. The same principle applies to the recombination process: a free electron in an indirect bandgap material must both emit a photon and exchange a phonon with the crystal lattice in order to recombine with a hole in the valence band. In direct bandgap materials however, no exchange of momentum between the electron and the lattice vibrations is required for electron-hole pair generation. As a

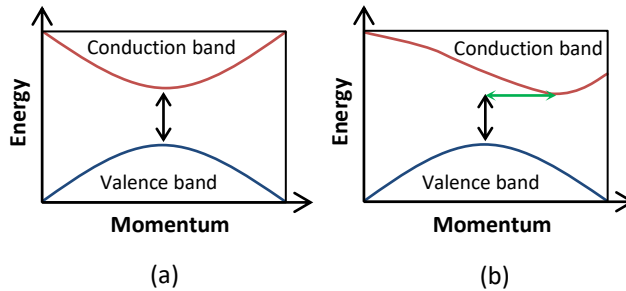


Figure 1.3: Simple illustration of the energy dispersion diagram of a) a direct bandgap semiconductor and b) an indirect bandgap semiconductor.

result of the additional complication in charge carrier generation in indirect bandgap semiconductors, and, therefore, less absorption probability compared to direct bandgap semiconductors, the incident light can travel longer through the material without being absorbed. Therefore, indirect bandgap materials are often poorer absorbers than their direct bandgap counterparts and need relatively thicker layers to absorb the same amount of incident light. For the same reason, the lifetime is longer and thus, also the diffusion length. This absorption quality is evaluated by a parameter called *absorption coefficient*, which determines the distance that light can travel in a material before it is absorbed. The higher the absorption coefficient, the shorter is the distance that light can penetrate inside the semiconductor.

1.2 Absorber categories

In a traditional approach, the absorber of solar cells are categorized as either wafer-based or thin-film-based. These groups are briefly explained in the following.

1.2.1 Wafer-based solar cells

In most of the wafer-based solar cells, silicon (Si) is the absorber material of choice. The wafers are produced by slicing high purity silicon ingots using wire saws. An example of solar cells made by such technology is presented in Figure 1.4. The current standard absorber thickness in wafer-based Si PV technology is above $100\ \mu\text{m}$ (it varies between 160 and $200\ \mu\text{m}$). This is partly because of manufacturing limitations and partly due to silicon's indirect bandgap, and, hence, low absorption coefficient (about $3.03 \times 10^4\ \text{m}^{-1}$ at $\lambda = 900\ \text{nm}$ [12]). The large absorber thickness is to ensure that the incident light is absorbed as much as possible. Owing to several factors, including relatively cheap production, maturity of Si PV technology and high accessibility of silicon (being the second abundant material on earth), this material is the most popular absorber material for solar cells, despite not being the best one. On the other hand, for cost motivations, material consumption should be reduced by reducing the absorber thickness and kerf losses during wafer sawing.

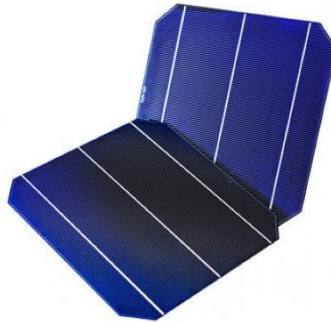


Figure 1.4: Solar cells made from silicon wafers. Image taken from [13]

1.2.2 Thin-film solar cells

The absorber of thin-film solar cells is typically much thinner than that of the wafer-based solar cells. This is mainly achieved by employing absorbers with direct bandgap, and, therefore, high absorption coefficient. At the time of this thesis publication, Gallium arsenide (GaAs) holds the world record power conversion efficiency³ among thin-film and wafer-based single-junction solar cells (solar cells with only one p - n junction) [14] and due to its high price, is mainly used in space applications, where efficiency outweighs cost. Other thin-film PV technologies include: copper indium gallium (di)selenide (CIGS), Cadmium telluride (CdTe), amorphous / microcrystalline Si, Perovskite, dye sensitized, etc.

Due to the typically low thickness of thin-film solar cells (less than $10\ \mu\text{m}$), they require a supporting carrier, a substrate or superstrate. A variety of materials, including glass, polyamide and steel can be used as super/substrates. This selection flexibility makes thin-film solar cells attractive for light-weight and flexible PV cell applications. However, so far, due to lower efficiency and higher manufacturing costs per Wp , thin-film PV technologies have not been able to compete with wafer-based counterparts. Currently, only 4-6% of total global PV-based power capacity is covered by thin-film solar cells [15]–[17].

In the following sections, CIGS solar cells, which are the focus of the thesis at hand, will be introduced. A brief history of this PV technology, its state of the art, the typical solar cell structure, optical and electrical losses will be discussed.

1.3 CIGS solar cells

The history of CIGS solar cells goes back to 1975, when the scientists at Bell Laboratories successfully fabricated a cell with 12% solar energy conversion efficiency. The cell was made of a CdS layer, evaporated on a single copper indium diselenide (CuInSe_2 or CIS) crystal [18]. This sparked an ongoing research on CIS thin-films.

³Power conversion efficiency, also known as efficiency in PV research community, is the ratio between the maximum electrical power generated by a solar cell to the input power.

Different methods for the formation of the CIS films were investigated. For instance, at the University of Maine, dual-source evaporation of CuInSe_2 and Se was used for this purpose [19]. The first small-area CIS solar cell devices in the 1980s showed efficiencies less than 10%. It was the Boeing group with a co-evaporation technique that demonstrated CIS solar cells with more than 10% efficiency [20]. In this technique, the precursors (Cu, In and Se) are evaporated from separate evaporation sources and deposited onto the substrate. In the beginning of the 1990s, gallium (Ga) was added to the compound. As will be explained below, the addition of Ga provides the possibility of tuning the bandgap. The research on CIGS solar cells continued to evolve towards higher efficiencies with using sodium-containing substrates and the development of more complicated three-stage co-evaporation processes [21]. The second technique, which started to develop almost at the same time as the co-evaporation method, is called deposition-reaction technology and involves the deposition of the metallic precursors in a HSe_2 atmosphere as the reacting chalcogen source. In this thesis, we work with CIGS solar cells fabricated within a three-stage co-evaporation process, although the general discussions, modelling techniques and proposed structures are applicable to both fabrication methods. In the three-stage co-evaporation process [21], the elemental flux of evaporation precursors is varied in three time intervals to change the distribution of elements in the deposited layers.

It is helpful to understand the material composition and the electronic properties of the CIGS material in more detail. CIGS belongs to the chemical family of chalcopyrites. Chalcopyrites, the name of which originates from the mineral CuFeS_2 , are I-III-VI₂ ternary compounds. It means that they are composed of elements from groups I, III and VI in the periodic table of elements. Together, they form a tetragonal crystalline structure, in which each group-I and III atom bonds with four group-VI atoms in a tetrahedral format, and each group-VI atom bonds with two group-I and two group-III atoms in the same format (see Figure 1.5) [22]. The bandgap of CIGS can be tuned by changing the composition of group-III elements. More accurately, the chemical compound is $\text{Cu}(\text{In}_{1-x}\text{Ga}_x)\text{Se}_2$, in which x takes values between 0 and 1. CIS and CGS have bandgaps of 1 and 1.71 eV, respectively [23], giving CIGS the possibility of attaining any value in this range by varying x . Some research and development groups also use a *sulfurization* step in the process and therefore, the material becomes $\text{Cu}(\text{In}_{1-x}\text{Ga}_x)(\text{Se}_y\text{S}_{1-y})_2$ or simply CIGSSe. The sulfur is found mostly close to the front surface of the absorber, where it widens the CIGS bandgap near the metallurgical junction with CdS, resulting in less interface recombination [24], [25]. Another attractive feature of this material is its high absorption coefficient (about $2.2 \times 10^6 \text{ m}^{-1}$ at $\lambda = 900 \text{ nm}$ for a bandgap of 1.12 eV [23]), thanks to the direct bandgap that facilitates high absorption of light in very thin (less than $3 \mu\text{m}$) absorber layers [26].

1.3.1 State of the art

At the cell level, during the writing of this thesis, the world record efficiency of lab-scale CIGSSe solar cells is 23.35%, held by Solar Frontier [14], [27]. At the module level, the record efficiency of rigid CIGS modules is 19.2% and belongs also to Solar Frontier [28], while that of the large area (1.08 m^2 aperture area) flexible modules is 18.64% by Miasolé [29]. In the year 2019, CIGS PV technology contributed to 1.6

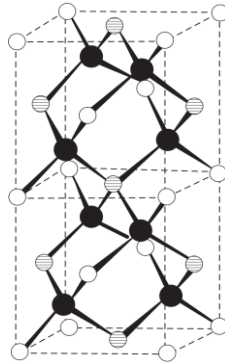


Figure 1.5: The chalcopyrite crystal structure. White, dash-filled and black circles represent group I, III and VI elements, respectively (image taken from [22]).

GWp of the total 136.8 GWp global PV power production capacity. This translates into 1.17% of the total PV and 21.33% of the thin-film technology power capacity share [17].

A hot topic in CIGS research community is ultra-thin (less than $1\ \mu\text{m}$) CIGS absorbers, which is due to the following reasons. The precursors In and Ga (especially In) are scarce and of high demand in electronics, opto-electronics and flat panel industry. High demand and limited resources lead to high prices and supply risk, and, therefore, hinder terawatt-scale production. On the other hand, cell to module efficiency loss needs to be reduced as well. In this respect, as part of the solution, thinner absorbers not only can reduce the end price by consuming less material, but also the production time can be considerably shortened. From a performance point of view, the major drawback of thickness reduction is that it comes at the expense of poor optical performance (i.e. low charge carrier generation rate). As will be shown in the next chapter, incomplete absorption increases as the absorber thickness reduces. Accordingly, light management to compensate thickness-related optical losses in CIGS solar cells is a critical research subject and is pursued by several research groups [26], [30]–[38]. We will discuss this topic in detail in the following chapters. On the other hand, as the absorber thickness decreases, the charge carrier generation occurs closer to the back contact, in this case, molybdenum (Mo). As a result, holes, which are less mobile than electrons, have to travel a shorter distance to reach the back contact and, therefore, the chance of recombination is less. This is provided that the interface between the absorber and the back contact, i.e. the CIGS / Mo interface, is properly passivated (for more information about passivation, please refer to Section 1.3.4) [31], [33].

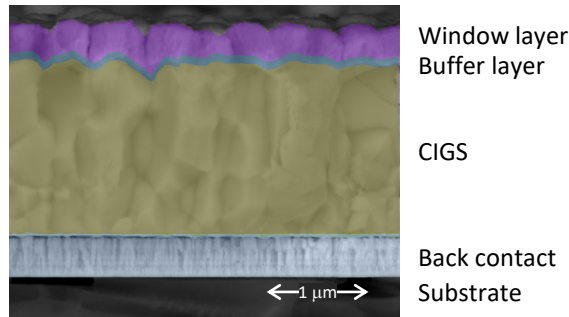


Figure 1.6: Cross section of a CIGS solar cell using scanning electron microscopy (SEM). The layers from bottom to top are the glass substrate, molybdenum back contact, CIGS absorber, CdS buffer layer and a double-layer window consisting of intrinsic ZnO and aluminum-doped ZnO. The role of each layer is explained in the main text. The top grey area is the surface of the window layer. (courtesy of Dr. Marcel Simor, TNO).

1.3.2 Structure of CIGS solar cells

Figure 1.6 schematically shows the structure of a CIGS solar cell, fabricated by our collaborators at TNO research organization. From bottom to top, it consists of a glass substrate, Mo back contact, CIGS absorber, CdS buffer layer and the window layer. Depending on the companies' and the research labs' strategies and application of the cells, the materials and their thicknesses can vary. In the following, an overview of the main layers other than the absorber is presented.

Substrate

CIGS solar cells are typically made in substrate configuration, also known as bottom-up approach. This means that the cell fabrication starts from the substrate layer (the bottom-most layer in Figure 1.6), continues with the formation of the subsequent layers and ends with the light-facing transparent conductive oxide (TCO) layer. The most common substrate is soda lime glass (SLG), which is favorable for its high thermal stability, thermal expansion coefficient similar to that of CIGS and its sodium (Na) content. The sodium existing in SLG can diffuse into the CIGS layer and improve the cell's efficiency. The role of Na, which is an alkali metal, in efficiency improvement of CIGS solar cells has been highly debated in CIGS research community and many research results have been published on that matter [39]–[43]. The amount of Na incorporated into the CIGS layer through the SLG substrate is uncontrollable [24]. For this reason and, also for flexibility in the choice of the alkali metal, sometimes a Na barrier is deposited on SLG. The alkali metal is then added using a post-/pre-deposition treatment of the CIGS absorber. Typical choices for the alkali metal besides Na are rubidium, caesium and potassium [27], [30], [44]. Flexible substrates such as stain-

less steel and polyimide are increasingly being used and investigated for light-weight and flexible applications. This can make roll-to-roll fabrication with high industrial throughput possible. In case of stainless steel substrates, an iron barrier is needed before depositing the back contact to prevent the iron from diffusing into the absorber, and, therefore, reducing the efficiency of the solar cell [45].

Back contact

The most commonly used back contact for CIGS solar cells is molybdenum (Mo), normally formed by direct current (DC) sputtering [46]. Mo is popular, because it is stable and inert during high-temperature growth of the CIGS layer, it is economical and provides an ohmic contact with CIGS due to a MoSe₂ layer formation [24], [47]. Mo is normally sputtered on the substrate in two steps: a high pressure sputtering leads to a porous Mo layer with good adhesion to the substrate. This is followed by a low pressure sputtering for a dense, and, therefore, a low-resistive Mo contact [48], [49].

The high absorption coefficient and the low reflectivity of Mo reduce the optical performance of the solar cell, meaning that a significant part of the incident light is absorbed in Mo and cannot contribute to charge carrier generation. Research is ongoing on different methods to tackle this challenge. Different alternative back contacts, such as W, Nb, Ti, Ta, Cr etc. have been investigated [47]. However, so far, Mo has shown better performance, due to better absorber growth. Silver is a significantly better reflector, yet less thermally stable than Mo. Gouillart et al. proposed an Ag / ITO (SnO:In) reflector stack, covered with a dielectric layer with point contacts as the back contact of a sub-micron CIGS solar cell [50]. The point contacts in the dielectric connect the absorber to the back contact and facilitate the charge carrier collection. Although the cell performance is improved with respect to the case with Mo back contact, large-scale and relatively cheap production of this structure remains in question, as it probably needs nanoimprinting [50], [51] or nanolithography. In another work, Gouillart et al. fabricated ultra-thin CIGS solar cells with ZnO:Al (AZO) / Ag / ITO and AZO / Ag / AZO / ITO reflective back contacts. The results show that the second stack performs better than the Mo back contact due to better internal reflection and no Ag diffusion into the CIGS layer [37]. This approach and many more techniques for quenching Mo-associated optical losses are one of the aspects of light management in CIGS solar cells and will be addressed in the following sections.

Buffer layer

The term *buffer layer* is used for the layer that forms the *p-n* junction with the absorber and is placed between the window layer and the absorber (see Figure 1.6). The role of the *n*-type buffer layer in CIGS solar cells is manifold: better lattice match between the absorber and the window layer (transparent front contact), protection of the CIGS surface during the sputtering of the window layer and the formation of a low-recombination heterojunction [52], [53]. The conventional buffer material for CIGS solar cells is CdS with a few tens of nanometer thickness. Although it has

been shown that even in case of broken cells no Cd leaks into the environment [52], reservations remain towards the employment of toxic materials like Cd. The toxicity of Cd and the high parasitic absorption of CdS have stimulated the research on alternative buffer layers for this PV technology and Cd-free CIGS solar cells are increasingly being produced. Some candidates for Cd-free buffer layers are Zn(O,S), In_2S_3 , $(\text{Zn,Mg})\text{O}$ and $(\text{Zn,Sn})\text{O}$ [27], [54]–[56].

CdS is deposited on the CIGS surface by chemical bath deposition (CBD) [57]. The advantages of this technique include low price, compatibility with large cell area and uniform coverage of CdS on the absorber. On the other hand, CBD requires vacuum breakage, which is not suitable for roll-to-roll processes. Other dry deposition techniques such as physical vapor deposition (PVD) or physical sputtering can be used for Cd-free buffer layers [56]. Also, atomic layer deposition (ALD) can be a potential substitute for CBD, due to less chemical waste and no need for vacuum breakage [58]. For example, the buffer layer structure of the world record CIGS_{se} solar cell consists of a $\text{Zn}(\text{O,S,OH})_x / \text{Zn}_{0.8}\text{Mg}_{0.2}\text{O}$ double layer deposited using CBD and ALD, respectively [27].

Window layer

The window layer, which is responsible for the lateral transportation of current to the front contacts, is a transparent layer (the topmost layer in Figure 1.6) that receives light on the front side and transmits it to the absorber through the buffer layer at its back side. For the solar cells with substrate configuration, it is desired that the window layer exhibits three distinct features: 1) optical transparency in order for the light to be transmitted to the absorber layer without being absorbed in the window layer, 2) low resistivity (high electrical conductivity) for efficient lateral current transport, and at the same time, 3) a high resistivity for screening shunts [24]. Obviously, the last two features are contradictory and cannot co-exist in one material, which is why the window layer is typically a double layer. A thin high-resistance oxide is sputtered on the buffer layer of the solar cell and secures the cell from shunts (current leakage). In CIGS solar cells, the most common material for this purpose is a few tens of nanometers of ZnO formed by Radio Frequency (RF) sputtering.

On the other hand, the transparency feature of the window layer demands for a high bandgap material. Undoped oxides with bandgaps larger than 3 eV are insulators at room temperature. Adding *n*-type dopants to these oxides makes them conductive, which in terms of energy band diagram, it means that the position of the Fermi energy changes such that it is above the conduction band minimum, similar to metals. The resulting doped oxide is called a transparent conductive oxide (TCO). By increasing the doping concentration, the resistivity decreases, which fulfills the second requirement, mentioned above. On the other hand, the higher carrier concentration shifts the infrared absorption edge (plasma absorption edge in the infrared part of the spectrum) towards the visible spectrum [59], reducing the transparency, and, therefore, violating the first abovementioned requirement. This means that there is a trade-off between low resistivity and high transparency as functions of carrier concentration and a compromise should be found. It is worth mentioning that the resistivity also depends on carrier mobility: the higher the mobility, the less is the resistivity. Mobility can be increased

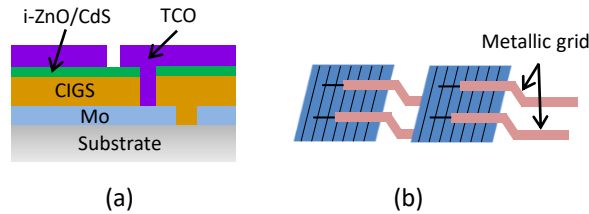


Figure 1.7: Two CIGS solar cells connected a) in a monolithic interconnection approach, and b) by stringing and tabbing.

by material engineering. The thickness is also a determining factor, as both the sheet resistance and optical transparency decrease by increasing the thickness. RF-sputtered Al-doped zinc oxide (AZO) is the typical material for the window layer of CIGS solar cells, although, ZnO with other doping materials such as Br, Ga and In are also possible options [60]–[62]. Other possible materials include ITO and $\text{In}_2\text{O}_3\text{:H}$ (IOH) [60], [63].

1.3.3 Optical losses

The optical performance of a solar cell is related to how much and in which layer the light is absorbed, reflected or transmitted. In general, it is desired that no *usable light* (light with energy higher than the absorber bandgap) is reflected from or transmitted through the solar cell. Also, ideally, the light is only absorbed in the absorber layer and not in the supporting layers. This ensures a high charge carrier generation rate in the absorber and what we consider as a good optical performance. In this respect, we summarize below the optical losses in CIGS solar cells from the light-facing side to the substrate.

A part of the incident light is reflected from the front side of the solar cell due to the change in the refractive index between air and the top layer of the solar cell. The reflection loss, according to Snell's law [8], depends on the wavelength-dependent refractive index of the solar cell's layers.

Optical shading refers to the lost part of the light due to the presence of the front grid, which hinders the light from reaching the absorbing layers and generating charge carriers. In CIGS PV technology with rigid substrate, the monolithic interconnection approach is used to connect the cells in series (Figure 1.7(a)). In this approach, the TCO of one cell is connected to the back contact of the adjacent cell. Since the charge transport at the front side of the cells occurs via the TCO, no metallic grid is needed and optical shading does not occur. On the other hand, laser scribing causes material loss and dead cell areas. On the contrary, in case of flexible CIGS solar cells, the monolithic interconnection technique is less common due to technological limitations. In that case, other interconnection approaches such as Shingling [64] or stringing and tabbing (Figure 1.7(b)) [65] are employed. As a result, the metallic grid, deposited onto the TCO to improve transport of carriers [66], reduces the active area of the solar cell and causes the optical shading. There is a trade-off between optical shading and resistive losses as functions of the grid size, which should be optimized for optimal

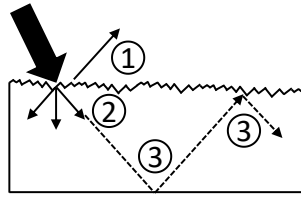


Figure 1.8: Simple schematic of light management approaches. Numbers in the figure show: (1) the reduction of the primary reflection due to light in-coupling, (2) light scattering and (3) internal reflection. Light trapping consists of (2) and (3).

power output.

A portion of the light is absorbed in the supporting layers, i.e. window and buffer layers and the Mo back contact. Since the light absorbed by these layers does not contribute to the collectable charge carriers (due to high recombination and conversion to heat), it is called parasitic absorption. Parasitic absorption depends on the thickness and the absorption coefficient of the layers.

As the light propagates in the absorber, it is partially absorbed. As mentioned before, the efficiency of light absorption depends on the absorption coefficient. Incomplete absorption is a type of optical loss that is due to the limited thickness of the absorber. In other words, the absorber should be thick enough for all the incident light to be absorbed and thin enough for the photo-generated charge carriers to be collected at the contacts before being recombined. Therefore, there is a trade-off between light absorption and charge carrier collection because of the limited diffusion length of charge carriers. As a result, part of the light is lost due to incomplete absorption.

Light management

Light management refers to different techniques to improve the optical performance of the solar cell. In brief, it consists of three major approaches: i) light in-coupling to increase the chance of the incident light in entering (being coupled into) the solar cell, ii) light scattering for distributing the in-coupled light over wide angles to increase its path length (leading to a higher absorption efficiency), and iii) internal reflection to trap the photons as long as possible until maximum absorption. Light scattering and internal reflection are the two aspects of light trapping.

Figure 1.8 shows a simplified schematic of the abovementioned approaches. A variety of methods have been employed by different research groups for reduction of the primary reflection⁴, hence, improvement of light in-coupling over wide ranges of light spectrum (number 1 in Figure 1.8) [67]–[70]. These include single- or multi-layer antireflection coatings (ARC) and textured surfaces and will be discussed in more details in **Chapter 4**. Additionally, less absorptive supporting layers are desired for less parasitic absorption.

⁴The primary reflection arises from the refractive index mismatch between the incidence medium and the solar cell's surface.

Light scattering (number 2 in Figure 1.8) can be achieved by introducing roughness into the rear and/or front side of the structure. Although random textures lead to more uniform angular distribution of the photons, it has been shown that periodic textures can result in higher optical gains in some narrow parts of the spectrum [71], [72]. Metallic or dielectric nanoparticles as well as nanowires have also been studied for this purpose [73]–[75], although, due to high parasitic absorption, high recombination at the surface of the nanoparticles and complicated fabrication, they are not employed yet in industrial CIGS solar cells.

Incomplete absorption of low-energy photons is more significant in sub-micron CIGS solar cells than their thicker counterparts. Compared to high-energy photons, the low-energy photons penetrate deeper into the absorber before they are absorbed. This necessitates enhanced internal reflection in the absorber. As mentioned above, Mo / CIGS interface is poorly reflective and a significant part of the photons reaching that interface is absorbed by Mo. Alternative back reflectors and dielectric spacers can be used to avoid this problem and provide a second (or more) chance for the light absorption. This problem is addressed in **Chapter 3**.

1.3.4 Electrical losses

The generated charge carriers are subject to recombination, due to different reasons, in the absorber bulk, at the interfaces and/or at the contacts and in the supporting layers. Charge carrier recombination prior to the external circuit indicates collection issues. Different recombination mechanisms that are more likely to happen in CIGS solar cells are briefly explained below.

Direct recombination refers to the case when an excited electron with the energy larger than the conduction band minimum energy recombines with a hole. As a result, a photon is radiated, which is why direct recombination is also known as radiative recombination. This phenomenon happens in direct bandgap semiconductors more often than indirect bandgap materials. As explained earlier, the recombination process in indirect bandgap semiconductors is more complicated and involves phonon transfer as well to conserve momentum. The recombination of an electron-hole pair results in the excitation of a third electron (or hole) to higher energy states in the conduction band (or deeper energy states in the valence band), after which the excited electron or hole loses the extra energy in the form of a phonon and reaches a relaxed energy state again. This phenomenon is known as Auger recombination.

Shockley-Read-Hall (SRH) recombination is a non-radiative phenomenon, facilitated by impurity atoms and lattice defects. These material imperfections act as traps for electrons and holes. In other words, they introduce allowed energy states within the forbidden gap of the semiconductor material that are known as defect and trap states. The polycrystalline nature of the CIGS material leads to a significant concentration of material defects. This makes SRH recombination the dominant recombination mechanism in the CIGS solar cells [76]. A special case of SRH recombination is the recombination at the surface of the material, due to broken covalent bonds (dangling bonds).

The series resistance of a solar cell causes additional electrical losses. It refers to the resistance experienced by the photo-generated charge carriers in the path to the

external circuit and is caused by the bulk resistance of the solar cell, the resistance of the electrodes and the contact resistance between the electrodes and the solar cell.

The aforementioned bulk recombination can be reduced by improving the material quality, for instance by forming absorbers with larger grains or less defect density. Surface recombination is tackled by either electrical or chemical surface passivation. Electrical passivation (also known as field-effect passivation) means adjusting the electric field close to the absorber surface to prevent the accumulation (hence, the recombination) of minority charge carriers at the surface. Chemical passivation is facilitated by introducing specific atoms to the surface to form covalent bonds with dangling bonds and refers to the reduction of electrically active (interface) defects [77]. In Si-based PV technology, hydrogen atoms are widely used for the passivation of defects [78], [79]. The application of Al_2O_3 in rear surface passivation of CIGS solar cells at the CIGS / Mo interface has been the subject of several research activities [77], [80]–[86]. The chemical and electrical passivation techniques will be discussed in **Chapter 6**, where the structure of an interdigitated back-contacted (IBC) CIGS solar cell will be optimized for minimal optical and electrical losses.

1.4 Aim and scope of this thesis

The aim of this thesis is to study, propose and optimize light management techniques in sub-micron CIGS solar cells using optical and electrical modelling approaches. Considering the high absorption coefficient and direct bandgap of this material, it has been demonstrated that ultra-thin absorbers are sufficient for high optical performance [75]. Therefore, an advanced opto-electrical study of different passivation and light management techniques, in order to achieve the best possible efficiency of these devices, appears crucial. In the thesis at hand, a number of technologies are studied to improve optical as well as electrical performance of reference sub-micron CIGS solar cells. A brief literature study on each light management technique under investigation is reported at the beginning of the corresponding chapter. In this respect, this thesis reports on (i) investigation of the back contact optical losses; (ii) optical optimization of a dielectric stack with local point contacts between the absorber and the back contact to minimize such losses; (iii) angular resilient (resilient against the light's angle of incidence) light in-coupling using a double-layer ARC based on MgF_2 ; (iv) a novel parasitic absorption-free IBC CIGS solar cell; and, finally, (v) opto-electrical optimization of the proposed IBC CIGS solar cell.

1.5 Outline

This thesis is outlined as follows: **Chapter 1** (this chapter) gives a general introduction of CIGS solar cells, their structure and different loss mechanisms in (sub-micron) CIGS solar cells. In **Chapter 2**, optical benchmarks for CIGS performance will be presented and opto-electrical modelling platforms / techniques used will be explained. In **Chapter 3**, firstly, the nature of optical losses at CIGS / Mo interface will be investigated. Then, dielectric spacers with local point contacts between Mo contact and CIGS absorber will be studied for increasing the rear reflection by the elimination of

plasmonic losses at the corresponding interface. Light in-coupling improvement with double-layer porous MgF_2 ARC is the subject of the next light management approach that will be discussed in **Chapter 4**. It will be shown that as far as resilience of the antireflection effect against the light's angle of incidence is concerned, the new structure outperforms its conventional single-layer counterpart. Also, the optical performance of the cell with sub-micron absorber and a combination of the abovementioned modifications will be compared to that of a cell with almost twice as thick of an absorber. **Chapter 5** covers the new (for CIGS PV technology) IBC CIGS solar cell that no longer suffers from parasitic absorption in the top layers, i.e. the buffer and window layers. We optically optimize the geometrical features (periodicity, width and thickness of the contacts and the ARC dimensions) of the new solar cell. Electrical performance of the proposed IBC solar cell will be presented in **Chapter 6**, where we explain in more details, the function of each layer. We first calibrate the input parameters of the electrical model using experimental measurements of the reference front- and back-contacted (FBC) solar cell. Then, we vary the geometrical and material features of different layers to study and optimize the overall performance of the IBC cell. Finally, **Chapter 7** summarizes the thesis conclusions and presents the outlook.

1.6 Main contributions to the field

This thesis has contributed to the CIGS PV technology in the following ways:

- It answers the questions about the physical nature of optical losses at the back contact of CIGS solar cells.
- The double-layer dielectric stack, consisting of MgF_2 and Al_2O_3 , sandwiched between CIGS and Mo is optically optimized to quench the Mo-related optical losses. The Al_2O_3 layer in this stack is used to reduce the recombination losses (demonstrated in other researches [87])
- An angular resilient ARC using porous-on-compact MgF_2 was proposed and optimized using effective medium approximation (EMA) in the 3-D optical modelling. According to our analysis, the proposed ARC outperforms the conventional single-layer ARC only in resilience against the light's angle of incidence. Therefore, if angular resilience is not required, the additional fabrication complication associated with development of a porous layer on a CIGS solar cell is unnecessary.
- For the first time in CIGS PV technology, an IBC configuration is introduced and investigated. The new CIGS solar cell no longer suffers from parasitic absorption and performs both optically and electrically better than the conventional FBC CIGS solar cells. This is reflected in more than 5% (absolute) improvement of the efficiency compared to the reference FBC solar cell. This research encourages the CIGS community to investigate other solar cell configurations for solving the current challenges of CIGS solar cells.

2

Modelling Approaches

2.1 Introduction

In this chapter, the performance indicators of a solar cell, including current density vs voltage curve, external quantum efficiency and power conversion efficiency are introduced. The theoretical optical limits are explained and finally, the modelling tools, employed in this thesis, are described.

2.2 Solar cell characteristics

The solar cell characteristics are measured in standard test conditions (STC) to allow for location-independent and unbiased comparisons. STC for solar cells means AM1.5G [88] illumination with total irradiance of 1000 W/m^2 and $25 \text{ }^\circ\text{C}$ ambient temperature. AM1.5G indicates that the solar cell is facing the sun at a tilt angle of 37° .

2.2.1 Current density versus voltage curve

From the current density-voltage (J - V) curve, the so-called external parameters of a solar cell can be extracted. These parameters (also shown in Figure 2.1) are the short-circuit current density (J_{SC}), open-circuit voltage (V_{OC}) and fill factor (FF). FF , which is a measure of *rectangularity* of the J - V curve, is calculated as follows:

$$FF = \frac{V_{MPP} J_{MPP}}{V_{OC} J_{SC}} \quad (2.1)$$

where V_{MPP} and J_{MPP} are the voltage and current density at the point of maximal power density (p_{max}) delivered by the solar cell, also known as maximum power point (MPP). From that, the power conversion efficiency (η) is calculated as the ratio between p_{max} and the input power density (1000 W/m^2). There is a common convention among the PV research community to use the term efficiency instead of power conversion efficiency, which is also employed in the thesis at hand from now on. It should be noted that since the solar cell generates power, the current density has a negative sign. But it is also common to present the J - V curve with positive J values.

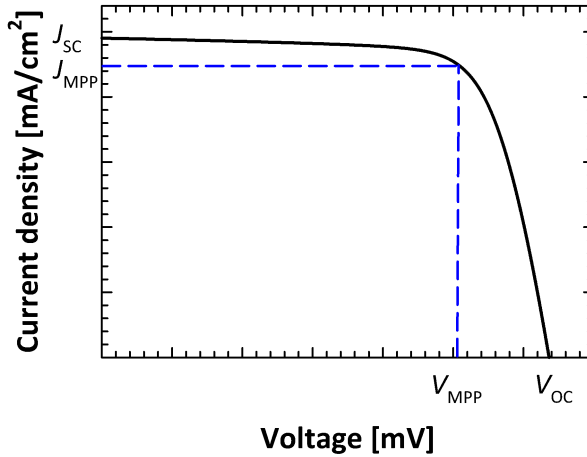


Figure 2.1: An example of the J - V curve of a solar cell. V_{OC} and J_{SC} are the open-circuit voltage and short-circuit current density, respectively. V_{MPP} and J_{MPP} represent the voltage and current at maximum power point (MPP).

2.2.2 The external quantum efficiency

The external quantum efficiency (EQE) is the ratio between the number of photons leading to generation as well as collection of charge carriers to the number of photons incident on the solar cell. This wavelength-dependent parameter is calculated by illuminating the active area of the solar cell with a monochromatic light of wavelength λ and measuring the photocurrent density J_{ph} . Therefore:

$$EQE(\lambda) = -\frac{J_{ph}(\lambda)}{q\Phi_{ph}(\lambda)}. \quad (2.2)$$

In this equation, q is the elementary charge and $\Phi_{ph}(\lambda)$ is the photon flux. The photocurrent density can be calculated from EQE spectrum as follows

$$J_{ph} = -q \int_{\lambda_{min}}^{\lambda_{max}} EQE(\lambda)\Phi_{ph}(\lambda)d\lambda. \quad (2.3)$$

Another important parameter of an absorber material is the spectral generation rate ($G(\lambda)$), which is the number of charge carriers generated per unit area, time and wavelength. As expected, $G(\lambda)$ depends on the incident photon flux and the absorptance in the absorber material ($A(\lambda)$):

$$G(\lambda) = \eta_g \Phi_{ph}(\lambda)A(\lambda). \quad (2.4)$$

η_g is the generation quantum efficiency and defines the number of electron-hole pairs generated by one photon and normally is equal to 1. Furthermore, from the EQE definition, one would realize that EQE can also be derived from the following equation:

$$EQE(\lambda) = \eta_g \eta_e(\lambda) A(\lambda) \quad (2.5)$$

where $\eta_e(\lambda)$ is the electrical quantum efficiency that shows the efficiency in successfully collecting the charge carriers and is always less than one due to recombination. From equations 2.4 and 2.5, one can calculate the relation between EQE and $G(\lambda)$ as

$$EQE(\lambda) = \eta_e \frac{G(\lambda)}{\Phi_{ph}(\lambda)} \quad (2.6)$$

As can be seen in the abovementioned equations, any changes in the optical performance of the solar cell lead to the variation of the absorption, optical generation, EQE and finally, J_{ph} . It is worth noting that the EQE spectrum measured under no bias voltage can be used to calculate J_{SC} ($J_{ph} = J_{SC}$). The reason is that under zero bias voltage, the impact of recombination current density (J_0) on the photocurrent density is included in the amount of collected charge carriers. In many cases, the EQE measurement is performed under negative bias voltage to increase the space charge region width, and, therefore, reduce the recombination current. In other words, J_{ph} is the current density generated but not yet collected and is larger than J_{SC} .

2.3 Optical limits

No matter how well the light absorbed in the solar cell and generated carriers collected at the contacts, the efficiency is limited due to several factors. The efficiency upper limit has been the subject of many researches since early days of solar cells. In 1961, W. Shockley and H. J. Queisser formulated the limiting efficiency of a p - n junction solar cell, considering radiative recombination as the only recombination mechanism in the device [89]. This efficiency limit is abbreviated as SQ limit. According to this formulation, the efficiency limit for the solar cells with bandgaps between 1.05 and 1.75 eV varies from 28% to 33% [90]. Indeed, once the imperfect charge carrier collection is considered, this limit is reduced. For instance, in case of undoped crystalline silicon (c-Si), the efficiency limit predicted by SQ is more than 30%. This reduces to 29.43% practical efficiency limit for a 110- μ m thick solar cell by including the dominant Auger recombination in such c-Si solar cells [91].

Regarding the optical performance, in an ideal situation, $EQE(\lambda) = 1$ and the maximum current density is

$$J_{SC-ideal} = -q \int_0^{\lambda_G} \Phi_{ph}(\lambda) d\lambda \quad (2.7)$$

where λ_G is the bandgap wavelength of the absorber material. This formulation is achieved by simply assuming full absorption of all the photons with energies above the bandgap. In reality, however, the absorption coefficient is wavelength-dependent and reduces near the bandgap wavelength. The so-called classical Yablonovitch absorptance limit [92], [93] calculates the maximum absorption probability in an absorber material under the following circumstances: i) the semiconductor slab is a randomly textured layer with refractive index $n(\lambda)$ ii) it is in equilibrium and surrounded by

black-body radiation and iii) there is zero reflectance at the front side and perfect reflectance at the rear side. In absence of light trapping, the minimal absorptance will be

$$A = 1 - e^{-2\alpha d} \quad (2.8)$$

where α and d are the absorption coefficient and the semiconductor thickness, respectively. The factor 2 shows double-pass absorption due to perfect back reflectance. Note that both parameters are wavelength-dependent. On the other hand, in case of perfect light trapping and Lambertian light scattering at both front and rear interfaces, the light path length will be maximized and the absorptance will be

$$A = \frac{\alpha}{\alpha + \frac{1}{4n^2d}} \quad (2.9)$$

It should be noted that this approximation is only valid in the weak absorption regime ($\alpha d \rightarrow 0$) [92]. A more accurate absorptance limit, also not limited to the weak absorption regime, has been calculated by M. A. Green as follows [94]:

$$A = \frac{(1 - e^{-4\alpha d})}{1 - (1 - \frac{1}{n^2})e^{-4\alpha d}} \quad (2.10)$$

In the thesis at hand, the Green absorptance limit is used as the absorption benchmark and the performance of different light management schemes is compared to this benchmark. Figure 2.2(a) shows the Green absorptance limit for a CIGS material, with a bandgap of 1.12 eV, as a function of thickness and wavelength. Here, for simplicity, we consider the bandgap to be thickness-independent. As can be seen, the absorptance approaches zero near the bandgap wavelength (1107.1 nm) and is more dependent on thickness for thinner absorbers. For larger thicknesses (larger than 1.5 μm), A tends to stay constant at maximum level and shows a nearly abrupt decrease in the weak absorption region. In Figure 2.2(b), the Green absorptance limit, integrated as J_{ph} (see Equation 2.3) for different bandgaps and thicknesses is presented. As expected, lower bandgap absorbers have a higher potential for current production (nearly 46 mA/cm^2 for $E_g = 1$ eV). Also, it is observed that for thicker absorbers at each bandgap value, J_{ph} is independent of thickness. This indicates that at a certain threshold, increasing the thickness leads to no additional current density and should be avoided to potentially reduce the production cost and time. Once again, the possibility of high current generation with low-bandgap, low-thickness absorbers emphasizes the choice of CIGS both as a single-junction solar cell material and as the bottom cell in multi-junction applications [95].

2.4 Optical simulation tools

Rigorous three-dimensional (3-D) optical modelling has been widely used to design, optimize and characterize various thin-film solar cell technologies. 3-D modelling has several advantages over 2-D and 1-D approaches, including i) more accurate calculation of electric field distribution and plasmonic losses due to the possibility of modelling

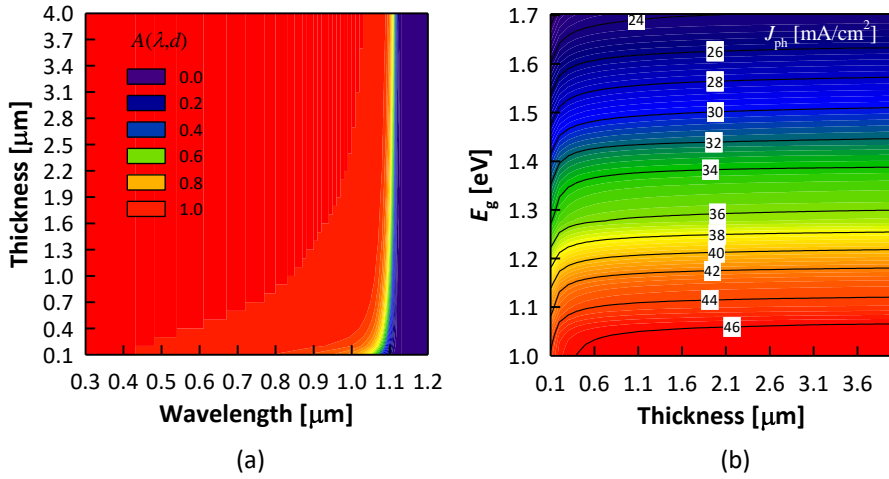


Figure 2.2: a) Absorptance benchmark according to the Green formula as a function of absorber thickness and wavelength for a CIGS absorber with $E_g = 1.12$ eV, b) Green absorptance limit integrated as photocurrent density as a function of absorber bandgap and thickness. The bandgap is considered thickness-independent.

natural textures of solar cells and ii) optimization of periodic gratings for light management purposes in real-life cases. Several commercially available optical simulation tools, based on different numerical methods, have been employed by different research groups for modelling CIGS solar cells. Below, a brief introduction to some of those numerical methods is provided:

2.4.1 Finite-difference time domain (FDTD) method

FDTD method [96] works on the spatial derivatives of the differential operators in Maxwell's equations in time domain. The derivatives are discretized by expanding the film on a regular tensorial grid. Then, the temporal derivatives are integrated by time stepping. It is an explicit easy-to-parallelize method and does not require a large set of linear equations [97]. Therefore, a broadband pulse source can provide the structure's response over a wide wavelength range in one simulation run. However, this method is only suitable for transient or narrow-band calculations for structures consisting of perfect conductors or low-loss dielectrics. Accurate transient calculations are possible for materials with high frequency dependence in their optical properties [98]. Attempts for taking into account the dispersive characteristics of materials commonly lead to convergence problems or long calculations. Examples of employing FDTD method in modelling of thin-film solar cells can be found in [99]–[102].

2.4.2 Rigorous coupled wave analysis (RCWA)

RCWA [103] is a rigorous method for 1-D or 2-D periodic structures that calculates the electromagnetic modes of each layer using Floquet functions and then applies the boundary conditions to calculate the reflected and transmitted orders [104], [105]. In this technique, the structure is divided into layers in which the material is homogeneous in the propagation direction. Fourier transform is used for every layer to represent the permittivity, transverse electric (TE) and transverse magnetic (TM) components of the electromagnetic field. By applying the boundary conditions, a matrix is formed and finally, the coupling coefficient for each Fourier component is calculated [106]. The accuracy of the results and the simulation speed depend on the degree of filtered higher order Floquet functions. Several applications of RCWA in modelling thin-film CIGS solar cells can be found in literature. For instance, Goffard et al. and Gouillart et al. used RCWA to model 2-D periodic nanostructured back mirrors for ultra-thin CIGS solar cells [34], [50].

2.4.3 Finite integration technique (FIT)

FIT is a time-domain technique, which uses a spatial discretization method to solve electromagnetic problems. It was proposed in 1977 by Weiland [107] and is viewed as a generalization of the FDTD method. FIT discretizes the integral form of Maxwell's equations over a pair of dual intertwined discretization grids and so, generates Maxwell's Grid Equations (MGEs). The physical properties of the computed fields are therefore, guaranteed and a unique solution is achieved. This technique can be applied to different mesh types and, in Cartesian coordinates, its time-domain form is equivalent to FDTD [108]. Other advantages of FIT include i) the possibility of modelling a wide range of material properties such as dispersion, anisotropy and non-linearity and ii) memory-efficient algorithms because of leap-frog integration scheme. FIT has been used in modelling thin-film silicon solar cells with grating couplers [109], [110] and in tandem applications [111].

2.4.4 Transfer matrix method (TMM)

In optics, TMM is used to study the propagation of electromagnetic waves in a multi-layer medium. In the simple case of a single interface between two media, the Fresnel coefficients describe the reflection of light from the interface. However, for a multi-interface system, the interference affects the total reflection. Using the continuity conditions of the electric field at each interface, a characteristic matrix (M_i , where i is the layer number) for each layer can be obtained. M_i depends on wavelength, the thin-films' complex refractive index and thickness. The whole system's characteristic matrix is the product of the characteristic matrices of all the individual layers. Eventually, wavelength-dependent transmittance, reflectance and absorptance of the layers are calculated [35]. TMM is applicable to optically isotropic and homogenous layers with flat interfaces in a coherent system [112]. More complex modifications are needed for rough or textured interfaces and incoherent systems. For example, a 3-D combined Ray-Optics Wave-Optics model (CROWM) combines thin-film wave optics (coherent TMM) and geometrical ray optics to overcome this challenge [113].

2.4.5 Net-radiation method

The net-radiation method solves a set of equations relating the incoming and outgoing energies at each interface in a multi-layer system [114]. Absorptance of individual layers, reflectance and transmittance are calculated by solving $4 \times I$ number of equations, (where I is the number of interfaces) relating the wavelength- and angular-dependent Fresnel coefficients to complex electric and magnetic fields at every interface [114], [115]. The advantage over TMM is that instead of solving a system with a sequence of 2×2 transfer matrices, only one set of linear equations is used to calculate all complex amplitudes. This technique is applicable to coherent and incoherent layers. However, if the incoherent layers are treated with coherent net-radiation method, an unrealistic pattern of interference patterns will appear in the resulting spectra [115]. This error can be corrected by averaging the interference fringes out. Santbergen et al. developed a simple and accurate method to correct the results for incoherent layers; Therefore, a multi-layer system consisting of coherent, incoherent and partly coherent layers can be analyzed only using the net-radiation method [115]. Their methodology is implemented in GENPRO4 software, which can optically model multi-layer solar cells with surface textures. The coherent layers are treated as *coatings* and are part of the interface between two thick (incoherent) *layers*. It is possible to use atomic force microscopy (AFM) scans or angular intensity distributions of large textures as input. Then, GENPRO4 uses angular intervals to include light scattering by surface textures. This increases the number of equations to $4 \times I \times V$, where V is the number of angular intervals. The resulting generation profile is in one dimension [116].

2.4.6 Finite element method (FEM)

FEM is a numerical method to solve partial differential equations of boundary value problems. It was first introduced by Courant in 1940 [117] to solve vibration and equilibrium problems, followed by aircraft design applications in 1950s. It was modified over time such that its applications were extended to fluid dynamics and electromagnetics [118]. Some advantages of FEM include accuracy, the possibility of modelling inhomogeneous and dispersive materials (it is a frequency-domain technique) and straightforward modelling of optical effects on the surface of metallic nanoparticles [104], [119].

After the system is mathematically modelled, the boundary value problem is resulted as follows:

$$L\phi = f \quad (2.11)$$

with L as the differential operator, f as the excitation and ϕ as the set of unknowns [118]. Accordingly, the wave equation in electromagnetics is described in the following:

$$\nabla \times \left(\frac{1}{\mu} \nabla \times \vec{E} \right) - \omega^2 \varepsilon \vec{E} = -j\omega \vec{J} \quad (2.12)$$

in which \vec{E} is the electric field, μ the magnetic permeability, ε the electric permittivity, $\omega = 2\pi f$ the angular frequency (with f as the frequency) and \vec{J} is the current density

vector [118]. An alternative equivalent equation exists for the magnetic field, \vec{H} . It is necessary to select a trial function to approximate the solution, which is difficult in case of 2-D or 3-D problems. Therefore, the problem domain is divided into small subdomains and the trial functions for each subdomain are defined. At this point, two methodologies can be used to solve the equation set, Ritz method and Galerkin method. The former is known as variational finite element method and the latter is called Galerkin finite element method, which uses weighting functions to achieve the solution [118]. Finally, the solution is obtained for the nodes of the subdomains. An overall classification of the mesh generation approaches can be found in [120]. It is worth noting that the mesh generation process in large 3-D structures is very demanding in terms of time and random access memory (RAM) [104].

Several commercial packages have been used for modelling CIGS solar cells. Some of them include JCMSuite [121]–[123], COMSOL Multiphysics [124]–[127] and Ansys HFSS [72], [128]–[130]. Since Ansys HFSS is the software selected for the optical simulations in the thesis at hand, a more in-depth introduction to this tool will be provided.

High frequency structure simulator (HFSS)

HFSS is a 3-D full wave electromagnetic solver based on FEM with adaptive meshing to increase the accuracy and reliability of the results. The 3-D interface enables the user to model complex 3-D structures or import CAD models. The extraction of scattering matrix parameters and the 3-D electromagnetic field visualization are possible. Parameterization is possible for defining variables and making design variations. HFSS meshes the volume by producing tetrahedral elements, at whose vertexes the electromagnetic problem is solved. This characteristic as well as adaptive meshing lead to conformal mesh generation, which is suitable for simulating arbitrary structures. Moreover, the freedom in choosing zero-order, first-order or, second-order elements and even a mixture of them in different parts of the structure makes the simulation time and memory usage more efficient [131]. The modelling procedure in HFSS includes:

- Sketching the structure
- Defining the materials
- Setting the boundary conditions
- Defining the excitations
- Setting the solution frequency and frequency range
- Designing the parametric sweep (if necessary)
- Creating the results report
- Model validation
- Starting the analysis

- Meshing
- Solving for the initial frequency
- Frequency sweep

2.5 Electrical simulation tools

Electrical characterization/modelling of solar cells is as crucial as their optical analysis. As based on semiconductor materials, solar cells follow Poisson, continuity and drift-diffusion equations. While generation of charge carriers is calculated in optical analysis, electrical simulations in device-level address recombination, drift and diffusion mechanisms. The generation rate calculated by optical simulations is fed to the electrical model, leading to the extraction of the external parameters and further design guidelines. There are many commercial and in-house opto-electrical modelling tools used by PV community. ASA, developed in PVMD group of Delft University of Technology, is a 1-D opto-electrical simulation tool with GENPRO4 implementation as the optical solver. It was originally used for amorphous Si solar cell simulations and later was modified to include more advanced c-Si models. The newest version of the software is extended to model other solar cell technologies, including CIGS with bandgap grading and perovskites [132]. Some examples of ASA application in design and modelling of solar cells can be found in [133]–[136]. A few other widely used 1-D programs are SCAPS 1D [35], [137]–[142], PC1D [91], AMPS-1D [143], [144], Quokka-1D [78] and AFORS-HET [145]. The list does not end here, as many groups have developed their own modelling tools for customized requirements.

Although 1-D models have provided priceless input to researchers, there are critical limitations to them. The charge transport in 1-D simulations is limited to one direction, i.e. perpendicular to the device's plane of incidence. Due to the 3-D structure of the solar cell, charge carriers have to travel in all directions (mostly in lateral direction in case of thin-films). Additional requirements on material and contact quality are therefore, present for better charge collection. This is addressed by 2- and 3-D simulations. Moreover, non-uniformity in thickness and material properties (lifetime, bandgap, mobility, ...) always occur in real-life solar cells and should be carefully understood. To create a model, the following steps need to be taken: defining materials and geometry, introducing doping profiles, electronic properties, optical properties, incident light spectrum, boundary conditions and discretizing the geometrical structure (meshing). Besides, the recombination mechanisms in each material and interface should be defined, for which, the defect density and distribution and charge carriers' capture cross-section or lifetime need to be described. There are several commercial tools for 2- and 3-D modelling of solar cells, including Sentaurus TCAD, ATLAS, Quokka, PC2D and PC3D.

Having started in 1984, SILVACO ATLAS has contributed to different areas of semiconductor research [146]. 2- and 3-D opto-electrical simulations are possible and different optical solver methods such as mode solver, ray tracing, TMM and FDTD are available. The electrical performance of amorphous and polycrystalline materials can be simulated using TFT package. Energy-dependent density of states (DOS), different tunneling mechanisms and DC, AC and transient simulations are provided

in TFT. Delgado-Sanchez et al. performed 2-D simulations in ATLAS environment to optimize the front contact structure of industrial CIGS solar cells in different solar concentrations [147]. Using the same tool, Sharbati et al. optimized Zn(O,S) buffer layer parameters in a CIGS solar cell to improve the overall performance. These parameters include the thickness, doping density and oxygen content [148].

Quokka [149] is especially designed for silicon solar cells and uses a C++ code for its finite difference approach. Large-area effects such as distributed metal resistance and edge recombination can be modelled. However, Quokka3 does not support detailed optical modelling for textured or thin-film solar cells. Therefore, the optical generation profile must be imported from other solvers in this case. An example of the application of Quokka3 in quantifying losses in an IBC silicon solar cell can be found in [150].

Sentaurus TCAD (our choice for our electrical simulations) is a multidimensional device simulator for modelling optical, electrical and thermal properties of semiconductor materials [151]. A real device is approximated by a virtual device that is described by a TDR file, containing the device's grid (geometrical features) and the data files (doping profiles, ...). Creating, managing, executing and analyzing the TCAD simulations are done in a graphical environment called Sentaurus Workbench. The typical flow of the models is as follows: i) the device structure is built in Sentaurus Structure Editor, ii) the electrical properties of the device are modelled in Sentaurus Device and iii) the output is visualized in Sentaurus Visual. Depending on the type of problem and the balance of accuracy versus computation time, there are different methods for calculating the optical generation profile (TMM, FDTD and beam propagation method) or loading external profiles from file [152]. Several research groups have selected Sentaurus for their comprehensive solar cell models. Sozzi et al. studied the role of grain boundaries on the temperature behavior of shunt leakage currents in CIGS solar cells [153]. In their 2-D simulations, the grains are uniform in size and modeled as 2-nm thick layers with donor-type deep defects [153]. In another publication, the same group analyzed the role of Ga grading on the performance of CIGS solar cells with different Cu contents [154]. Metzger et al. performed time-resolved photoluminescence (TRPL) simulations on CIGS samples using a code in Sentaurus Device [155]. A Gaussian laser pulse was injected into CIGS, CdS/CIGS or ZnO/CdS/CIGS structures and the behavior of excess electrons (recombination, drift and diffusion) after the injection was studied. Using Sentaurus, Mansfield et al. engineered the Ga gradient of ultra-thin (< 500 nm) CIGS solar cells to achieve 15.2% certified efficiency at the experimental level. Their modelling provides a route towards 19% efficient CIGS solar cells with the same absorber thickness.

3

Quenching Mo optical losses in CIGS solar cells by a point contacted dual-layer dielectric spacer: a 3-D optical study

This chapter was published in *Optics Express** [156].

Abstract

A 3-D optical simulation was calibrated to calculate the light absorptance and the total reflectance of fabricated CIGS solar cells. Absorption losses at Mo / CIGS interface were explained in terms of plasmonic waves. To quench these losses, we assumed the insertion of a lossless dielectric spacer between Mo and CIGS, whose optical properties were varied. We show that such a spacer with low refractive index and proper thickness can significantly reduce the absorptance in Mo in the long wavelength regime and improve the device's rear reflectance, thus leading to enhanced light absorption in the CIGS layer. Therefore, we optimized a realistic two-layer MgF_2 / Al_2O_3 dielectric spacer to exploit i) the passivation properties of ultra-thin Al_2O_3 on the CIGS side for potential high open-circuit voltage and ii) the low refractive index of MgF_2 on the Mo side to reduce its optical losses. Combining our realistic spacer with optically-optimized point contacts increases the implied photocurrent density of a 750 nm-thick CIGS layer by 10% for the wavelengths between 700 and 1150 nm with respect to the reference cell. The elimination of plasmonic resonances in the new structure leads to a higher electric field magnitude at the bottom of CIGS layer and justifies the improved optical performance.

*N. Rezaei, O. Isabella, Z. Vroon, and M. Zeman, "Quenching Mo optical losses in CIGS solar cells by a point contacted dual-layer dielectric spacer: a 3-D optical study," *Optics Express*, vol. 26, no. 2, A39, Jan. 2018. doi: 10.1364/OE.26.000A39.

3.1 Introduction

CIGS PV technology enables high performance thin-film solar cells [14], [28], [44], [157], owing to its high absorption coefficient and gallium (Ga) content-based bandgap variation [72], [158]. To increase the PV market share of CIGS solar cells, larger and better industrial throughput is pursued by further improving the conversion efficiency and reducing cell-to-module losses. Also, for reducing material consumption (especially indium) and production time [36], [159], the absorber thickness should be reduced from the standard 2-3 μm [44], [72] to less than 1 μm .

However, reducing the absorber thickness results in less light absorptance, more recombination at the back contact (as more charge carriers are created near the back contact) and shunting problems [158]–[161]. Furthermore, Mo is a low-reflective metal [47], [162] and Mo / CIGS interface is a highly recombinative interface [82]. While the surface recombination problem has been addressed by using a thin Al_2O_3 passivating film [80], [84], the light management at such interface to compensate the current density loss in ultra-thin CIGS solar cells is still an issue, especially with industrially-compatible solutions in mind.

In both wafer-based and thin-film silicon technology, a low refractive index dielectric material (called *spacer layer*), placed between the metallic back reflector and the absorber, blue-shifts metal-related plasmonic resonances, increasing the short-circuit current density (J_{SC}) of the solar cell [163]–[165]. In this work, first, a physical explanation of the optical loss mechanism occurring at Mo / CIGS interface is provided. Then, borrowing the concept of dielectric spacer from Si PV technology, an intermediate dual-layer $\text{MgF}_2 / \text{Al}_2\text{O}_3$ stack [87], sandwiched between Mo back contact and CIGS layer, is designed and optimized. This was done by using a three dimensional (3-D) optical modelling approach based on the finite element method [72]. The insertion of such stack quenches the abovementioned optical losses, showing its effect in the improved implied photocurrent density (J_{ph}) in a solar cell with 1600 nm-thick CIGS layer. This dielectric stack is expected to boost also the V_{OC} , owing to the rear passivation of the CIGS layer, operated by the Al_2O_3 thin film [87], [166].

For carrier collection at the back contact, local point contacts are considered in an ultra-thin solar cell with a 750 nm-thick CIGS absorber. Both the dual-layer dielectric spacer and the geometry of the point contacts scheme are optimized, considering J_{ph} as the performance indicator.

3.2 Optical modelling

Ansoft® HFSS, which is a 3-D Maxwell's equation solver, was used for our optical studies. The optical constants of the materials composing different layers were imported into HFSS as inputs. The model was perpendicularly excited by means of plane waves through a Floquet port terminating a 300 nm-thick vacuum cushion above the top transparent conductive oxide (TCO). Master-Slave boundary conditions were enforced on the sides of the unit cell, respectively aligned with xz - and yz - planes. S-parameters were used for the calculation of total reflectance ($R = |S|^2$). HFSS proprietary meshing algorithm was deployed, resulting in higher number of tetrahedra per unit volume

in parts of the model with higher extinction coefficient and/or characterized by sudden change in real part of the refractive index (i.e. the more metallic and/or the thinner the layer is, the denser its mesh results). The absorptance in each layer was calculated as [72]:

$$A_i(\lambda) = \frac{1}{2} \varepsilon_0 \text{Im}\{\varepsilon_i(\lambda)\} \omega \int_{V_i} |\vec{E}(\lambda)|^2 dV \quad (3.1)$$

where λ is the wavelength of light, ε_0 is the electric permittivity *in vacuo*, ω is the angular frequency, \vec{E} is the electric field and ε_i and V_i are the relative electric permittivity and the volume of the i -th layer, respectively. The real and imaginary parts of relative electric permittivity of the materials used in the model are plotted in Figure 3.1.

For the simulated model to properly represent the fabricated solar cells, the simulation results should match the measured parameters with small deviation. In this respect, software calibration is an essential part of each simulation study. The thicknesses of the layers composing the simulated model were adjusted and the results (absorptance and reflectance spectra) were compared to the measured *EQE* and reflectance (R) of the baseline cells, fabricated at TNO [167]. The calibrated model is depicted in Figure 3.2(a).

According to the method established in [72], periodic truncated pyramids were used to model the natural roughness of the CIGS layer, while also the conformal growth of top layers on CIGS was considered. The period of features modelling roughness of CIGS absorber is 330 nm, equal to the correlation length of a CIGS sample measured by atomic force microscopy. The presence of nanotextures on Mo surface is considered by implementing nano-sized features with bottom base area and height size of $30 \times 30 \text{ nm}^2$ and 30 nm, respectively, and top base area of $20 \times 20 \text{ nm}^2$ at Mo / CIGS interface, as shown in Figure 3.2(a). It should be noted that no antireflective coating has been used in either the measured or the simulated devices.

In Figure 3.2(b), experimental $1-R$ and *EQE* spectra are overlaid on the simulated reflectance and absorptance spectra of the corresponding layers shown in Figure 3.2(a). In the wavelength range between 450 and 950 nm, the light absorptance in the simulated CIGS layer is more than the measured *EQE*, which can be due to carrier collection issues in the real device, resulting in recombination of electrons and holes before being collected at the terminals. The average difference between the simulated CIGS absorptance and measured *EQE* was 0.056, while this average difference in R was 0.03. These results are in line with previously published modelling works [72]. In this study, we worked on improving the optical properties of the Mo / CIGS interface, that is reached only by low energy photons. For this reason, our priority was to achieve a reasonable spectral matching between measured and simulated spectra in the long wavelength range. As Figure 3.2(b) shows, in the wavelength range between 900 and 1200 nm, the simulated $1-R$ and *EQE* spectra follow the same trend as their measured counterparts.

The presence of optical losses due to high absorption in Mo layer in the long wavelength range is well pronounced in Figure 3.2(b). These optical losses near the bandgap of CIGS deteriorate the generation of current in the solar cell and need to be quenched.

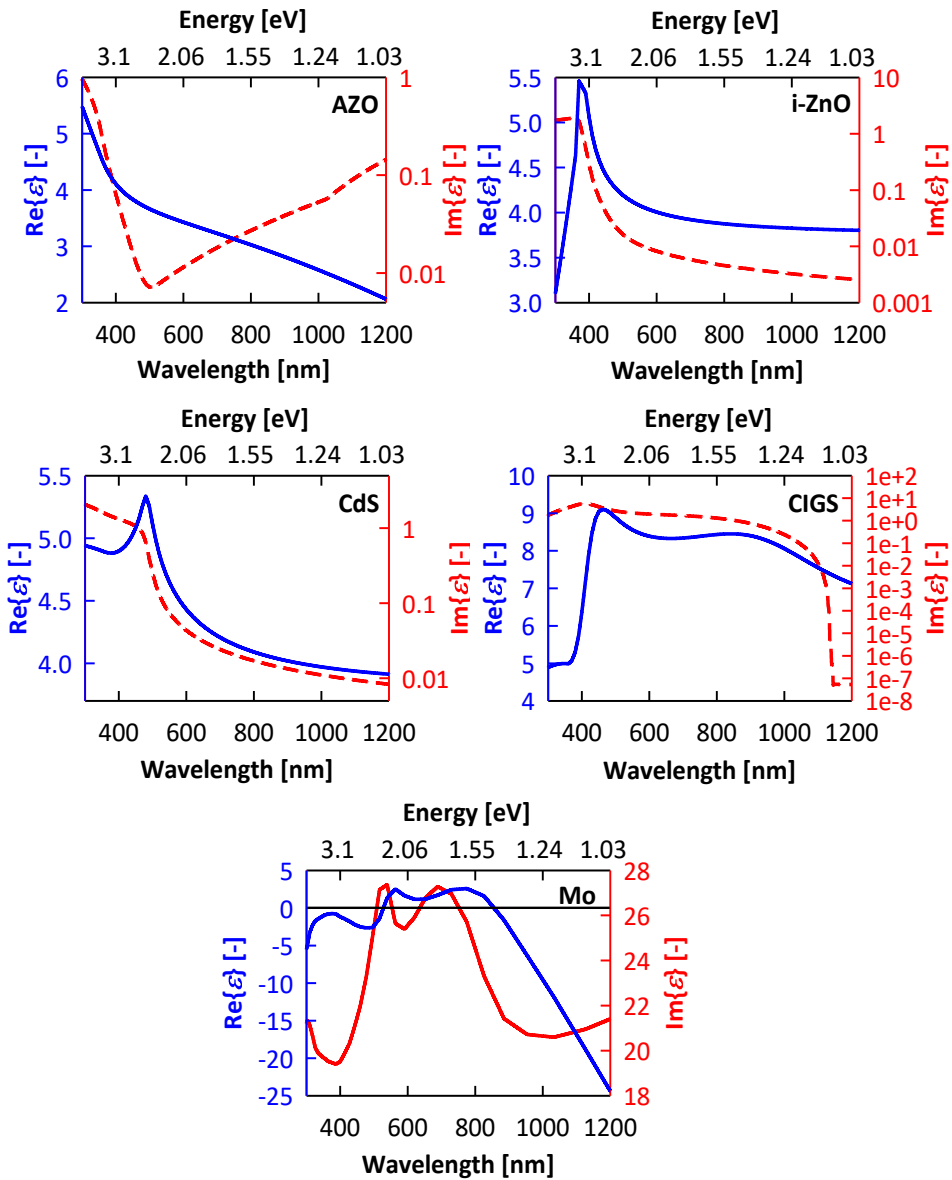


Figure 3.1: Real (solid) and imaginary (dashed) parts of relative electric permittivity of materials used for the calibrated model as a function of wavelength (the first four optical properties are obtained from [168] and Mo from [72]).

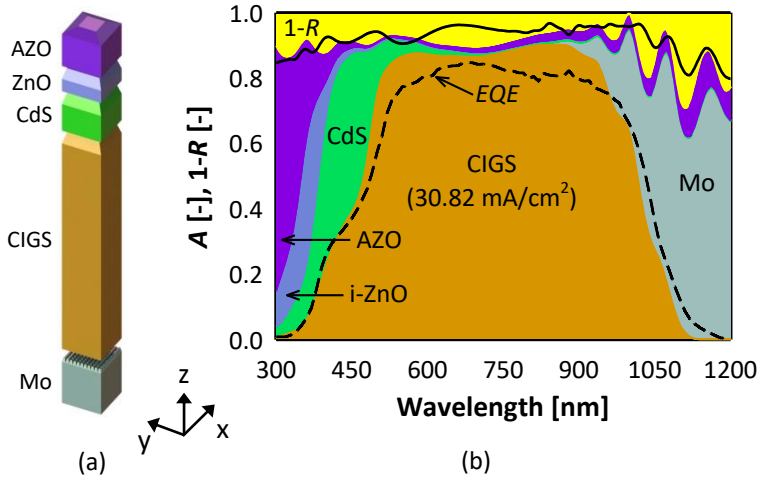


Figure 3.2: a) The schematic of the simulated solar cell. Thicknesses of layers from top to bottom are (in nm): 250, 60, 70, 1600 and 320. b) Simulation results are compared to the measured EQE and $1-R$ (dashed and solid black curves, respectively). Colored areas indicate absorptance in different layers of the structure.

3.3 Results and discussion

3.3.1 Nature of the optical losses at the back contact

The nature of optical losses at the interface between Mo and CIGS is addressed here. Depending on the polarization of light impinging on a metal / dielectric interface, the interaction with metal's electron plasma leads to the excitation of surface plasmons (SPs) [169]–[171]. SPs can either be *surface-bound* or *leaky*. Surface-bound SPs (also known as surface plasmon polaritons, SPPs) propagate along the interface with maximum amplitude at the surface and exponential decay in the direction normal to the interface. Necessary conditions for exciting SPPs are i) transverse magnetic polarized illumination light, ii) real parts of electric permittivity of the two media having opposite signs and iii) $|\text{Re}\{\varepsilon_m\}| > \text{Re}\{\varepsilon_d\}$, where ε_m and ε_d are the relative electric permittivity of metal and dielectric, respectively [171], [172]. In addition, since SPPs cannot be directly excited by light incident on a flat interface through the dielectric medium, certain phase-matching conditions must occur, such as having a textured interface between metal and dielectric [169], [170], [172]. In case of Mo / CIGS interface, considering the whole wavelength range from 300 nm to 1200 nm, the necessary conditions for the excitation of SPPs are met between 980 nm and 1200 nm (Figure 3.3(a)). On the other hand, if $|\text{Re}\{\varepsilon_m\}| < \text{Re}\{\varepsilon_d\}$, leaky SPs will be excited. In other words, when the $|\text{Re}\{\varepsilon_m\}|$ is smaller than the $\text{Re}\{\varepsilon_d\}$, the conditions for the excitation of a propagating wave component in the direction normal to the interface are met. It means that the wave propagates not only along but also normal to the interface

and effectively, the SPs are not confined to the interface. To distinguish between the wavelength regions of bound and leaky surface waves, the *dispersion relation*, which describes the wave vector component parallel to the interface, is compared to the light line in the dielectric.

In a Cartesian coordinate system, we assume two half spaces, one metallic and one dielectric, where the plane $z = 0$ coincides with the interface between the two media. The dispersion relation is a function of material properties and wavelength and can be derived as [169], [170]:

$$\beta(\lambda) = k_0 \sqrt{\frac{\varepsilon_d \varepsilon_m}{\varepsilon_d + \varepsilon_m}} \quad (3.2)$$

where β is the wave vector component parallel to the interface and $k_0 = 2\pi/\lambda$ is the wave vector of a photon *in vacuo*. In this relation, material properties such as damping and frequency dependency are considered. The light line in the dielectric represents instead the transverse component of the wave vector within a dielectric medium and is defined as $k_d = \text{Re}\{(2\pi/\lambda)\sqrt{\varepsilon_d}\}$. In Figure 3.3(b), the real part of β at a Mo / CIGS interface is compared to the light line of CIGS in the wavelength range $300 < \lambda < 1200$ nm. Due to the wavelength dependency of $\varepsilon_{\text{CIGS}}$, the light line of CIGS is not linear. The imaginary part of β , which is a measure of attenuation along the interface, is not shown here.

In Figure 3.3(b), two wavelength ranges can be individuated. In the first one, where only SPPs may exist between Mo and CIGS ($980 < \lambda < 1200$ nm), the dispersion curve lies on the right-hand side of light line. For a perfectly flat interface, as the wave vector of SPPs is larger than the wave vector of the light of the same energy propagating along the interface [169], no SPP is allowed. However, the presence of self-grown nano-roughness on Mo surface [173] fulfills the conservation of momentum and energy [172], making the excitation of SPPs in a real CIGS solar cell possible in this wavelength range. This phenomenon will be investigated further for one example wavelength in Section 3.4. The coupling of light into SPPs at the back contact surface is a source of optical loss, since these type of surface waves are strongly confined to the interface and will not lead to charge carrier generation in the absorber layer. In the second wavelength range ($300 < \lambda < 980$ nm), where only leaky surface waves can exist at Mo / CIGS interface, the wave vector of leaky SPs is smaller than the wave vector of light of the same energy propagating in CIGS. This means that even at a flat interface, these waves can be excited. Consequently, a large part of the light impinging on Mo surface, depending on the thickness of CIGS layer, will be absorbed in the Mo layer. Such optical loss is made even more serious, due to relatively higher real part of refractive index of Mo compared to more reflective metals such as silver, thus developing low reflectivity at the interface between Mo and CIGS.

3.3.2 Synthetic dielectric spacer

After having looked at the nature of optical losses at the back contact, an ideal lossless (i.e. *synthetic*) dielectric spacer is studied here to tackle this problem and boost the photo-current density of the solar cell. The electric permittivity (ε) and the thickness (d) of a synthetic material sandwiched between Mo and CIGS were therefore varied

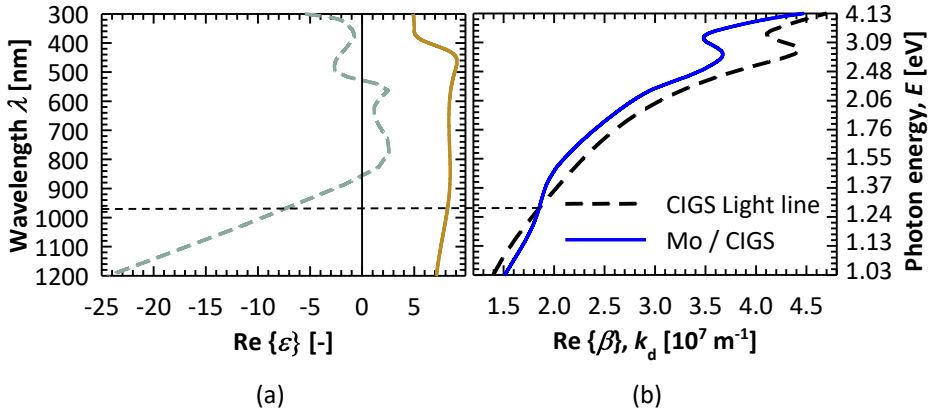


Figure 3.3: a) Real part of relative electric permittivity of Mo (dashed) and CIGS (solid), and b) SPP dispersion curve at the interface between Mo and CIGS (blue) half spaces compared to CIGS light line (dashed black) as a function of wavelength (i.e. photon energy).

in the wavelength range between 900 and 1200 nm and their influence on the optical performance of the solar cell was investigated. The choice of this wavelength range is related to the absorptance in Mo in a 1600 nm-thick CIGS solar cell, as shown in Figure 3.2(b).

For the remainder of this chapter, a *synthetic* material is an ideal material with the imaginary part of the electric permittivity forcibly set to zero at all wavelengths ($\text{Im}\{\varepsilon\} = 0 \forall \lambda$), while a *real* material is an actual material, characterized by its own wavelength-dependent complex electric permittivity, ε . With respect to the calibrated model, aside the insertion of the synthetic dielectric spacer, all other structural parameters were kept the same.

J was employed as performance indicator. This parameter is either the photocurrent density generated in the absorber layer or the lost photocurrent density as a result of absorption in each supporting layer. J can be calculated as follows [104]:

$$J_i = -q \int A_i(\lambda) \Phi_{\text{ph}}(\lambda) d\lambda \quad (3.3)$$

where i is the i -th analyzed layer, q is the electric charge, $A_i(\lambda)$ and $\Phi_{\text{ph}}(\lambda)$ are the wavelength-dependent absorptance and AM1.5 photon flux [8], respectively. In this regard, $J_{\text{ph}} = J_{\text{CIGS}}$. Likewise, the current loss due to the total reflection (J_R) is calculated by replacing $A_i(\lambda)$ with $R(\lambda)$ in Equation 3.3. Figure 3.4 depicts a visual rendering of the modelled solar cell endowed with a dielectric spacer.

In Figure 3.5, contour plots of the absorptance (integrated as current density) in Mo and CIGS ($d_{\text{CIGS}} = 1600$ nm) in the wavelength range between 900 nm and 1200 nm as a function of spacer thickness and electric permittivity are shown. It can be concluded that the lower the refractive index of the spacer layer ($n = \sqrt{\varepsilon}$) is, the higher the



Figure 3.4: Modified model with the synthetic dielectric spacer layer. Thicknesses of different layers (in nm) from top to bottom are as follows: 250, 60, 70, 1600, d and 320. The thickness d of the spacer layer was varied between 20 nm and 170 nm.

absorptance is in the CIGS layer and vice versa in the Mo layer. Real low refractive index dielectric materials suitable as spacer are, for example, MgF_2 , LiF , SiO_2 , Al_2O_3 and TiO_2 . Since the field reflected at the interface metal / dielectric spacer forms a standing wave [174], it is important to set the proper thickness of the spacer, so that the intensity of the wave travelling back to the absorber is at maximum. As Figure 3.5(b) shows, for each spacer material, there is an optimal thickness at which J_{ph} can be maximized. This is in agreement with the findings of Holman et al. about the effect of spacer thickness on the internal reflectance improvement of Si-based solar cells [165], stating that beyond a certain spacer thickness, the internal reflection (and hence, the photon absorptance in the absorber) does not improve anymore.

3.3.3 Al_2O_3 vs MgF_2

In CIGS solar cell architecture, with the inspiration from Si-based passivated emitter and rear cell (PERC) technology [166], a 10-nm thick dielectric spacer is used to passivate the rear surface of CIGS, leading to an increase in V_{OC} (PERC-like technology). Al_2O_3 with an electric permittivity of 2.7 (or $n = \sqrt{\epsilon} = 1.64$) at $\lambda = 1000$ nm is currently the state-of-the-art material, from electrical point of view, for rear surface passivation of CIGS solar cells [82], [86]. However, as it can be concluded from our theoretical optical study (Figure 3.5(b)), a very thin layer of Al_2O_3 cannot perform well in increasing the J_{SC} with respect to other materials with refractive indices less than that of Al_2O_3 . MgF_2 with $\epsilon = 1.87$ (or $n = \sqrt{\epsilon} = 1.38$) at $\lambda = 1000$ nm is a good candidate for this purpose.

In Figure 3.6, when Al_2O_3 with *real* material properties [175] is used as the spacer, the integrated absorptance in the wavelength range between 900 and 1200 nm in different layers of CIGS solar cell as a function of d is shown. The first column indicates the simulation results of the reference cell in which no spacer is implemented. The

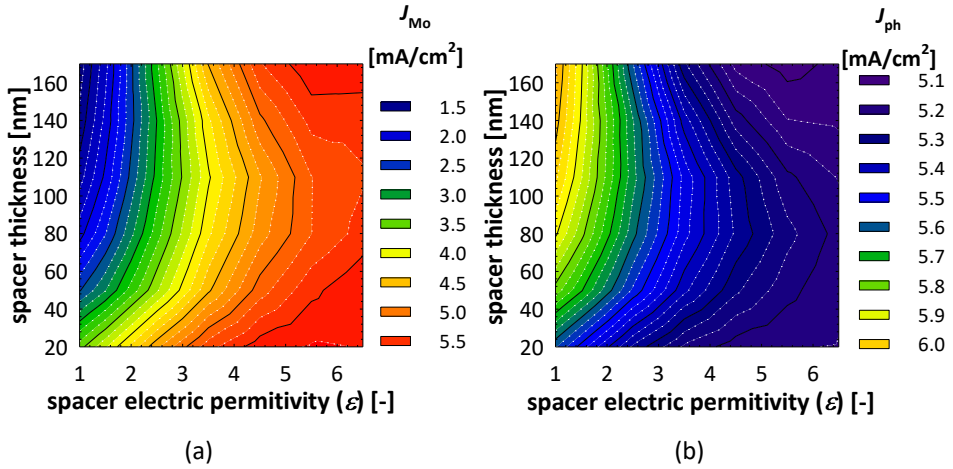


Figure 3.5: Contour plots of the synthetic dielectric spacer optimization: a) integrated Mo absorptance loss (J_{Mo}), and b) implied photo-current density in CIGS layer (J_{ph}) versus spacer thickness and electric permittivity for the wavelength range 900-1200 nm.

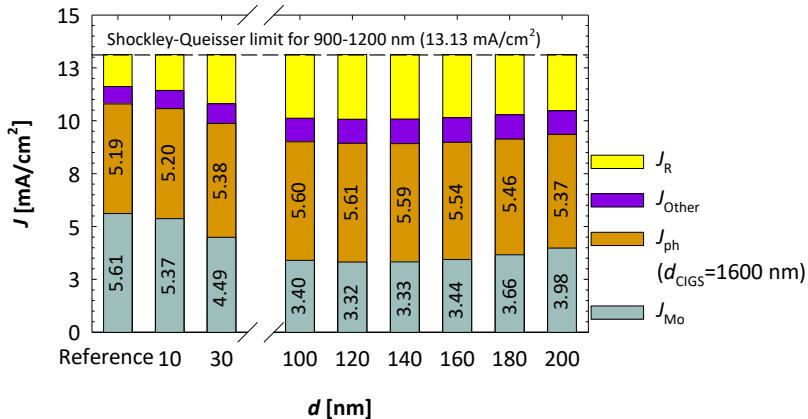


Figure 3.6: Integrated absorbance (or photocurrent density) in different layers of CIGS solar cell as a function of spacer thickness d in the wavelength range between 900 and 1200 nm when Al_2O_3 is used as the spacer.

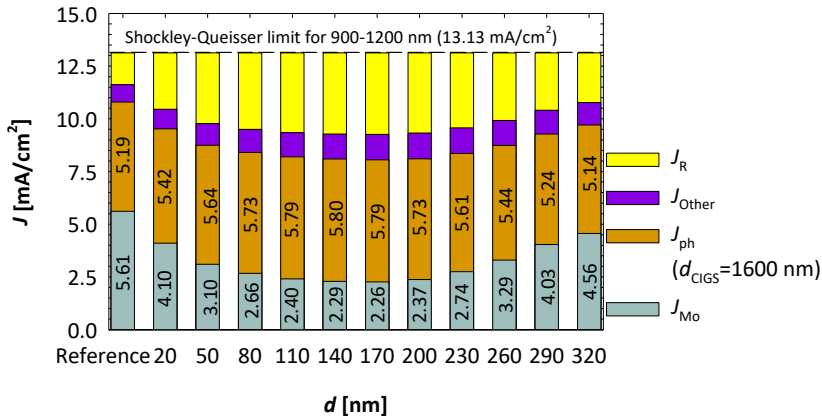


Figure 3.7: Integrated absorptance (or photocurrent density) in different layers of CIGS solar cell as a function of spacer thickness d in the wavelength range between 900 and 1200 nm when MgF_2 is used as the spacer.

results of Figure 3.6 confirm that a thin layer of Al_2O_3 spacer (10 nm, for instance) does not lead to a significant increase in J_{ph} . Nevertheless, for the optimal thickness of 120 nm, an improvement of 0.42 mA/cm² in J_{ph} can be achieved. On the other hand, Figure 3.7 shows that when MgF_2 [176] is used as the spacer material, at the optimal thickness of 140 nm, the enhancement of J_{ph} is 0.61 mA/cm², confirming the statement that a material with low refractive index and lower than that of Al_2O_3 is better for quenching Mo optical losses at the rear side of the solar cell [163]. These results are in good agreement with the findings of Poncelet et al. in [35], where a dielectric spacer is used to increase the rear reflectance of CIGS solar cells. However, we will show that when a different figure of merit than reflectance is used and for cells with thin CIGS layers, the optimized spacer thickness might be different.

A proper way of combining the advantages of Al_2O_3 and MgF_2 is to make a double-layer, in which an MgF_2 spacer layer with optimized thickness is covered by a thin Al_2O_3 layer (10 nm), potentially acting as a passivator to enhance V_{OC} (see Figure 3.8). The feasibility of such a stack, in combination with local point contacts, has been shown in [87].

As mentioned before, the thickness optimization of the spacer is of great importance. Hence, the thickness of MgF_2 in the new stack was optimized to achieve the maximal J_{ph} . The results show that despite the presence of a 10 nm-thick Al_2O_3 layer on top of MgF_2 , 140 nm is again the optimal thickness leading to the absorptance spectrum shown in Figure 3.9(a). In this figure, the increase (decrease) of the absorptance in CIGS (Mo) in the presence of the spacer can be clearly recognized. The absorptance in the short wavelength range is not influenced by the presence of the spacer, since, for the absorber thickness of interest, the high-energy photons do not reach the back contact. A 0.63 mA/cm² improvement in J_{ph} for the whole wavelength spectrum of interest can be obtained with this configuration (see Figure 3.9(b)). This is not a

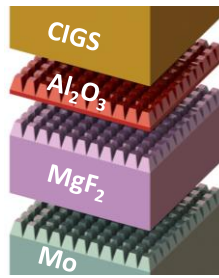


Figure 3.8: The schematic of the two-layer dielectric spacer / passivating stack consisting of MgF_2 (140 nm) and Al_2O_3 (10 nm) placed between Mo back contact and CIGS absorber.

marginal improvement, given that it is achieved by simply depositing two layers on Mo and not by texturing the backside of the CIGS device, potentially leading to the growth of low quality CIGS and/or parasitic absorption.

It should be noted that in such structure, the total reflection will also increase, basically hindering the net effect of quenching Mo-related losses. This is the result of the increase in the secondary escape reflection [177], representing the photons that enter the cell, undergo one or more internal reflections and finally escape from the front side of the cell without being absorbed.

3.3.4 Electric field investigation

One of the main advantages of 3-D optical simulations over 1-D simulations is the possibility to observe electric field distribution in every point of the structure. In order to show that the enhancement of current in long wavelength regime is partly resulted from the reduction of plasmonic resonances [165], the magnitude of the electric field ($|\vec{E}|$) is evaluated. Particularly, $|\vec{E}|$ is sampled along the central line of the cell at $\lambda = 1020$ nm, corresponding to the third peak of the solid blue curve in long wavelength range in Figure 3.9(a), with and without the spacer for transverse magnetic (TM) light illumination. We looked at this polarization, because surface plasmons can only be excited by TM polarized light [165], [170], although in this case, due to the symmetry of the structure, the difference between TE and TM polarizations is not pronounced.

Figure 3.10(a) shows that by inserting the two-layer spacer, $|\vec{E}|$ is increased along the cell, which according to Equation 3.1, leads to the absorptance enhancement. The excitation of surface plasmons at Mo / CIGS interface at $\lambda = 1020$ nm can be noticed from the peak of electric field at that interface in Figure 3.10(b), which has an almost exponential decay in CIGS (linear decay in logarithmic scale). This observation is in agreement with our discussion in section 3.1. This lossy optical mechanism prevents the reflection of photons from Mo surface back into the absorber, a phenomenon similar to plasmonic losses in Si-based solar cells [178]. It should be noted that according to our studies, this phenomenon could not have been observed, if the natural roughness of

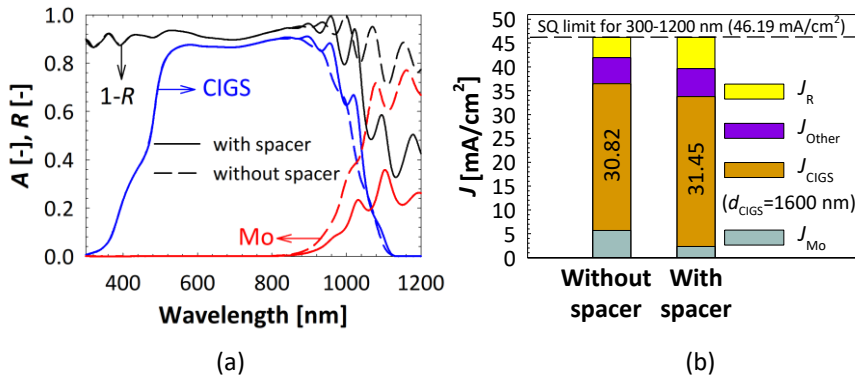


Figure 3.9: a) The absorptance in 1600-nm thick CIGS (blue) and Mo (red) and $1-R$ (black) for the reference cell (dashed) and the cell with two-layer spacer (solid), and b) the integrated absorptance in different layers of CIGS solar cell for the wavelength range between 300 and 1200 nm.

Mo was not included in the model, which is in agreement with the necessary conditions for the excitation of plasmonic waves. As indicated in Figure 3.10(c) instead, the plasmonic resonance is quenched in the modified structure endowed with MgF_2 / Al_2O_3 spacer. In fact, the peak in \vec{E} at Mo surface is disappeared, explaining the peak in CIGS absorptance in Figure 3.9(a) at the corresponding wavelength.

3.3.5 Point contact optimization

The proposed structure in its current form cannot be a working solar cell, unless the absorber layer is connected to Mo [81] to enable hole collection. Therefore, local point contacts with circular cross sections are added to the structure (see Figure 3.11(a)). The radius and spacing between these contacts should be optimized for maximal J_{ph} . However, it should be kept in mind that in a local point contact scheme, the charge carriers move in lateral direction to finally reach the back contact. Therefore, the point contact spacing should be less than twice the minority carrier diffusion length in CIGS layer (between 0.5 and $2 \mu m$ [179]) to prevent charge carrier recombination in the absorber.

As mentioned above, sub-micron CIGS layers are of particular interest for a variety of reasons. Accordingly, our point contact scheme was optimized for a cell with 750-nm thick CIGS absorber, re-finding first the best MgF_2 thickness and investigating then, the different geometric configurations. Due to less absorber thickness, higher energy photons with wavelengths down to 700 nm can reach the back contact. That is why in this part of the contribution, results attain the wavelength range between 700 nm and 1150 nm, where the upper bound was chosen based on measured EQE spectrum of the baseline ultra-thin CIGS solar cell. We found that the optimal thickness for MgF_2 is 100 nm, which in combination with a 10-nm thick passivating Al_2O_3 , leads

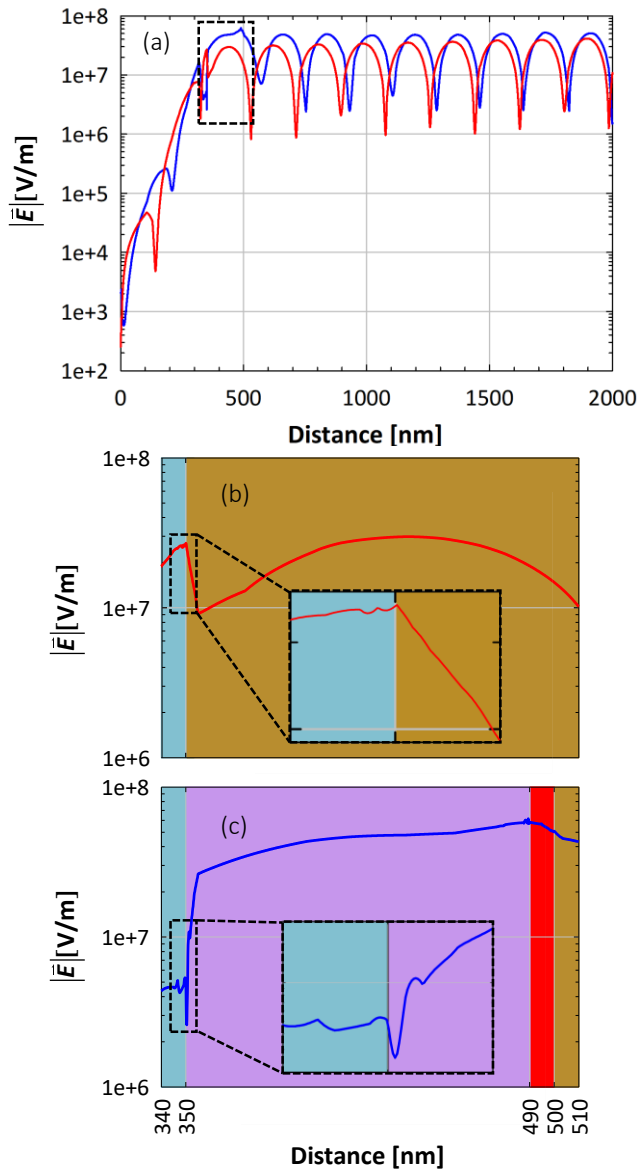


Figure 3.10: From top to bottom, magnitude of the electric field $|\vec{E}|$ along the central line of the solar cell at $\lambda = 1020$ nm as a function of the distance from the back side of the Mo layer for TM illumination: a) comparison between the reference cell (red) and the cell with $\text{MgF}_2 / \text{Al}_2\text{O}_3$ spacer (blue), b) a closer look at the area shown in the dashed rectangle for reference cell and c) the same but for the cell with $\text{MgF}_2 / \text{Al}_2\text{O}_3$ spacer. The background colors indicate different layers: Mo (greenish-grey), MgF_2 (pink), Al_2O_3 (red) and CIGS (brown).

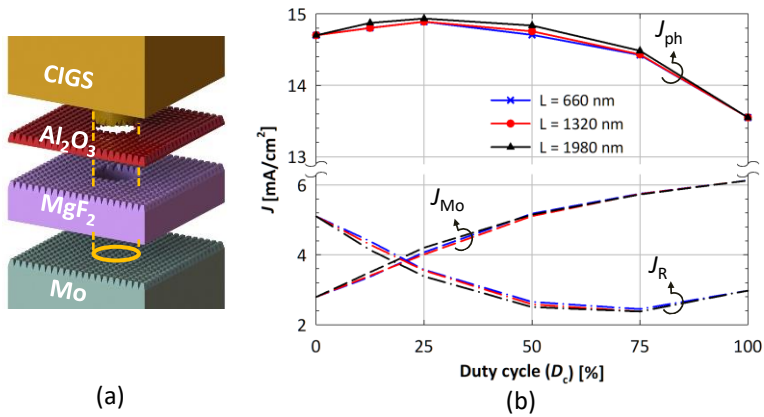


Figure 3.11: a) Dual-layer spacer / passivator consisting of MgF₂ (100 nm) and Al₂O₃ (10 nm), including the point contact scheme; b) implied photocurrent density and integrated Mo absorptance and reflection loss for $700 < \lambda < 1150$ nm as a function of Duty cycle (D_c) for unit cell lengths of two, four and six times larger than the correlation length of CIGS surface texture.

to 1.15 mA/cm² increase in J_{ph} (or 8.5% improvement for $700 < \lambda < 1150$ nm) compared to the reference cell. The optimized value of MgF₂ thickness is different from the one obtained in [35], because of the different performance indicator (J_{ph} in our case instead of rear reflectance). In fact, increasing the rear reflectance will lead to the improvement of J_{ph} , but not all the reflected light can be absorbed in the absorber and the maximal value of J_{ph} is not necessarily accompanied with maximal rear reflectance. In addition, the optimization in [35] was performed for $800 < \lambda < 1100$ nm, independently from CIGS thickness. In reality, CIGS thickness plays an important role in the wavelength range of photons reaching the back contact, causing the optimization regime vary for different absorber thicknesses.

As for the investigation on different geometric configurations, two structural parameters were varied: the unit cell size (L) and the Duty Cycle (D_c). D_c represents the area coverage of point contacts and is defined as $\pi r^2 / L^2$ in which r is the radius of the point contact. It should be noted that L is the point contact period too. The smallest value of L is 660 nm, which is equal to two times larger than the correlation length of as-grown textures on CIGS surface. In Figure 3.11(b), J_{ph} and integrated Mo absorptance and reflectance losses as functions of D_c are shown. 0% and 100% D_c correspond to full passivation and no passivation of the back contact, respectively. It can be observed that there is a trade-off between Mo absorptance and total reflectance. Current density loss due to Mo absorptance is minimized when its surface is fully covered with the spacer and increases by increasing the area coverage of point contacts, which is in agreement with the analyses in previous sections.

According to a previous study on diffraction gratings [180], the intensity of diffracted modes depends on duty cycle of the grating and, for $D_c = 50\%$, all diffracted modes

are excited altogether. This means that the light is diffused in higher angles (with respect to the normal to the interface). This increases the optical path length of light inside the absorber and, hence, results in higher chance of light absorption. By looking at the point contact structure as a diffraction grating, the same interpretation seems to be realistic. Although, for $D_c = 50\%$ more light is diffused outside the escape cone of the CIGS layer, this is counterbalanced by more Mo absorptance. Accordingly, for less D_c values, less Mo absorptance is balanced out by more light escaping the solar cell (more total reflection). It can be concluded from Figure 3.11(b) that these two parameters reach an optimal point close to $D_c = 25\%$, leading to maximal light absorptance in CIGS layer.

The presence of a similar trend for different point contact periodicities shows the scalability of the structure. It means that it is possible to fabricate this structure using techniques that are cheaper than e.g. e-beam lithography. For the case of $L = 1980$ nm, the current density improvement at optimal D_c is 1.39 mA/cm² (or 10%) for the wavelengths between 700 and 1150 nm. The simulations for the whole spectral range of interest indicate that J_{ph} is improved by 1.45 mA/cm², from 28.04 to 29.49 mA/cm², which can be translated to a 5.27% optical improvement.

3.4 Conclusions

An optical model of a CIGS solar cell using 3-D Maxwell's equation solver based on the finite element method was presented. The software was calibrated with the measured *EQE* and *R* spectra of the reference solar cells and a qualitative agreement was obtained. The natural textures of different layers were modeled by truncated pyramids.

The possibility of the excitation of SPPs at Mo / CIGS interface was investigated by studying the dispersion curve. Results show that for a wide wavelength range in the visible part of the spectrum, leaky surface waves can be excited at a flat Mo / CIGS interface. In the long wavelength range, on the other hand, the presence of natural roughness on Mo facilitates the excitation of surface-bound plasmons, dramatically reducing the *EQE*.

Borrowing the concept of dielectric spacer from Si PV technology, the insertion of a synthetic low refractive index dielectric layer between Mo and CIGS was optically studied. It was shown that i) such a spacer will quench the optical losses caused by high absorptance in Mo and plasmonic losses in long wavelength regime and ii) an optimal thickness for the dielectric spacer exists. The capability of Al₂O₃, which is the state-of-the-art material in CIGS-based PERC-like structures, in enhancing J_{ph} was compared to that of MgF₂. The results indicate that the latter - with the optimal thickness of 140 nm - performs better than Al₂O₃.

Then, a two-layer spacer / passivator consisting of MgF₂ and Al₂O₃ was designed and the thickness of MgF₂ was optimized for maximum J_{ph} . An absolute increase in J_{ph} by 0.63 mA/cm² for the whole visible spectrum can be expected with the proposed structure, notwithstanding increased reflectance losses. These are, in fact, closely related to augmented absorptance in CIGS, when Mo optical losses are quenched. A study on the magnitude of the electric field proves that the plasmonic losses are

quenched by the two-layer spacer, giving rise to better light absorptance in the CIGS layer.

Finally, point contacts were inserted into the cell structure endowed with a 750-nm thick CIGS absorber and their area coverage was optimized for maximal implied photocurrent density. The results indicate that the trade-off between current loss in Mo and total reflection is balanced out for $D_c = 25\%$, leading to improvement of J_{ph} by 10% compared to the reference cell for the wavelengths between 700 and 1150 nm.

4

A multi-layer wideband antireflection coating

This chapter was published in *Solar Energy** [181]

Abstract

The optical losses associated with sub-micron absorbers in CIGS solar cells can be reduced by light management techniques. 3-D optical modelling was used to optimize the light in-coupling and internal rear reflectance in a 750-nm thick CIGS reference solar cell. At the front side of the solar cell, an effective medium approximation (EMA) approach for describing optical properties of a MgF_2 -based anti-reflection coating (ARC) was applied. Taking reflectance as the cost function and sequential nonlinear programming as the optimization algorithm, an optimal porous-on-compact double-layer ARC was determined. This led to a wideband light in-coupling with a 6.8% improvement in the photo-current density (J_{ph}) with respect to the reference solar cell without ARC. Considering the variation of the sunlight direction due to day and seasonal changes, different light incidence angles were investigated. The results indicate that in this case, our designed double-layer ARC outperforms the standard compact MgF_2 single-layer ARC. By using the EMA approach, the amount of computational memory can be reduced by a factor of 30, shortening the simulation time from four days to one hour. At the rear side of the cell, a point-contacted $\text{MgF}_2 / \text{Al}_2\text{O}_3$ reflector, in combination with our proposed front ARC, enhances the J_{ph} by 11.3% considering the same reference solar cell. Compared to a much thicker cell (1600-nm thick absorber) without light management structures, our front-and-rear optical approaches more-than-compensate optical losses resulting from using thinner absorbers. This design is suitable for industrial uptake and practical to realize. Additionally, the approach of using EMA for double-layer ARC optimization is innovative with respect to other ARC approaches applicable to not only chalcopyrite photovoltaic technologies.

*N. Rezaei, O. Isabella, Z. Vroon, and M. Zeman, "Optical optimization of a multi-layer wideband anti-reflection coating using porous MgF_2 for sub-micron thick CIGS solar cells," *Solar Energy*, vol. 177, no. August 2018, pp. 59–67, 2019. doi: 10.1016/j.solener.2018.11.015.

4.1 Introduction

With a record efficiency of 23.35% [27], CIGS solar cells still need to get closer to their theoretical efficiency limit [8], [182]. This means that light management techniques can still be improved, which along with the improvement of the electrical performance, lead to higher conversion efficiency. Given the fact that in general, a large part of the optical loss is due to the front reflectance, the usage of anti-reflection coatings (ARC) for improving the light in-coupling appears crucial. When it comes to the ARC topic, different techniques can be employed to reduce the light reflection. The simplest approach is a single-layer film with a thickness of quarter of light's wavelength and a real part of the refractive index (n) between that of the air and the solar cell's top layer [8], [183]. In addition, the film should be as less absorptive as possible, ideally lossless.

MgF₂ with thicknesses of about 100 nm is the conventional ARC material for CIGS solar cells, which is normally evaporated on top of the cell [67], [68], [184]–[186]. High thermal stability, low n , durability, insignificant absorption in the wavelength range of interest and resilience against water makes MgF₂ a good candidate for anti-reflection purposes [187].

Nonetheless, single-layer ARCs are effective only in a small range of wavelengths and angles of incidence (AOI). Hence, wideband anti-reflection systems that are less sensitive to the AOI should be used to enhance the optical performance of solar cells. This is possible by gradually changing n using sub-wavelength textures and/or by multi-layer ARC [69]. Both of these techniques are based on Rayleigh effect, according to which when the light impinges a medium with graded n , reflectance is reduced and the light beam bends while travelling in the medium [188]. Likewise, a sub-wavelength-textured surface is seen by the light as if it has graded n , which - in combination with multiple internal reflections - promotes light trapping in the solar cell [69], [189]. The effect of textured transparent conductive oxide (TCO) in light trapping in CIGS solar cells was theoretically studied in the past by Campa et al. [70]. The results indicated that the textured air / front TCO interface improves the quantum efficiency merely as a result of better AR effect, rather than improved scattering. Dahan et al. showed from theoretical and experimental points of view that texturing ZnO:Al (AZO) can improve the short circuit current density (J_{SC}) of a CIGS solar cell by 5 to 10% [190]. Yet, the presence of naturally grown roughness [191] on the surface of CIGS which is conformally transferred to the subsequent top layers [72], [156] gives an intrinsic advantage to CIGS PV technology, leaving more room for studying other anti-reflection methods to be combined with it.

In this respect, our focus is more on grading n through multi-layer ARCs as viable approach. For example, the addition of a more than 2 μm thick double-layer of SiO₂ / Al₂O₃ on the surface of AZO was studied and a 2.3% increase in J_{SC} was reported as a result of anti-reflection effects [192]. Grading n can also be done by introducing a gradient level of porosity in the same ARC material instead of using different materials. In silicon PV technology, different porous materials such as silicon dioxide, silicon and magnesium fluoride, developed with a variety of methods, have been widely investigated for the same purpose [193]–[197]. However, to our knowledge, this topic has not been studied in the field of CIGS PV technology.

The development of ultra-low refractive index using thermally induced porosity in MgF_2 -based films has been reported in [187], [198]. Accordingly, a multi-layer MgF_2 -based optical coating with the average pore size of 10 to 20 nm with n down to 1.08 was fabricated. The significantly low n achievable with this method makes it an interesting candidate for the design of a multi-layer wideband ARC for CIGS solar cells. On the other hand, from optical perspective, the inherent complexity of modelling a porous layer endowed with sub-wavelength features calls for an equivalent approach, such as the effective medium approximation (EMA) [199]. This technique will be explained in more details in next section.

In the following, we design and optimize a double-layer wideband MgF_2 -based ARC for a 750-nm thick CIGS solar cell using a 3-D optical modelling tool. For this purpose, in order to achieve better computational performance, we deploy the EMA approach and compare it with the model employing a true porous layer, demonstrating excellent predictive power. Also, we study how the AOI of the light impacts on the optical performance of the CIGS solar cells endowed with our multi-layer ARCs. Finally, combining our multi-layer ARC design with the point contacted double-layer spacer design from our previous study [156], we devise a light management scheme (light in-coupling + light scattering + low loss back reflector) to boost the optical behaviour of a sub-micron CIGS solar cell compared to a more standard 1.6- μm thick CIGS solar cell.

The following points highlight the importance of the proposed optimization scheme:

- As mentioned above, 3-D optical modelling provides an opportunity to obtain the overall optical performance of the solar cell under different types of light illumination (polarization, angle of incidence, etc.).
- Optical performance improvements at both short and long wavelength ranges are addressed separately.
- Using EMA in combination with suitable periodic boundary conditions, the simulation time and the computational memory are reduced significantly.
- A wideband antireflection effect with low dependency on AOI is obtained without the need for etching the absorber layer, indicating the cost-effectiveness of the structure.
- This approach is applicable to other thin film solar cell technologies, such as CdTe, BaSi_2 [200], [201] and perovskites to name a few [202].

This study is focused on sub-micron CIGS solar cells, for which the optical loss due to ultra-thin absorber should be compensated by light management strategies. Since this work aims at giving guidelines for design and optimization purposes, a few considerations are made:

- The model is valid for lab-scale CIGS solar cells without encapsulating layers. In case of encapsulation, the designed ARC can be placed on glass, provided that further optimizations are done and a multi-optical regime software platform [116], [203]–[205] is used.

- According to [198], in the fabrication process of porous MgF_2 -based films, the samples should go through a flash thermal heating step at 450°C for about 10 minutes. In a standard CIGS solar cell structure, the CdS buffer layer will degrade and inter-diffuse with CIGS at this high temperature [75]. Therefore, from experimental point of view, this ARC scheme can be realized if alternative thermally-stable buffer layers are used and/or porous MgF_2 films are developed at lower temperatures.

4.2 Methodology

In this work, Ansoft HFSS has been used for modelling a 750-nm thick CIGS solar cell. The typical layer stack of the reference cell is composed of (from bottom to top): Mo (150 nm) / CIGS (750 nm) / CdS (70 nm) / i-ZnO (60 nm) / AZO (230 nm). Our modelling platform was preliminary calibrated to guarantee that the simulation results accurately represent the experimentally measured EQE and R of the baseline solar cells fabricated at Solliance [38]. This was done by deploying as-measured optical properties of involved layers, by adjusting the layers' thickness and by approximating surface morphology until a reasonable matching with the measured spectra was achieved (Figure 4.1). The unit cell size (330 nm) in the model is within the lateral correlation length of CIGS grains, measured by atomic force microscopy. The cell is illuminated perpendicularly by AM1.5G spectrum. The wavelength range of interest is 300 nm to 1200 nm. Plane wave excitation via Floquet port formalism and Master/Slave boundary conditions were used to excite the cell structure and model its periodicity, respectively. Although this is a simplification of the realistic case with random natural grains, it reduces the simulated volume and computational time and memory significantly, without harming the acceptable accuracy of the model. The overestimation of absorptance in mid-wavelength range (see Figure 4.1(c)) can be due to poor charge collection in the real solar cell. More details about the simulation settings and modelling of surface morphology can be found in **Chapter 3** [156]. This validation is instrumental for our further analysis and development of the reference solar cell, as reliable results are of great importance. In the following, given the successful calibration of the simulator in carrying out EQE and R spectra as in measured devices, we shall use EQE as synonym of absorptance spectrum in CIGS absorber layer.

In FEM, the volume of the simulated model is discretized (meshed) with tetrahedrons. The size of mesh is dependent on the relative size of different components with respect to each other and to the wavelength of light. The smaller the mesh elements are, the larger the required computational memory (random access memory, RAM) is [104]. Therefore, in general, the optimization of porous layers by means of FEM-based 3-D Maxwell's equation solvers with the available computational tools is cumbersome, if not impossible. According to the EMA theory of Bruggeman [199], a porous material with pores much smaller than the wavelength of light can be approximated by an equivalent optically-isotropic medium. In case of low-loss materials (i.e. when the imaginary part of the refractive index k , the extinction coefficient, is much smaller than n), the real part of electric permittivity can be approximated by $\text{Re}\{\varepsilon\} = n^2 - k^2 \approx n^2$ and the EMA equation is [206]:

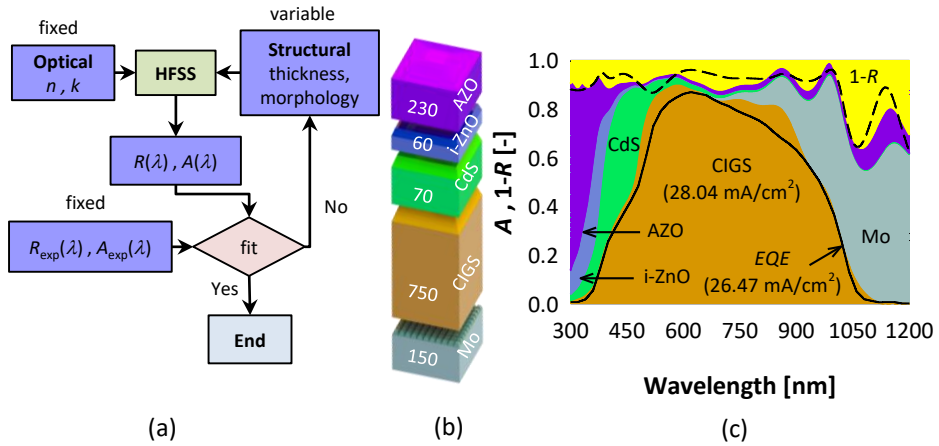


Figure 4.1: a) Flowchart of the calibration procedure with HFSS reference model: input/output (purple), process (green), condition (pink) and end (light blue). b) The simulated reference solar cell. The numbers in the blocks show the layer thicknesses in nm. c) Comparison between the simulation results and measured EQE and $1-R$ spectra (solid and dashed black lines, respectively). Each colour is an indication of absorptance in each layer or reflectance.

$$(1 - p) \frac{\text{Re}\{\varepsilon_d\} - \text{Re}\{\varepsilon_e\}}{\text{Re}\{\varepsilon_d\} + 2\text{Re}\{\varepsilon_e\}} + p \frac{1 - \text{Re}\{\varepsilon_e\}}{1 + 2\text{Re}\{\varepsilon_e\}} = 0 \quad (4.1)$$

where ε_d and ε_e are the electric permittivity of the porous and effective media respectively, and p is the volume fraction of pores. By using EMA theory in our HFSS models, the required simulation time and RAM were significantly reduced, since compact easy-to-mesh layers could be simulated. The validity of this approximation was then tested by i) calculating p from Equation 4.1, ii) controlling the introduction of pores into the ARC layer with the realistic optical constants and optimal thickness, and finally, iii) simulating for once a stack with non-compact but porous layers endowed with spherical voids placed randomly in the simulated model.

Natural nanotextures at Mo / CIGS interface, which influence the long wavelength performance of the cell [156], are not included in this optimization step. The validity of this assumption was assessed after the optimization and the results will be shown in the following sections.

4.3 Contribution of the front reflectance in optical losses

Figure 4.2(a) shows how much and where light is absorbed or reflected in a 750-nm thick CIGS solar cell when illuminated by AM1.5 light, calculated according to

Equations 4.2 and 4.3 [133]:

$$\bar{A}(\%) = \frac{\int_{300}^{1200} A(\lambda)\Phi_{\text{ph}}(\lambda)d\lambda}{\int_{300}^{1200} \Phi_{\text{ph}}(\lambda)d\lambda} \times 100\% \quad (4.2)$$

$$\bar{R}(\%) = \frac{\int_{300}^{1200} R(\lambda)\Phi_{\text{ph}}(\lambda)d\lambda}{\int_{300}^{1200} \Phi_{\text{ph}}(\lambda)d\lambda} \times 100\% \quad (4.3)$$

where λ is the wavelength of light, $A(\lambda)$ is the absorptance in different layers of the solar cell, $\Phi_{\text{ph}}(\lambda)$ is AM1.5 photon flux and $R(\lambda)$ is the reflectance spectrum. Each value in the figure represents the ratio between absorptance in each layer or reflectance integrated as photo-current density [156] and the maximum attainable photo-current density in the 300-1200 nm wavelength range, also known as Shockley-Queisser (S-Q) limit [89]. As indicated in Figure 4.2(a), a considerable value of light is lost due to reflectance (11.15%). The reflected light from a solar cell consists of two different contributions: i) the reflection from the front side (R_{front}) and ii) the escaping light (R_{esc}), which is the light reaching the back contact, having a number of round trips in the solar cell stack and eventually escaping from the front side of the cell [156], [177]. The latter contributes only to the longer wavelength part of the reflectance spectrum, whose emerging wavelength depends on the thickness and the absorption coefficient of the absorber. In case of a 750-nm thick absorber, this onset happens at 640 nm, as shown in Figure 4.2(b). In this figure, the total reflectance spectrum (R_{tot}) is plotted against R_{front} as function of wavelength. The latter spectrum was simulated for a solar cell comprising of similar front layers and an ultra-thick CIGS layer such that there is no contribution from rear reflectance. The difference between the two curves indicates R_{esc} . Considering that the average difference between R_{tot} and R_{front} for the wavelengths up to 800 nm is only 0.009, the influence of R_{esc} on total reflectance in the corresponding part of the spectrum can be considered as insignificant. Therefore, to simplify the model for faster simulations, we excluded the nanotextures of the back contact without harming the accuracy of the optimization process for $300 < \lambda < 800$ nm. In this wavelength range, from 27.2 mA/cm² of maximum attainable photo-current density from S-Q limit, 7.03 mA/cm² is lost due to reflection and parasitic absorption. The contribution of reflectance to this loss is 2.36 mA/cm² or 33.6%, accounting for almost one third of the optical losses. By suppressing this source of optical losses, more light will be coupled into the solar cell, which can be translated into the improvement of J_{ph} .

4.4 Optical optimization of ARC with reflectance as the cost function

4.4.1 Optimum combination of ARC properties for maximum photogenerated current density

A synthetic double-layer ARC was considered. In this context, *synthetic* means that $\text{Im}\{\varepsilon\} = 0$ and $\text{Re}\{\varepsilon\}$ is wavelength-independent. The electric permittivity and thick-

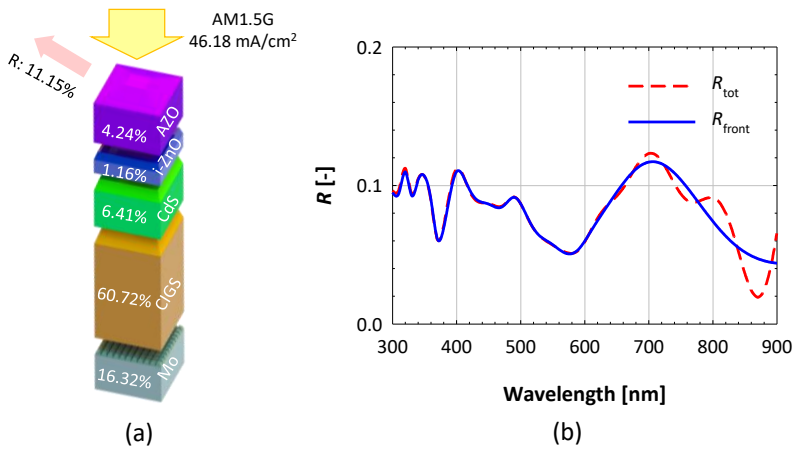


Figure 4.2: a) Breakdown of light absorptance or reflectance for a 750-nm thick CIGS solar cell with respect to the Shockley-Queisser limit in the wavelength range between 300 and 1200 nm. From top to bottom (in nm): AZO (230), i-ZnO (60), CdS (70), CIGS (750) and Mo (150). b) Total reflectance (R_{tot} , dashed red curve) and front reflectance (R_{front} , solid blue curve) spectra of the same solar cell in the wavelength range $300 < \lambda < 900$ nm.

ness of each ARC layer were used as optimization variables (Figure 4.3), resulting in four variables in total. Referring to Figure 4.4(a), in order to protect the AZO layer from moisture, the first ARC layer should be impermeable (i.e. compact) MgF_2 , reducing the variables from four to three, i.e. ϵ_{ARC2} , d_{ARC1} and d_{ARC2} . The optical properties of MgF_2 were taken from [176]. The optimization goal was set to $R(\lambda) < 0.05$ for wavelengths between 300 and 800 nm to achieve a reasonably low reflectance in a wide wavelength range. Sequential nonlinear programming (SNLP) algorithm was selected to find the optimal values of the abovementioned parameters such that the optimization goal is fulfilled. It is instructive to know that SNLP is provided by HFSS, for which the user defines the optimization variables, the cost function, the maximum number of iterations and the variables' allowed ranges. This optimization algorithm has some advantages over other algorithms available in HFSS, such as Quasi-Newton, including less sensitivity to numerical noise and faster practical convergence speed [207]. d_{ARC1} and d_{ARC2} could take values between 50 nm (the minimum practical thickness of porous MgF_2 according to [198]) and 250 nm, while optimal ϵ_{ARC2} could be between 1.08 [198] and 1.9. The upper limit for ϵ_{ARC2} marks the average electric permittivity of compact MgF_2 in the visible spectrum [176].

Figure 4.4(c) shows EQE and $1-R$ spectra of the reference cell (curves with red circles), the cell endowed with EMA-based optimized double-layer ARC (curves with pink crosses) and the cell with realistic dispersive porous MgF_2 as ARC (blue curves). The optimization goal was achieved by $d_{ARC1} = 78.97$ nm and $d_{ARC2} = 79.37$ nm (both approximated to 79 nm) and $\epsilon_{ARC2} = 1.42$. As can be seen from the $1-R$ curves, the proposed ARC structure effectively reduces R to values below 5% in a wide wavelength

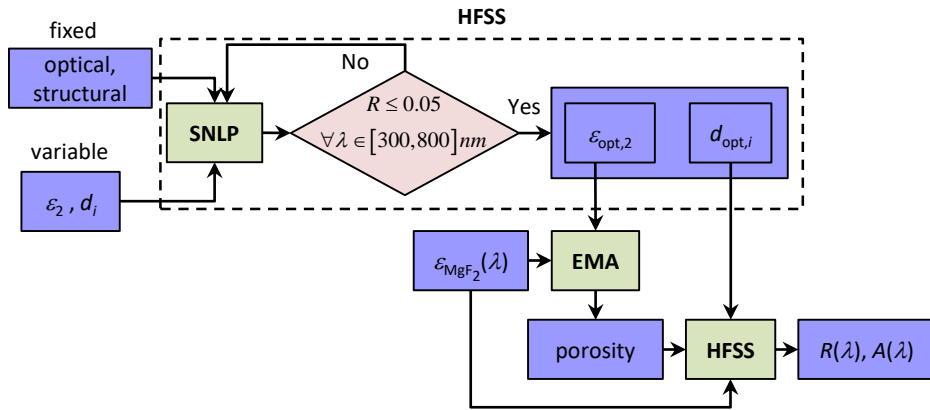


Figure 4.3: Flowchart for optimization of multi-layer ARC using sequential nonlinear programming (SNLP) algorithm: input/output (purple), process (green) and condition (pink). Subscript $i = 1, 2$. is the number of ARC layers. After the optimal electric permittivity and thicknesses are found, the EMA theory provides the porosity value, which translates into the equivalent refractive index used to model the porous top layer of MgF_2 .

range from 300 nm to 930 nm. Reflectance values below 1% can be observed from 510 nm to 680 nm and at 900 nm. This results in a wideband improvement of the *EQE* spectrum. The abovementioned absorptance spectra are compared to the theoretical Green absorption limit [94] for a 750-nm thick CIGS slab. The presence of natural features on the front and back side of CIGS layer complicates the calculation of the equivalent thickness for Green limit computations. Therefore, the corresponding limit for a CIGS slab of 750 ± 250 nm thickness is shown in grey in Figure 4.4(c). These absorptance spectra indicate that i) the reflectance is a major contributor to the optical losses, ii) the reflectance can be quenched in a wide part of the spectrum of interest and iii) the reduction of parasitic absorption is required for further improvement of CIGS absorptance.

As mentioned above, the optimal value of $\epsilon_{\text{ARC}2}$ is in fact the effective electric permittivity of a porous layer of MgF_2 with the same thickness, in which, according to Equation 4.1, the volume fraction of pores is 48%. This porosity was modelled by randomly placing in ARC2 spheroids of air having < 15 -nm long radii and using realistic optical constants of MgF_2 both for ARC1 and ARC2 (Figure 4.4(b)) [176]. The nearly perfect agreement between the *EQE* and $1-R$ spectra of EMA-based model and porous ARC model (Figure 4.4(c)) approves the reliability of our optimization based on the EMA approach. Also, in computational terms, referring to the EMA-based model in Figure 4.4(a) and the porous model in Figure 4.4(b) with *EQE* and $1-R$ spectra reported in Figure 4.4(c), the former occupied 30 times less RAM and was 96 times faster than the latter.

Next, the natural morphology of Mo surface was included in the simulation in order to examine the accuracy of the model and calculate the more realistic value of J_{ph} .

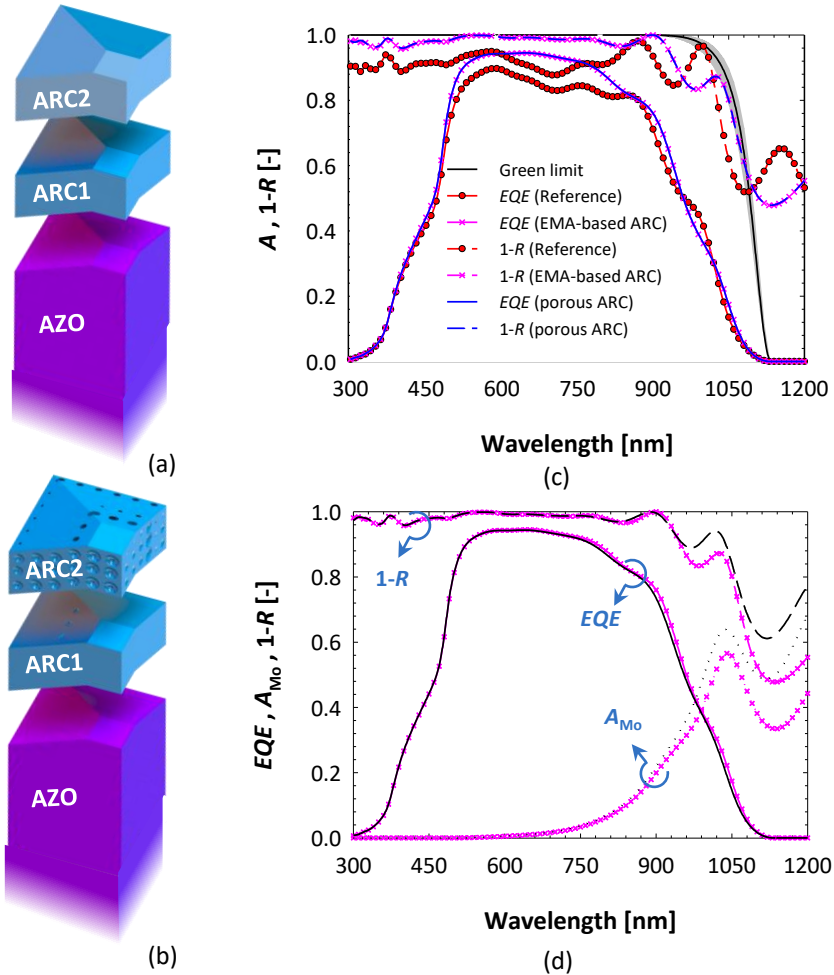


Figure 4.4: A quarter of the unit cell's front side covered with a) a compact double-layer ARC using EMA technique; and b) the same but with MgF_2 replacing the equivalent material of ARC1 and ARC2 and including pores in ARC2; c) EQE and $1-R$ spectra of i) reference cell (curves with red circles), ii) the cell with optimized ARC using EMA approach (curves with pink crosses) and iii) the cell endowed with double-layer porous MgF_2 as ARC (blue curves) against the Green absorption limit ([94]) for a 750-nm thick CIGS layer (black curve; the grey area shows Green limit for the thickness difference of ± 250 nm); and d) EQE , $1-R$ and Mo absorptance spectra of the solar cell endowed with optimized double-layer ARC for flat (curves with pink crosses) and rough (black curves) CIGS / Mo interface.

This was fulfilled by adding truncated pyramids with the bottom and top base area of $30 \times 30 \text{ nm}^2$ and $20 \times 20 \text{ nm}^2$, respectively, and the height of 20 nm [156]. Figure 4.4(d) shows modelled EQE and $1-R$ spectra of the solar cell modified with optimized double-layer ARC with and without Mo surface morphology. As expected, the presence of these nanotextures increases the light absorption inside Mo at long wavelengths (**Chapter 3**) [156] and, therefore, reduces R_{esc} and EQE in the corresponding part of the spectrum. The impact on the performance at wavelengths up to 800 nm on the other hand, is negligible.

At this point, it is possible to calculate the gain in J_{ph} as a result of the designed double-layer ARC. As expected, and the optimization aimed at, the total current density lost due to reflectance ($J_{\text{Loss-R}}$) encountered an 84.7% reduction from 2.36 to 0.36 mA/cm^2 for $300 < \lambda < 800 \text{ nm}$ (reclaiming 2 mA/cm^2 of the reflectance loss). As a result, J_{ph} increased from 20.17 mA/cm^2 to 21.81 mA/cm^2 , accounting for a relative gain of 8.13%. Besides that, a small part of the additional light coupled into the solar cell (0.36 mA/cm^2) is parasitically absorbed in layers other than CIGS. Taking the whole wavelength range of interest (300 to 1200 nm) into account, the enhancement of J_{ph} was calculated to be 1.9 mA/cm^2 , i.e. from 28.04 mA/cm^2 to 29.95 mA/cm^2 (+6.77%).

The same optimization approach was used for the design of a three-layer ARC that is not shown here for brevity. In that case, the optimization goal was accomplished by a more complicated structure with five optimization variables that has no practical advantage over the simpler double-layer ARC scheme. However, it was useful for assessing the potential of SNLP technique in handling cumbersome optimization calculations. Also, the validity of EMA assumption for the three-layer ARC was checked and confirmed.

4.4.2 Optimum combination of ARC properties for maximum photo-generated current density

Although decreasing the front reflectance improves J_{ph} , the optimal ARC structure for maximum J_{ph} might not be the same as the one when minimum reflectance is chosen as the cost function [133]. This can happen when the additional light coupled into the solar cell is lost due to parasitic absorption in front layers such as TCO and buffer layer [133]. For this reason, the properties of each ARC layer were varied independently and both J_{ph} and $J_{\text{Loss-R}}$ were calculated as functions of those parameters for wavelengths between 300 and 800 nm.

Figure 4.5 shows J_{ph} and $J_{\text{Loss-R}}$ as functions of d_{ARC1} , while ϵ_{ARC2} and d_{ARC2} were kept constant at the optimal values of 79 nm and 1.42, respectively. d_{ARC1} was varied from 50 to 150 nm in steps of 10 nm. Due to the limited number of simulations, nanotextures at Mo surface were considered at the expense of slower simulations. It can be concluded from this figure that minimum reflectance loss and maximum absorptance in CIGS occur at the same thickness of ARC1, or more generally, J_{ph} and $J_{\text{Loss-R}}$ follow opposite trends. Additionally, it can be noticed from Figure 4.5 that J_{ph} is not sensitive to small deviations from the optimal thickness of ARC. For example, a deviation of 10% from optimal d_{ARC1} results in less than 0.15% change in J_{ph} , which shows the flexibility of manufacturing with respect to thickness accuracy.

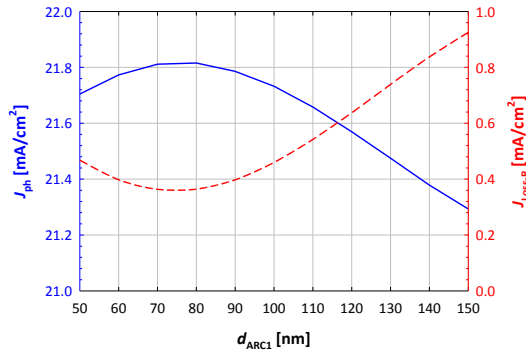


Figure 4.5: Implied photo-current density (J_{ph}) and total current density lost due to reflectance ($J_{\text{Loss-R}}$) as function of the thickness of ARC1, while the properties of ARC2 are kept at the optimal values ($d_{\text{ARC2}} = 79$ nm and $\varepsilon_{\text{ARC2}} = 1.42$). The wavelength range is between 300 nm and 800 nm.

The same observation (i.e. J_{ph} and $J_{\text{Loss-R}}$ having opposite trends) is made when the properties of ARC2 are varied independently from d_{ARC1} (Figure 4.6). In this case, $\varepsilon_{\text{ARC2}}$ took values between 1.05 and 1.9, while d_{ARC2} was spanned between 50 nm and 150 nm. It should be noted that in Figure 4.6, the values of current density, corresponding to the neighbouring colours, have a small difference of only 0.05 mA/cm². Considering this, it can be noticed that there is a wide range of optimal combinations of $\varepsilon_{\text{ARC2}}$ and d_{ARC2} that lead to maximum J_{ph} and minimum $J_{\text{Loss-R}}$. Also, from practical point of view, the design of ARC is not extremely sensitive to the discrepancy of the thickness and porosity from the optimal values.

4.4.3 Single- or double-layer ARC?

As mentioned above, a single-layer of 100-nm thick MgF₂ is the conventional ARC for lab-scale CIGS solar cells. In Figure 4.7 the optical performance of the optimized double-layer ARC (with EMA approach) is compared to the reference cell and the standard single-layer ARC. In all three models, the nanotextures at Mo / CIGS interface were taken into account. In case of the single-layer ARC, J_{ph} increases by 6.35% from 28.04 mA/cm² to 29.82 mA/cm². The proposed porous ARC shows almost the same impact on the optical performance with a slightly better *EQE* only in the wavelength range between 700 and 860 nm, translating into a small improvement of 0.1 mA/cm² in J_{ph} with respect to single-layer ARC. Although the porous ARC reduces the reflectance in ultra-violet part of the spectrum more effectively than the single-layer one, the extra light coupled into the solar cell is parasitically absorbed by the top layers instead of the cell absorber. The advantage of the proposed ARC over the conventional one is, however, in the better angular response (see Figure 4.7(b)). At the incidence angle of 80°, the solar cell modified with the double-layer ARC produces 2.64 mA/cm² more photo-current density than its conventional counterpart. This proves that the new ARC structure is more beneficial when less dependency on the incidence angle is

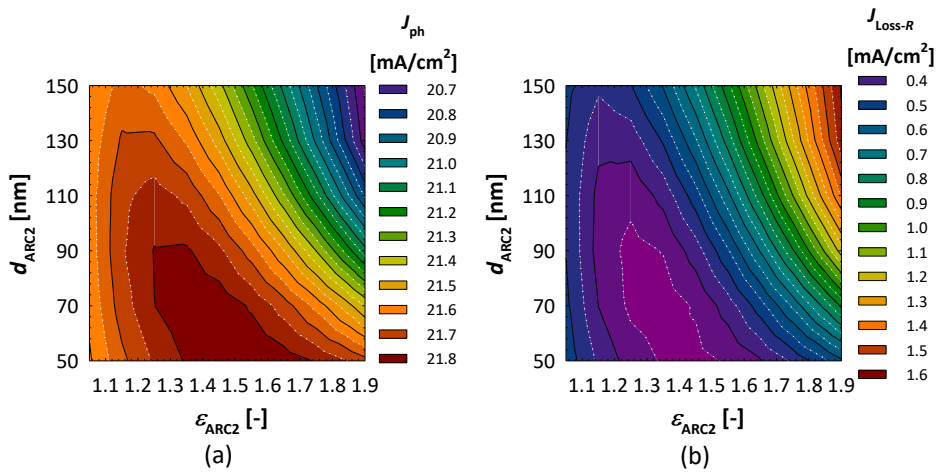


Figure 4.6: a) Implied photo-current density and b) total reflectance integrated as current density versus thickness and electric permittivity of ARC2, while the thickness of ARC1 is kept at the optimal value ($d_{ARC1} = 79$ nm). The wavelength range is between 300 nm and 800 nm.

required, e.g. when the sunlight direction varies due to diurnal and seasonal changes. This effect can also be seen in other nanotechnologies. Isabella et al. employed periodic high aspect ratio features in nano-crystalline silicon solar cells and achieved optimal light in-coupling into the absorber [71]. While high resilience against AOI is ensured in their design, possible deterioration of the electrical performance and fabrication complexity could hinder the significant optical improvement they achieved. The same result (low dependency on AOI) was achieved by Savin et al. for black silicon-based solar cell technology, in which sub-wavelength nano-cones are produced via etching processes [208]. Compared to these designs, our proposed porous-on-compact ARC is simpler and involves no etching of the absorber layer. Note that any light management technique which includes removal of the CIGS layer hinders our goal of cost-effectiveness by reducing absorber material consumption.

The fast, simplified and accurate modelling using EMA is not only useful in the special case introduced in this paper, but also in other PV technologies, light emitting diodes, etc. This approach can be proven to be useful in simulating the more industrial case of encapsulated CIGS solar cells.

4.5 Improvement of optical performance in the whole incident spectrum

Although the proposed double-layer ARC improves the light in-coupling, a considerable part of the low-energy photons is absorbed (therefore lost) in the Mo back contact as a result of the excitation of surface-bound plasmons [156]. In previous chapter,

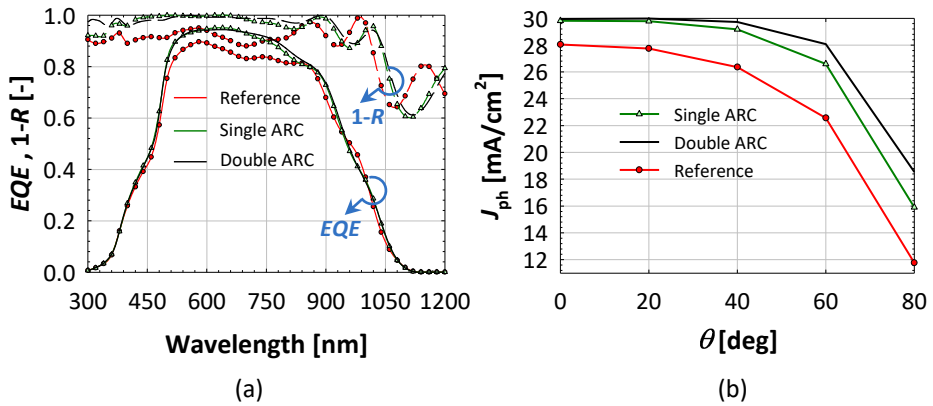


Figure 4.7: a) EQE and $1-R$ spectra of the reference 750-nm-thick CIGS solar cell (curves with red circles) and the same but with single-(curves with green triangles) and double-layer (black curves) MgF_2 ARC; and b) J_{ph} vs angle of incidence for the same solar cells.

a double-layer spacer / passivator consisting of MgF_2 and Al_2O_3 (100 nm and 10 nm, respectively) was suggested and optimized to quench this optical loss in the long wavelength part of the spectrum. The charge carrier collection was facilitated via optically-optimized point contacts with circular cross sections and 25% area coverage [156]. A combination of both double-layer ARC and point contact scheme can therefore, provide J_{ph} improvement over the whole wavelength spectrum of interest. This idea was implemented in our models for the 750-nm thick CIGS solar cell and the resulting J_{ph} was compared to those of the reference cell and a more standard 1600-nm thick CIGS solar cell. As can be seen in Figure 4.8, with an 11.3% increase in J_{ph} compared to the reference 750-nm thick cell, the cell with joined front and rear light management scheme successfully outperforms the cell with an absorber thickness of more than twice as thick. This highlights the crucial role of proper light management techniques in compensating low-thickness-borne absorptance losses or even surpassing the optical performance of standard CIGS solar cells.

4.6 Conclusions and outlook

We successfully optimized a porous-on-compact double-layer antireflection coating (ARC) based on MgF_2 for a CIGS solar cell with an absorber thickness of 750 nm. We calibrated our FEM-based 3-D Maxwell's equation solver with measured EQE and $1-R$ spectra. We employed effective medium approximation (EMA) theory of Bruggeman for modelling the top porous ARC layer. Choosing $R < 5\%$ as the cost function for $300 < \lambda < 800$ nm and by using sequential nonlinear programming algorithm, we optimized the thickness of two ARC layers and the equivalent electric permittivity of the top layer. The optimization algorithm led to a thickness of 79 nm for both ARC layers and to an effective permittivity of 1.42 for the top ARC layer. This (according

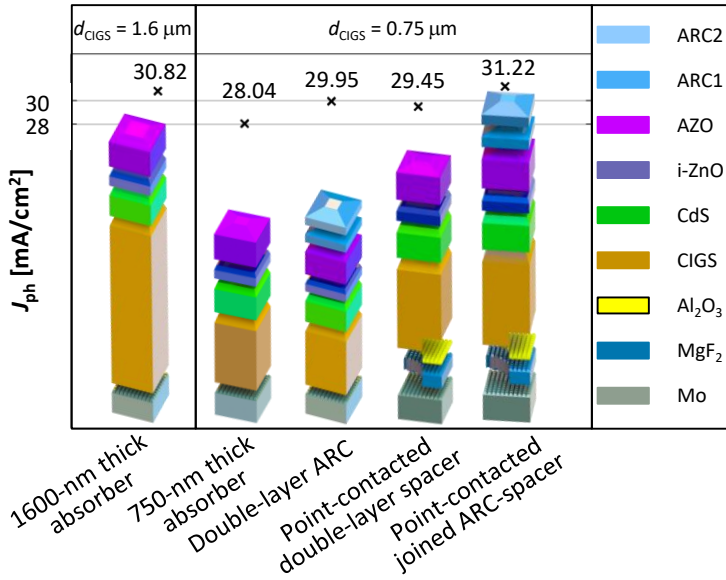


Figure 4.8: From left to right: Photo-current density and schematic of i) a 1600-nm thick CIGS solar cell, ii) a 750-nm thick CIGS solar cell, the same but with iii) double-layer ARC, iv) double-layer spacer with point contact scheme [156] and v) joined double-layer ARC at the front side and double-layer spacer at the back side of the solar cell. In the last two schematics, only one quarter of the modelled unit cell is shown.

to the EMA theory) is equivalent to a porous MgF_2 layer with porosity volume ratio of 48%. The simulation results show a 6.77% increase in implied photocurrent density (J_{ph}) from 28.04 mA/cm² to 29.95 mA/cm² for wavelengths between 300 and 1200 nm.

An independent variation of the properties of each ARC layer for achieving maximum J_{ph} indicated that i) J_{ph} and $J_{\text{Loss-R}}$ (current density lost due to reflectance) follow opposite trends, meaning that maximum J_{ph} and minimum $J_{\text{Loss-R}}$ occur for the same ARC properties, and ii) practically, the performance of our designed ARC is mainly unchanged despite deviations in thicknesses and porosity of the MgF_2 layers that can occur at experimental level. This study also elucidates the appropriateness of using the EMA approach in alleviating the computational burden (by a factor of 30) of inherently complex models endowed with sub-wavelength features.

Next, we compared the proposed double-layer ARC to a standard 100-nm thick MgF_2 ARC for perpendicular illumination and observed no significant difference. However, the double-layer porous ARC outperforms the standard one for oblique light illumination. This indicates the advantage of the new ARC design over the more standard one during diurnal and seasonal change of sunlight direction. Additionally, when comparing our proposed ARC structure to other light in-coupling approaches which are based

on high aspect ratio nanostructures in the absorber layer, our design appears simpler and more cost-effective, thanks to no absorber removal by etching processes.

Finally, we successfully achieved an efficient light management for the whole spectrum by combining the double-layer ARC with a point-contacted double-layer dielectric spacer placed between the back contact and CIGS. The dielectric spacer which consists of Al_2O_3 and MgF_2 , provides both electrical passivation and better internal reflection, improving the long wavelength performance of the solar cell. The result was an 11.3% improvement in J_{ph} from 28.04 mA/cm^2 to 31.22 mA/cm^2 . A comparison between J_{ph} production of the modified sub-micron CIGS solar cell with that of a cell with a 1600-nm thick CIGS layer shows that, with proper light management techniques, an ultra-thin CIGS solar cell can outperform its thicker counterpart. This will eventually reduce the material consumption in CIGS PV technology, helping the manufacturers to increase further its PV market share.

5

IBC CIGS solar cells, Part I: optical study

This chapter was published in *Optics Express** [209]

Abstract

A novel back-contacted solar cell based on submicron copper indium gallium (di)selenide (CIGS) absorber is proposed and optically investigated. Two back-contacted configurations are suggested and optimized for maximum current production. The results are compared with a reference front/back-contacted CIGS solar cell with 750-nm thick absorber. Current density production of 38.84 mA/cm^2 is predicted according to our simulations for a realistic front side texturing. This shows more than 38% improvement in optical performance compared to the reference cell and only 7.7% deviation from the theoretical Green absorption benchmark.

*N. Rezaei, O. Isabella, P. Procel, Z. Vroon, and M. Zeman, "Optical study of back-contacted CIGS solar cells," *Optics Express*, vol. 27, no. 8, A269, 2019. doi: 10.1364/oe.27.00a269.

5.1 Introduction

Even though the performance of ultra-thin CIGS solar cells can be improved by the light management methods described in previous chapters, there are still more challenges to overcome in this topic. Firstly, as shown in **Chapter 4**, the parasitic absorption in the front layers of a submicron CIGS solar cell contributes to more than 10% of optical losses [181]. Secondly, for CIGS devices deposited on thin flexible foils [210], the metallic grid at the front side of a front/back-contacted (FBC) solar cell, blocks a significant part of the incident light from entering the cell (optical shading) [211].

In an interdigitated back-contacted (IBC) solar cell, both electron (e) and hole (h) contacts (e-contact and h-contact) are alternatively located at the rear side of the absorber, as demonstrated in a number of high efficiency c-Si IBC solar cells [212]–[220]. This way, the optical shading and parasitic absorption are eliminated and the high energy photons can reach the absorber bulk and contribute to charge carrier generation. In this work, we introduce an IBC CIGS solar cell with a submicron absorber thickness. The collection feasibility of both charge carriers is studied by band diagram analysis in **Chapter 6**. Two light in-coupling configurations, namely, high aspect ratio front textures (see Figure 5.1) and double-layer antireflection coating (ARC, see Figure 5.1) will be investigated by means of rigorous three-dimensional (3-D) optical simulations. In both configurations, the e-contact dimensions are optimized for maximum current generation. This study provides guidelines to CIGS research community about IBC CIGS solar cells, which to our knowledge has not been studied so far.

5.2 Modelling platform

The band diagram of the structure (modelled by Sentaurus TCAD) will be studied in detail in the following chapter. The optical performance of the solar cell was modelled using Ansys HFSS. The optical constants of CIGS [156], [168], Mo [72], [156], ZnO:Ga (GZO) [221], MgF₂ [176] and Al₂O₃ [175] are used as modelling inputs. Master and slave boundary conditions are deployed to model the periodic structure. More details about the modelling scheme can be found in Chapters 3 and 4. The current density generated in the absorber ($J_{ph-CIGS}$) or dissipated in the i -th layer of the structure (J_{ph-i}) was calculated according to Equation 3.3. Here, $J_{ph-CIGS}$ represents the short circuit current density (J_{SC}) of the solar cell, assuming full charge carrier collection. It should be noted that both transverse electric (TE) and transverse magnetic (TM) polarizations are considered in the simulations and each absorptance spectrum is the average between the related spectra obtained from the two polarizations.

Green absorption limit [94] is used as a benchmark with which the optical performance is compared. This parameter describes the maximum absorption spectrum of a randomly textured slab of a material (here, CIGS) for which i) front reflectance is completely quenched, ii) light propagating in the slab is completely randomized, and iii) rear internal reflectance caused by a lossless metallic reflector is maximized. The Green limit is calculated as in Equation 2.10.

The proposed solar cell structures are compared to a reference FBC cell with a

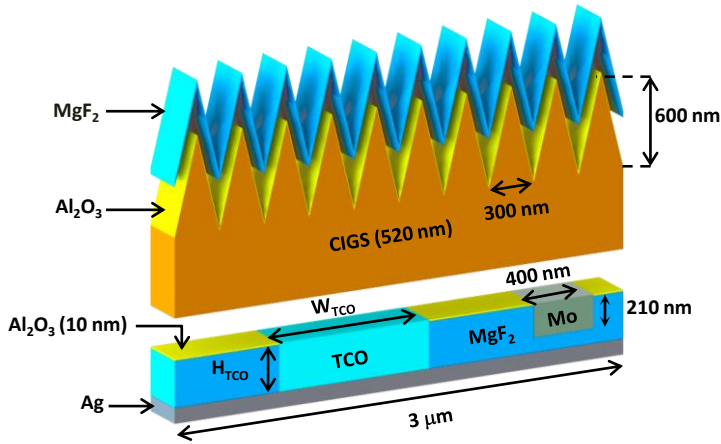


Figure 5.1: Visual rendering of the back-contacted CIGS solar cell with high aspect ratio features at the front. W_{TCO} and H_{TCO} indicate, respectively, width and height of the TCO.

CIGS thickness of 750 nm with and without a 100-nm thick MgF_2 ARC layer. From the light-facing window layers to the rear contact, the cell structure comprises the following layers: ZnO:Al / $i\text{-ZnO}$ / CdS / CIGS / Mo. More details about the optical modelling of the reference cell can be found in **Chapters 3 and 4**.

It is known that the number of the absorbed photons is directly related to the absorber volume [71], [222]. Therefore, the amount of absorber material in all of the configurations in this work is kept constant. Additionally, in order to account for the whole optically-active part of the absorber, the optical thickness is defined as the thickness from the top of the textures to the bottom of the absorber [71], [223]. It should be noted that the optical thickness is different from the equivalent thickness (the ratio between the unit cell volume and its bottom area). Hence, the deviation of J_{ph} from Green limit for a CIGS slab with the same optical thickness can be calculated as [71]:

$$\Delta_{\text{Green}} = \frac{J_{\text{ph-CIGS}} - J_{\text{Green}}}{J_{\text{Green}}} \% \quad (5.1)$$

where J_{Green} is the Green absorption limit integrated according to Equation 2.10.

5.3 Results and discussion

5.3.1 Design considerations

A detailed explanation on the design considerations for this IBC structure, the choice of materials and the band diagram of the contacts' cross-sections will be provided in Chapter 6. Therefore, in this chapter, we only focus on the optical potential of the novel IBC structure.

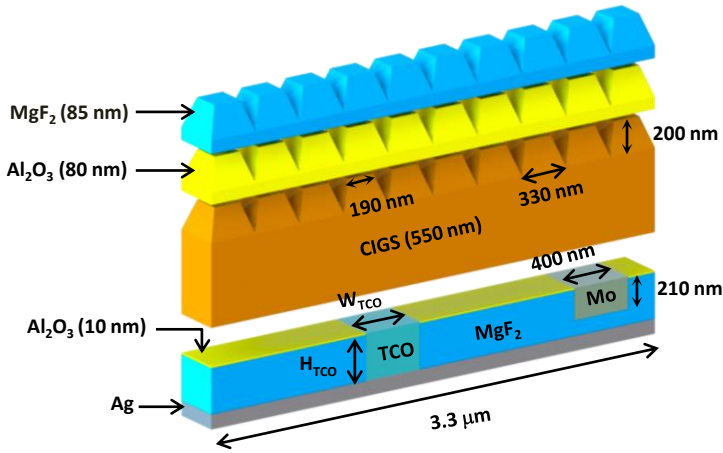


Figure 5.2: Visual rendering of the back-contacted solar cell with natural CIGS morphology and optimized ARC. W_{TCO} and H_{TCO} indicate, respectively, width and height of the TCO.

5.3.2 IBC solar cells with antireflective front textures

Figure 5.1 shows a visual rendering of the IBC CIGS solar cell. The presence of steep grooves with height to width ratio of 2 at the front side promotes light in-coupling and, hence, minimal reflection losses. A thin layer of Al_2O_3 improves the chemical and electrical passivation of the front surface.

The height and width of GZO (H_{TCO} and W_{TCO} , respectively) were optimized for the best current density production. W_{TCO} was varied between 400 and 1000 nm in steps of 100 nm. H_{TCO} took values between 240 (30 nm thicker than Mo to ensure a gap between Mo and the silver reflector) and 330 nm in steps of 30 nm. Figure 5.3(a) shows $J_{\text{ph-CIGS}}$ as a function of these parameters. Maximal $J_{\text{ph-CIGS}}$ can be obtained for $W_{\text{TCO}} > 800$ nm and $H_{\text{TCO}} > 290$ nm. Even though the optical performance might be better for larger W_{TCO} , we limited its range to values below the diffusion length to ensure good electrical performance as well. As a result, we selected 1000 nm and 320 nm as the optimal values for W_{TCO} and H_{TCO} , respectively. The absorptance and reflectance ($1-R$) spectra of the resulting configuration compared to the absorptance spectrum of the reference FBC solar cell is presented in Figure 5.3(b). Owing to the elimination of front layers' parasitic absorption and the low reflectance, almost all of the incident high energy photons are absorbed by the CIGS layer. This leads to an improvement of J_{ph} from 28.04 mA/cm² for the reference cell to 39.69 mA/cm² for the IBC cell with optimal TCO (41.55% improvement). Using Equation 5.1 to calculate Δ_{Green} for an optical thickness of 1120 nm (the peak-to-valley height of the textures plus the bulk thickness) shows that the IBC solar cell deviates from the benchmark by only 6.65%. On the other hand, since a significant number of lab-scale CIGS solar cells are combined with a nearly 100-nm thick MgF_2 ARC layer, it is instructive to compare the proposed IBC solar cell with an FBC cell including ARC. The latter was presented in **Section 4.4.3** with $J_{\text{ph}} = 29.82$ mA/cm². The optimized IBC solar cell

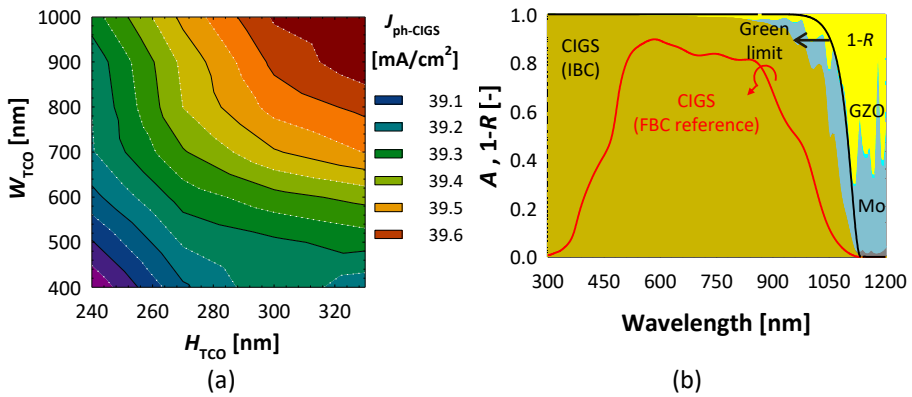


Figure 5.3: a) Implied photocurrent density in CIGS layer ($J_{ph-CIGS}$) as a function of width and height of TCO. b) absorbance and $1-R$ spectra of the IBC solar cell when $W_{TCO} = 1000$ nm and $H_{TCO} = 320$ nm.

shows a non-marginal improvement of 33.1%.

Even though the development of high aspect ratio textures on a CIGS layer is proven to be possible [224], this approach would need the partial removal of the absorber by ion bombardment [225] or wet etching [226]. This is in contrast with the photovoltaic (PV) market goal of increasing industrial throughput of CIGS PV technology by reducing material consumption [75], [86], [160]. In the following section, the development of the back-contacted solar cell with natural CIGS morphology is studied.

5.3.3 IBC solar cell with as-grown absorber morphology

According to our atomic force microscopy measurements for CIGS samples made at TNO [38], the lateral correlation length of the as-grown grains is about 330 nm [156], [181]. This was included in the structure of a back-contacted CIGS solar cell model without antireflective textures (see Figure 5.2). The natural roughness was modelled by introducing periodic truncated pyramids on the absorber bulk. Even though this is a simplification of the realistic device, the calibrated external quantum efficiency (EQE) and reflectance spectra sufficiently match the measured counterparts, confirming the validity of the assumption (see Chapter 4) [156]. Note that the absorber volume in Figures 5.1 and 5.2 are equal for fair comparison. In the absence of steep features at the front side for high light in-coupling, an alternative approach was employed. The thickness of passivating Al_2O_3 and antireflective MgF_2 layers in a reference solar cell were optimized for minimal reflection. The optimization algorithm is discussed in more details in Chapter 4 [181]. The resulting thicknesses for Al_2O_3 and MgF_2 are 80 and 85 nm, respectively.

Performing the same TCO optimization procedure as in the previous session leads to the results shown in Figure 5.4. $J_{ph-CIGS}$ values higher than 38.8 mA/cm² can be achieved for $W_{TCO} > 950$ nm and $H_{TCO} > 300$ nm. The optimal combination of these parameters ($W_{TCO} = 1000$ nm and $H_{TCO} = 320$ nm) resulted in the absorbance

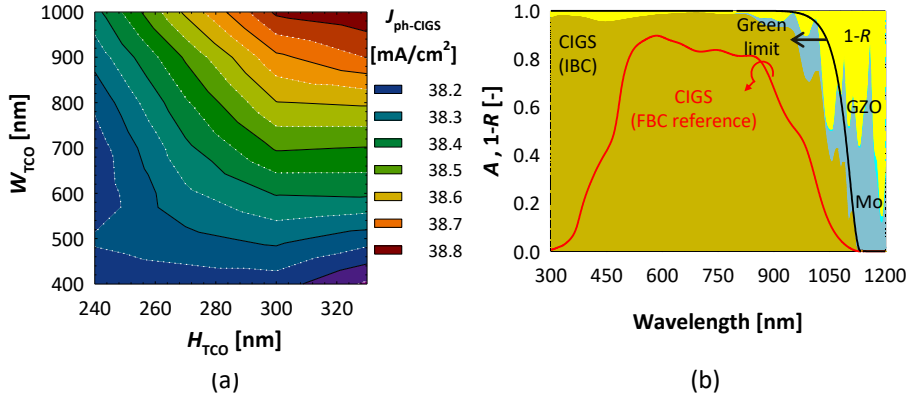


Figure 5.4: a) Implied photocurrent density (J_{ph}) as a function of width and height of TCO. b) absorbance and $1-R$ spectra of the IBC solar cell when $W_{TCO} = 1000$ nm and $H_{TCO} = 320$ nm.

and $1-R$ spectra plotted in Figure 5.4(b). As it can be seen in such a figure, a small drop in absorbance occurs at short wavelength region due to higher reflection from the front side of the cell. In total, $J_{ph-CIGS} = 38.84$ mA/cm² is expected from the optimized cell, showing less than 0.9 mA/cm² decrease in $J_{ph-CIGS}$ compared to the previous design. Considering cheaper and easier fabrication process of this approach, the drop in $J_{ph-CIGS}$ appears negligible. In this case, where the optical thickness is 750 nm, $J_{Green} = 42.11$ mA/cm², and therefore, according to Equation 5.1, Δ_{Green} will be 7.7%. This value is still very small compared to the case of the reference cell for which $\Delta_{Green} = 33.4\%$. The $J_{ph-CIGS}$ obtained in this work is comparable to the J_{SC} of world record efficiency CIGS solar cell [14], [27], in which parasitic absorption is still not addressed and the absorber thickness is considerably thicker than that of our design. In comparison to the FBC solar cell endowed with a 100-nm thick MgF₂ ARC, the IBC cell with as-grown CIGS morphology offers 30.2% improvement in J_{ph} .

We analyzed the optical performance of the IBC cell in more details for wavelengths longer than 900 nm. Figure 5.5(a) shows a close-up of Figure 5.4(b) overlaid by TM and TE components of the absorbance spectrum. As can be seen in this figure, the wavelength and amplitude of the average CIGS absorbance in low-energy part of the spectrum is mainly dominated by TM polarization. Figure 5.5(b-d) present the electric field magnitude ($|\vec{E}|$) at wavelengths corresponding to three local maxima in the TM-polarized absorbance spectrum.

These maxima are located at wavelengths 1020, 1070 and 1110 nm, indicated with red arrows in Figure 5.5(a). It should be noted that each local maximum in CIGS absorbance is correlated with a local minimum in total reflectance. This means that as more photons are trapped in the solar cell bulk, less photons escape from the cell. At 1020 nm (Figure 5.5(b)), the Fabry-Perot modes are the main components of the electric field, causing the light to mainly propagate in perpendicular direction with respect to the plane of incidence [227]. As the wavelength increases, the diffraction

modes that are triggered by the rear dielectric / metal arrangement (GZO / MgF_2 / Mo / MgF_2) and are coupled with waveguide modes inside the absorber bulk, outweigh the Fabry-Perót modes. This phenomenon is clearly visible in Figure 5.5(c) and (d), where waveguide modes are the dominant components of the electric field.

Even though the CIGS absorptance might have a slightly different shape in the two IBC designs in the long-wavelength regime (see Figure 5.3(b) and Figure 5.4(b)), the total generated J_{ph} in that part is not very different. For instance, for wavelengths between 900 and 1200 nm, the obtained photo-current densities from the first and the second IBC structures are 7.09 and 6.62 mA/cm^2 , respectively. This is due to the limited capability of the absorber in absorbing close-to-bandgap photons. Therefore, the higher intensity of the electric field in Figure 5.5(d) does not necessarily mean that the absorber will be capable of absorbing all of the trapped photons.

It should be noted that we also considered ITO as e-contact material in our models. In that case, due to the lower transparency of ITO material [221], less $J_{ph-CIGS}$ can be expected by the optimized structure. More importantly, the presence of indium in ITO contradicts our goal of decreasing indium usage, and, thus, fabricating cost-effective CIGS solar cells. Hence, we excluded ITO from our proposed IBC structure.

5.4 conclusions

CIGS with a low bandgap and high absorption coefficient, is a great candidate for thin-film solar cell applications. High parasitic absorption in front/back-contacted solar cell architectures hinders the full utilization of CIGS's optical potential. In this work, a back-contacted CIGS solar cell was proposed. An IBC solar cell with antireflective textures and optimized TCO dimensions showed a potential 41.55% improvement in implied photocurrent density ($J_{ph-CIGS}$) compared to a front/back-contacted reference cell without ARC and a 33.1% improvement with respect to an FBC solar cell including a 100-nm thick MgF_2 ARC layer. A simpler structure with as-grown CIGS morphology and optimized flat antireflection coating revealed a maximum $J_{ph-CIGS}$ value of 38.84 mA/cm^2 . This value deviates from the theoretical Green limit by only 7.7% and is comparable to the short circuit current density of the world record CIGS solar cell, albeit with significantly thicker absorber. Even though the fabrication of our proposed IBC structure in the current design might be complicated, eventually including a number of etching and lithography steps, we believe that this is an important step towards the development of high efficiency and cost-effective CIGS solar cells. More theoretical and experimental studies are needed to reach a balance between the cost and efficiency of such devices.

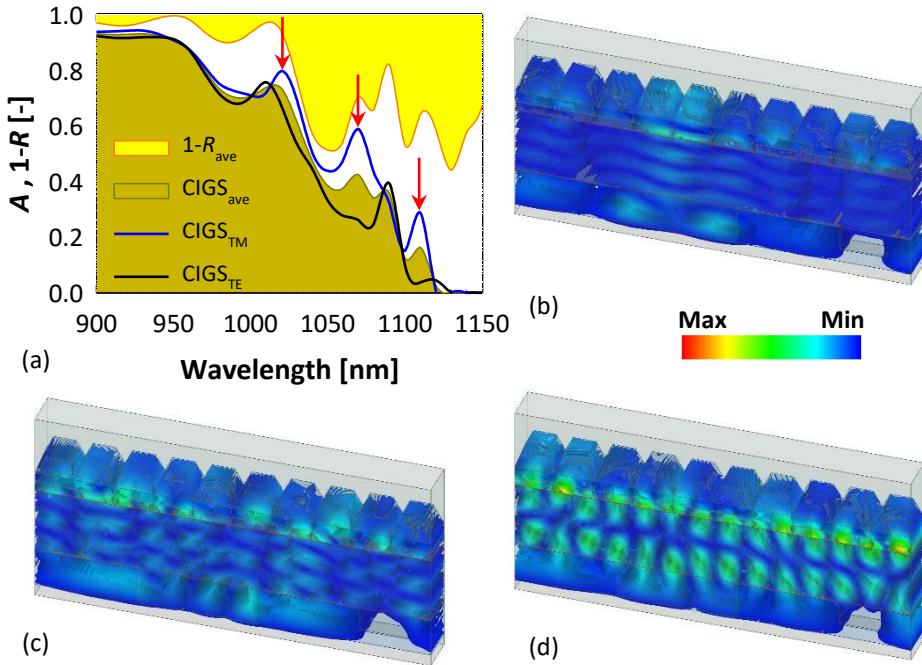


Figure 5.5: a) CIGS absorption for TM (blue line), TE (black line) and average of TM and TE (brown area) polarizations and average $1-R$ (yellow area) spectra. The graphs correspond to the optimized IBC solar cell with as-grown CIGS grains. b) – d) Electric field magnitude at wavelength b) 1020 nm, c) 1070 nm and d) 1110 nm for TM polarization corresponding to local maxima in CIGS absorption, also indicated with red arrows in a).

6

IBC CIGS solar cells, Part II: opto-electrical study

This chapter was published in *Progress in Photovoltaics**

Abstract

An interdigitated back-contacted (IBC) configuration is proposed for sub-micron copper indium gallium (di)selenide (CIGS). In a modelling platform, the structure was opto-electrically optimized for maximum efficiency. The results are compared to a reference front/back-contacted (FBC) solar cell with similar absorber thickness and exhibiting 11.9% efficiency. The electrical passivation at the front side is accomplished by an Al_2O_3 layer, which is endowed with negative fixed charges. The results indicate that with an optimal geometry and engineered bandgap grading the efficiency of the new IBC structure can reach 17%. Additionally, with a reasonably low defect density in the absorber layer, efficiencies as high as 19.7% and open-circuit voltage comparable to that of the record solar cell are possible with the IBC structure.

*N. Rezaei, P. Procel, M. Simor, Z. Vroon, M. Zeman and O. Isabella, "Interdigitated back-contacted structure: a different approach towards high efficiency ultra-thin CIGS solar cells," *Progress in Photovoltaics*, 1-10, 2020 doi:10.1002/pip.3296

6.1 Introduction

High absorption coefficient and tuneable bandgap (between 1 and 1.7 eV) make copper indium gallium (di)selenide (CIGS) an appropriate absorber material for highly efficient thin-film solar cell applications [23], [35], [158]. Yet, with a world record efficiency of 23.35% [14], [27], CIGS solar cells are still far from the Shockley-Queisser (SQ) theoretical efficiency limit [89], [90]. This gap is even wider for sub-micron CIGS solar cells, which for various reasons are studied by different research groups [31], [33], [83]. In addition to optical losses, sub-micron CIGS solar cells suffer from other performance deteriorations, which generally lead to less than optimal efficiencies [228]. In this respect, different strategies such as light management [26], [122], [181], back contact passivation [83], [86], [229] and alternative front layers [27], [230] have been employed to increase the performance of both thick ($> 1 \mu\text{m}$) and ultra-thin CIGS solar cells. However, in the front/back-contacted (FBC) structure, there are inevitable optical losses due to the parasitic absorption of the top layers, accounting for more than 10% loss in photocurrent density (J_{ph}) [76], [162], [181]. Also, in case of flexible CIGS solar cells, the metallic grid causes an additional optical shading [66], reducing even more the optical performance of these solar cells.

An interdigitated back-contacted (IBC) solar cell structure can be used to avoid the abovementioned optical losses. In IBC structure, the electron- and hole-contact (e-contact and h-contact, respectively) are both located at the rear side of the absorber material in a periodic design [150], [208], [209], [213], [215]–[220], [231]–[233]. In previous chapter, we investigated the optical performance potential of a novel IBC CIGS solar cell with and without textured antireflection coating (ARC). In this chapter, we employ opto-electrical simulations in TCAD Sentaurus environment to further study and optimize an IBC CIGS solar cell. First, we calibrate the model by matching the current density versus voltage (J - V) curves of simulated FBC CIGS solar cells with experimentally measured curves. Then, after explaining the IBC design strategy, we optimize geometrical and material properties in a step-by-step approach, keeping both efficiency and practicability in mind.

6.2 Modelling approach

We used a two-dimensional (2-D) simulation approach for both the FBC and IBC solar cell structures in TCAD Sentaurus environment. This simulation tool solves drift-diffusion equations by considering the thickness of the layers, trap distributions, doping, band structures and layers' optical properties [234]. We modelled opto-electrically the layered structures and selected the transfer matrix method (TMM) for the optical modelling. Using the reference FBC cells fabricated at Solliance, we performed atomic force microscopy (AFM) to measure the root mean square (RMS) roughness in two cases: i) the ZnO:Al (AZO) surface of the full solar cells and ii) the bare CIGS surface after removing the front contact layers. The average RMS roughness of several samples was between 30 and 45 nm for AZO and CIGS surfaces, respectively. We used these values in the optical model to take into consideration the light scattering from the normally incident AM1.5G spectrum at rough interfaces. The model parameters used

Table 6.1: The model parameters used in TCAD simulations. A and D denote acceptor and donor, respectively. CB DOS and VB DOS represent density of states of conduction band minimum and valance band maximum, respectively. Subscript IF means interface. The parameters and values shown in bold are fitting parameters. CIGS/CdS column reports input data referring to the interface between CIGS and CdS layers. Data acquired from: CIGS: [162], [235], CdS [229], [235], [237], CIGS/CdS, i-ZnO and AZO: [235] and GZO-a: [221].

Layer parameter	Symbol [unit]	CIGS	CdS	CIGS/CdS	i-ZnO	AZO	GZO-a
Thickness	d [nm]	673	50		50	205	330
Bandgap	E_g [eV]	graded	2.4		3.3	3.3	3.25
FBC/IBC							
Electron affinity	χ [eV]	graded	4.2		4.3	4.3	4.3
FBC/IBC							
Rel. permittivity	ϵ_r	13.6	10		9	9	3.85
Doping	N_A, N_D [cm ⁻³]	2×10^{16}	5×10^{17}		1×10^{17}	1×10^{20}	3.2×10^{19}
		(A)	(D)		(D)	(D)	(D)
CB DOS	N_C [cm ⁻³]	6.8×10^{17}	1.3×10^{18}		3×10^{18}	3×10^{18}	3.7×10^{18}
VB DOS	N_V [cm ⁻³]	1.5×10^{19}	1×10^{19}		1.7×10^{19}	1.7×10^{19}	1.7×10^{19}
Mobility	μ_e, μ_h [cm ² V ⁻¹ s ⁻¹]	100,12.5	72,20		100,31	100,31	23,1.7
Defects							
Type	–	D	A	D	A	A	A
Concentration/ Density	N_T [cm ⁻³]/ N_{IF} [cm ⁻²]	5×10^{13}	2×10^{17}	1×10^{12}	1×10^{16}	1×10^{16}	1×10^{16}
Energy level	E_T	E_i	E_i	E_i	E_i	E_i	E_i
Cap. cross-sec.	σ_e, σ_h [cm ²]	5×10^{-13} , 1×10^{-15}	1×10^{-15} , 5×10^{-13}	5×10^{-13} , 1×10^{-15}	1×10^{-15} , 5×10^{-13}	1×10^{-15} , 5×10^{-13}	1×10^{-15}, 5×10^{-13}

in this work are summarised in Table 6.1. In these simulations, we have modelled the natural defects in the CIGS material with donor-type mid-gap recombination centres [235]. Note that our primary goal is not to model the exact complicated nature of the CIGS material. We rather replicated the cell's performance by using an equivalent recombination behaviour [235].

In our simulation framework, the mesh elements are forced to be smaller near interfaces to accurately account for interface recombination and charge transport. In case of CIGS with Ga grading, the change in the Ga content affects the wavelength-dependent optical constants - refractive index, $n(\lambda)$, and extinction coefficient, $k(\lambda)$ - and, hence, the bandgap and absorption coefficient. In this work, we use an energy-shift model [236] to calculate the optical constants of CIGS with an arbitrary Ga composition. In this respect, multiple sets of $n(\lambda)$ and $k(\lambda)$ with known Ga compositions [23], [162] were employed, from which the optical constants of intermediate arbitrary Ga contents were calculated. The optical constants of other materials were obtained from [72], [156], [168], [175], [176], [221].

6.3 Model calibration

We calibrated our simulations by comparing the J - V curves of the simulated FBC solar cells with those of the fabricated cells from TNO Solliance. From the light-

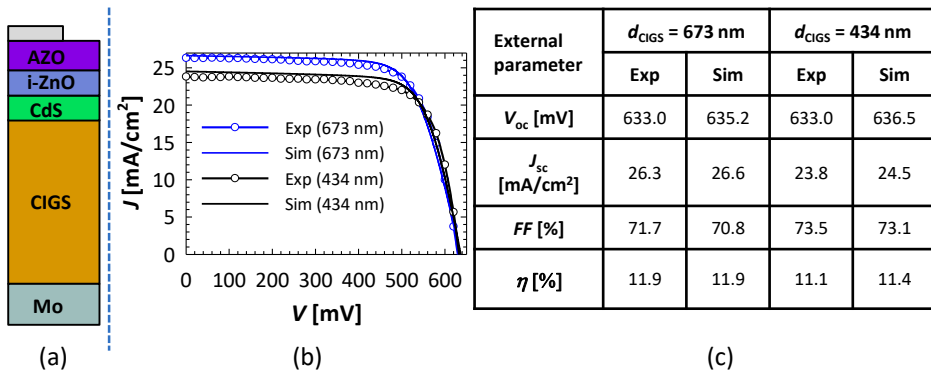


Figure 6.1: a) The reference FBC solar cell as modelled by TCAD (dimensions are not to scale). The dashed line shows the symmetry plane. b) J - V curves of the simulated and fabricated solar cells. The numbers in brackets indicate the absorber thickness. c) The measured and simulated external parameters of the reference FBC cell for two different absorber thicknesses.

facing side, the reference cell structure consists of AZO, intrinsic ZnO (i-ZnO), CdS, CIGS and Mo (Figure 6.1(a)). A close match between the simulated and measured external parameters - J_{sc} , V_{oc} , FF and η - for different absorber thicknesses indicates the validity of the model (Figure 6.1(b,c)). The fitting has been achieved by mostly adjusting the thickness of different layers, including the absorber layer. The variable absorber bandgap is included in the calibration models. Due to different deposition parameters for varying absorber thickness, the bandgap grading is different and sample-dependent. For instance, the 443-nm thick CIGS model was fitted to the experimental data by a slight increase of the bandgap towards the CIGS / Mo interface (from 1.17 eV to 1.21 eV). This in case of the 673-nm thick CIGS model was done by increasing the bandgap from 1.16 eV to 1.2 eV from the surface to the CIGS / Mo interface.

6.4 IBC design considerations

The not-in-scale schematic of the proposed IBC solar cell structure is shown in Figure 6.2(a). In a more realistic scale, the CIGS thickness will be even smaller than the gap width (Gap). The absorber thickness is kept similar to that of the reference FBC solar cell (673 nm) for fair comparison. The model is mirror-like symmetric at half of the h-contact and periodic in x direction. In **Chapter 5** [181], we optimized an Al_2O_3 / MgF_2 -based double-layer ARC for an IBC solar cell with natural surface morphology. The gradual change in the refractive index from MgF_2 to CIGS provides a wideband antireflection effect. The optimal thicknesses of Al_2O_3 and MgF_2 for this work are 80 and 85 nm, respectively. The Al_2O_3 layer at the front side of the absorber serves also as chemical and electrical passivation layer. An annealing step at 400-450 °C will activate negative fixed charges with densities as high as $1 \times 10^{13} \text{ cm}^{-2}$ at the CIGS / Al_2O_3 interface, leading to electrical passivation of the interface [139], [175]. The

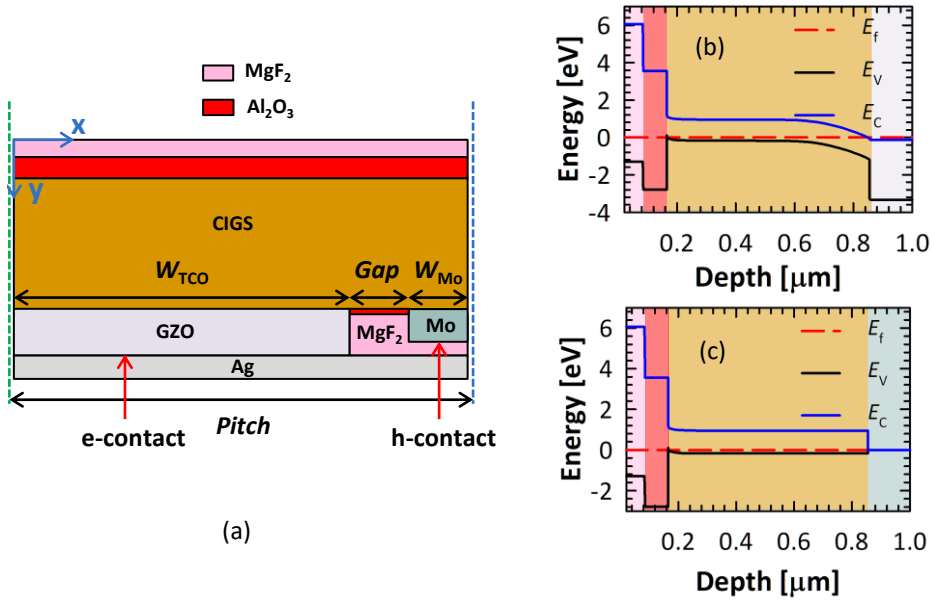


Figure 6.2: a) The schematic of the IBC solar cell (dimensions are not to scale) with symmetry (dashed blue) and periodicity (dashed green) lines. b) and c) The band diagram of the e-contact and h-contact, respectively. The depth corresponds to the distance from the front surface of the ARC layer.

presence of these fixed charges is considered in the model at the CIGS / Al₂O₃ interface both at the front and at the rear side of the absorber material. It is worth noting that the typical front layers in the FBC structure, i.e. CdS, i-ZnO and AZO are both not needed in and even detrimental to the IBC structure. This is because of parasitic absorption and the formation of a $p-n$ junction at the front side of the absorber, preventing the lateral transport of the charge carriers. Here the impact of the absorber quality on absorption is of secondary importance. In fact, the comparison between our reference FBC solar cell and the proposed IBC design is merely related to the performance difference of the same absorber in two different configurations.

At the rear side, a silver reflector is placed to reflect the photons from the rear side for a second-absorption chance. At the experimental level, however, the IBC structure could be realized on other substrates. The e- and h-contacts are separated by a dielectric stack consisting of MgF₂ and Al₂O₃ both to avoid electrical shunts and to increase the internal reflection due to the low refractive index of deployed dielectrics. The influence of the thin Al₂O₃ layer in electrical passivation will be studied in the following sections.

The e-contact is realized by an n -doped transparent conductive oxide (TCO). We intentionally did not use AZO for this purpose, because of its low thermal stability, which could become a problem at experimental level. In this case, gallium-doped zinc-oxide (GZO) type-a based on the work of Fujiwara et al. [221] was chosen. High doping

concentration, low absorption coefficient, high thermal stability and low free carrier absorption are some of the advantages of such a GZO material over its counterparts [221], [238]. Figure 6.2(b) shows the band diagram of the e-contact in dark condition. At the front side, the presence of negative fixed charges induces an electric field, which prevents the accumulation of electrons at the CIGS / Al_2O_3 interface (field effect passivation) [139]. Also, the accumulation of holes at the front interface helps with the lateral transport of majority charge carriers towards the molybdenum contact (i.e. the h-contact). The band bending at the rear side shows the formation of a p - n junction between CIGS and the degenerate semiconductor, GZO, which functions well for electron collection and hole rejection.

Similar to the conventional FBC CIGS solar cells, the majority carriers are collected using a Mo contact. As also plotted in Figure 6.2(c), the ohmic contact formed due to the formation of a very thin MoSe_2 layer at the CIGS / Mo interface enables the collection of holes [139].

6.5 Results and discussion

We have performed simulations by varying the geometrical parameters (Figure 6.2(a)) and absorber material characteristics to investigate the influence of each parameter on the cell performance. In each scenario, only one parameter is varied. After each step, the most suitable parameter value is selected for the rest of simulations to step-by-step complete the design of the proposed IBC structure. In-depth analysis of the charge density distribution or electric fields are provided when needed.

6.5.1 TCO width

We started with varying the TCO width (W_{TCO}), while keeping Gap and the Mo width (W_{Mo}) constant. Since the gap region is a non-collecting region, its width should be as small as possible. Hence, in these models, Gap is chosen to be $1\ \mu\text{m}$. Nonetheless, a sensitivity study on Gap will be provided in the following sections. Also, W_{Mo} should be smaller than or comparable to the minority carrier diffusion length to facilitate low carrier recombination. Therefore, it is kept at $500\ \text{nm}$. Note that due to symmetry, in the complete structure, this value means that the total width of Mo is $1\ \mu\text{m}$. Also, a change in W_{TCO} leads to a change in the size of the simulation domain, $Pitch$. The external parameters as functions of the changes in W_{TCO} are plotted in Figure 6.3. We observe that V_{OC} and J_{SC} increase as W_{TCO} increases. This can be explained by the reduction of electrical shading, which refers to the local reduction of J_{SC} due to charge carrier recombination at regions other than e-contact [239]. On the other hand, wider e-contact means that the majority carriers need to travel in longer distances to be collected at the h-contact. This explains the reducing trend of FF in Figure 6.3, which slightly outbalances the increasing trend of V_{OC} and J_{SC} for $W_{\text{TCO}} > 30\ \mu\text{m}$. For this reason and for the sake of fast simulations, we chose $W_{\text{TCO}} = 30\ \mu\text{m}$ for the rest of our studies. Already for such a non-optimized IBC architecture, the conversion efficiency is boosted to a value of 16.73%.

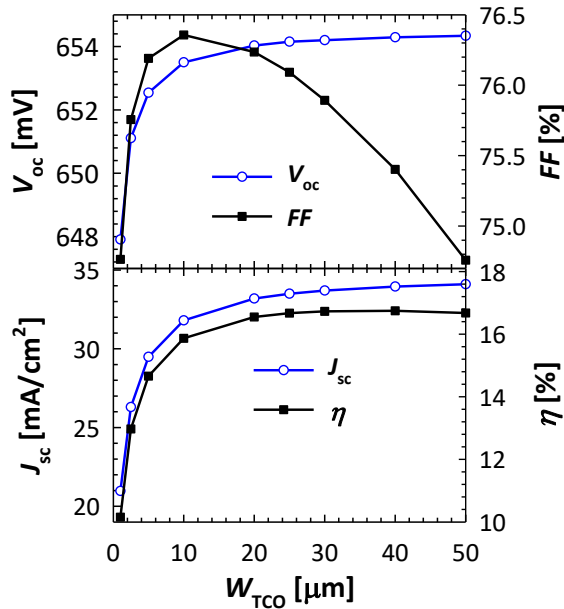


Figure 6.3: The external parameters as functions of W_{TCO} . The thickness of CIGS absorber layer is 673 nm.

6.5.2 Absorber thickness

We also studied the effect of the absorber thickness (d_{CIGS}) on the external parameters. We kept the bandgap constant at 1.16 eV and the rest of the geometrical parameters similar to the previous section. One would think that a thicker absorber naturally leads to higher current generation. However, as Figure 6.4(a) shows, the larger charge carrier generation (due to more light absorption) is debunked by more carrier recombination in the absorber bulk. The colour-plot in Figure 6.4(b) shows the charge carrier recombination rate in short-circuit conditions for two absorber thicknesses, namely, 690 nm and 1500 nm. The significantly higher recombination in the CIGS bulk can be explained by the black curves overlaid on the solar cells' cross-section. The curves represent the electrostatic potential as a function of depth under equilibrium conditions, from which the extent of the depletion region in the absorber (W) can be calculated. Knowing that the electrostatic potential is constant outside the space charge region and varies inside the region, we calculated W for the abovementioned thicknesses. Also, since the material properties, especially the doping concentrations at both sides of the metallurgical junction, are similar in both cases, it is not surprising that W is almost similar and equal to 430 nm. This means that the quasi-neutral region (in which charge carrier recombination occurs) in the thicker solar cell is larger, resulting in higher recombination. It can be concluded that for the same material properties, thickening the CIGS layer does not necessarily improve the device performance.

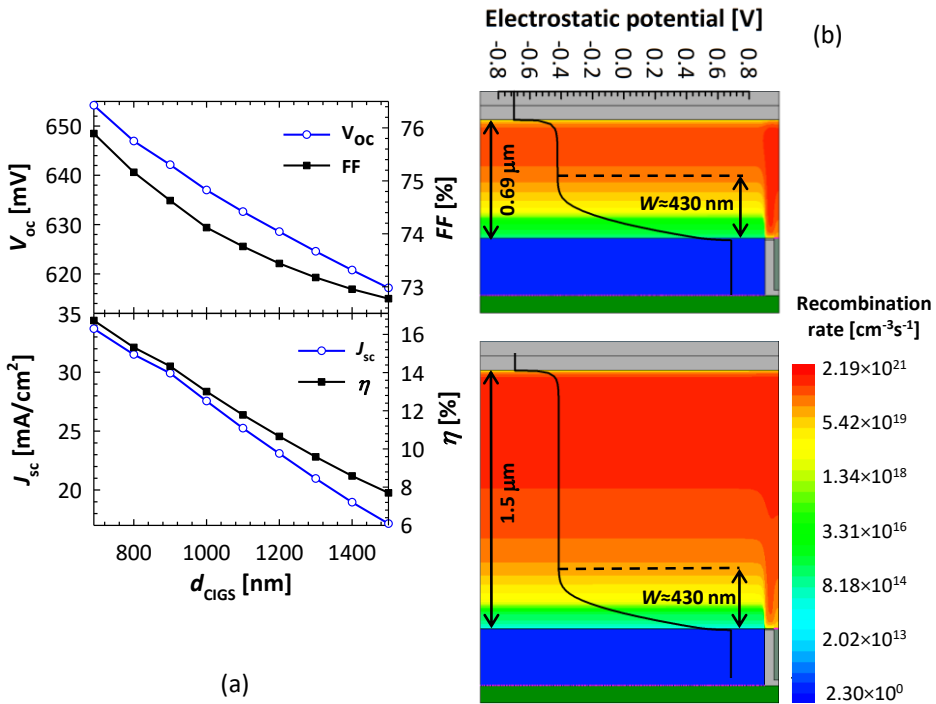


Figure 6.4: a) The external parameters as functions of d_{CIGS} . The bandgap is constant at 1.16 eV. b) Top and bottom: the cross-section of the IBC solar cell with 690 and 1500 nm CIGS thickness, respectively. The colour plot shows the recombination rate under short-circuit conditions. The black curve overlays show the electrostatic potential in equilibrium as a function of depth along the ARC, CIGS and TCO layers.

6.5.3 Bandgap grading

So far, the absorber bandgap was fixed at 1.16 eV, which according to Minoura et al. [23] corresponds to $\text{GGI} = 0.22$. GGI is defined as the compositional ratio of group III elements in the absorber: $\text{GGI} = [\text{Ga}] / ([\text{Ga}] + [\text{In}])$. We engineered the absorber bandgap by varying GGI according to energy shift model, described above. Two approaches were taken: i) constant GGI (0.22) in the first half of absorber thickness (with respect to the front side) and then linear increase of GGI towards the rear side and ii) linear increase of GGI towards the front side in the first half and then constant GGI in the bottom half of the absorber. In both cases, the maximum value of GGI is 0.9, corresponding to $E_{g\text{-CIGS}} = 1.64$ eV. Note that this linear profile is merely a simple approach to probe the effect of two opposite bandgap gradings on the cell's performance. Such semi-linear profile is already demonstrated in the work of Mansfield et al. [33]. More complicated profiles and/or higher (fixed) bandgap can be investigated in future studies. Figure 6.5 demonstrates the external parameters as functions of front-

and rear-side GGI (left-hand side and right-hand side of the dashed line, respectively). The red dashed line corresponds to a constant Ga content of 0.22. It is observed that increasing the Ga content towards the front side of the CIGS layer leads to an increasing trend in V_{OC} . This can be explained by larger quasi-Fermi level splitting due to higher absorber bandgap [8]. Also, there is an optimal value for J_{SC} and η at Front GGI = 0.4. Figure 6.6(a) and (b) provide more information about the reason for this optimum value. According to Figure 6.6(a), which shows the band diagram (in equilibrium) in the top part of the CIGS layer in case of front-side Ga grading, the more the bandgap at the front side of the absorber, the higher is the slope of the conduction band minimum energy. This results in a stronger electric field in that region, increasing the drift of electrons from the front interface towards the bulk region (the corresponding current has the opposite direction). On the other hand, as can be seen in Figure 6.6(b), an increase in the front-side GGI leads to steeper electron density curve as a function of distance from the front interface. This promotes larger electron diffusion in the direction of the front interface, which counteracts with the drift current. At an optimal value of Front GGI (here, 0.4), the two components of current density outbalance each other, leading to maximum J_{SC} , and, hence, η . This improves the efficiency from 16.73% for the IBC cell with constant bandgap to 17.87% for the IBC cell with optimal bandgap grading.

On the other hand, according to the right-hand side of Figure 6.5, rear-side Ga grading drastically reduces the cell performance. Although bandgap increase at the bottom half of the absorber improves V_{OC} , the rest of the external parameters reduce with increasing Rear GGI. The reason is explained by studying the band diagram in the corresponding part of the structure (Figure 6.6(c)). We observe the formation of an electron barrier at the CIGS / GZO interface for more Rear GGI. This, in turn, leads to the repulsion of the minority charge carriers from their related contact, and, therefore, to an increase in recombination rate in the absorber (Figure 6.6(d)). A similar grading in FBC CIGS solar cells enhances the efficiency due to better passivation of the rear contact [33]. We therefore, selected a front-side linear Ga grading with Front GGI = 0.4 as the optimal grading for the rest of simulations. This type of grading can be achieved by altering the CIGS three-stage co-evaporation process such that in the first stage, copper (Cu) and selenium (Se) are evaporated, followed by the second stage with Se, In and Ga [240].

It is worth noting that in case of a different absorber thickness, the optimal grading can be different. The results of our thickness-dependent grading optimization are not shown here for brevity.

6.5.4 TCO coverage

As discussed above, large values of W_{TCO} lead to less electrical shading, and, therefore, to large J_{SC} values. However, Mo contacts wider than what we have considered so far would be less complex to produce. This trade-off is investigated in this section. Here, we define a parameter $Ratio = W_{TCO}/Pitch$, and vary it, while keeping $Pitch$ and Gap constant. In this respect, smaller $Ratio$ (smaller W_{TCO}) means larger W_{Mo} . The results are presented in Figure 6.7(a). As expected, stronger electrical shading results from smaller $Ratio$ values, thus significantly compromising J_{SC} and η . However,

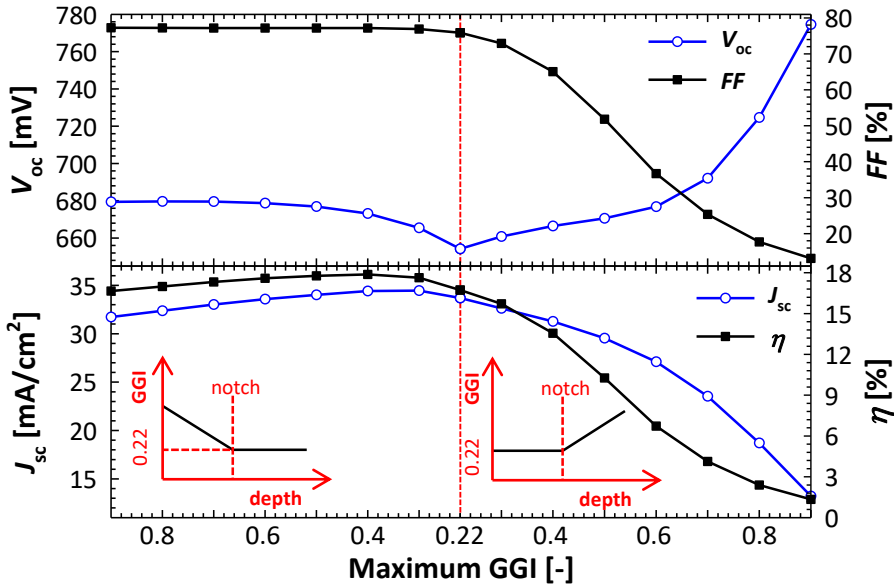


Figure 6.5: The external parameters as functions of Ga composition. The red dashed line shows the IBC cell with fixed bandgap. Left-hand side of the dashed line: front side grading. Right-hand side of the dashed line: rear side grading.

reducing Ratio to about 90% still results in $\eta > 17\%$, which is considerably larger than the efficiency of the FBC reference solar cell. This would allow us to increase W_{Mo} to $2\ \mu\text{m}$, i.e. four times wider than the initial value, and therefore, be able to use less complicated and cheaper (lithography) steps for the formation of the h-contact. For this reason, we modified the geometry with a wider Mo contact for further studies ($\eta = 17.02\%$).

6.5.5 Bulk trap density in CIGS

So far, the bulk defect density (N_{T-CIGS}) in the CIGS material was fixed at $5 \times 10^{13}\ \text{cm}^{-3}$. However, as the quality of CIGS material can be sensibly better than the one used in our work [33], [228], [241], we studied the impact of N_{T-CIGS} on the external parameters (Figure 6.7(b)). As expected, a high defect density in the absorber significantly deteriorates the efficiency. On the other hand, improving the material quality, for instance decreasing N_{T-CIGS} from $5 \times 10^{13}\ \text{cm}^{-3}$ to $1 \times 10^{13}\ \text{cm}^{-3}$ can boost the efficiency from 17% to 19.7%. As a result, V_{OC} is increased to values comparable to that of the record CIGS solar cell [14], [27]. For a better comparison, the efficiency of the reference FBC solar cell with $N_{T-CIGS} = 1 \times 10^{13}\ \text{cm}^{-3}$ would have been 12.5%.

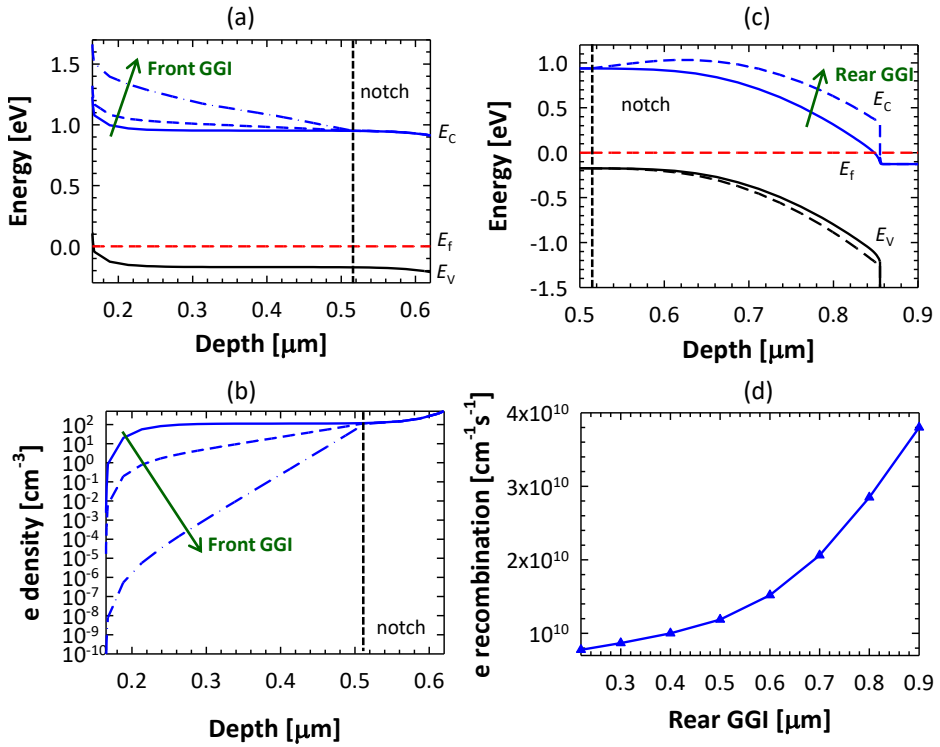


Figure 6.6: a) and b) The band diagram and the density of electrons as a function of depth from the front side of the cell in case of front-side grading for Front GGI= 0.22 (solid), 0.4 (short dash) and 0.9 (dash-dot), c) The band diagram in the bottom half of the CIGS layer for Rear GGI= 0.22 (solid) and 0.9 (short dash) and d) The integrated minority carrier recombination rate in the absorber in short circuit conditions as a function of Rear GGI.

This emphasises the importance of improving the fabrication process of the CIGS material in the final device performance.

6.5.6 Gap width

In the previous sections, we briefly mentioned that Gap should be as narrow as possible for better charge collection. Indeed, our simulations for different Gap widths from 20 nm to $6\ \mu\text{m}$ confirm this. In these models, we kept W_{TCO} and W_{Mo} constant at 28.5 and $2\ \mu\text{m}$, respectively. $N_{\text{T-CIGS}}$ is equal to the reference case of $5 \times 10^{13}\ \text{cm}^{-3}$. Increasing Gap to values larger than $1\ \mu\text{m}$ mainly affects J_{SC} with a decreasing trend, while other external parameters are nearly unchanged. This is mainly due to the increased hole recombination as a result of larger distance between the generation point and the h-contact. On the other hand, even a gap as narrow as 20 nm is sufficient for high J_{SC} values and avoiding shunts, increasing the efficiency from 17.02% ($1\text{-}\mu\text{m}$

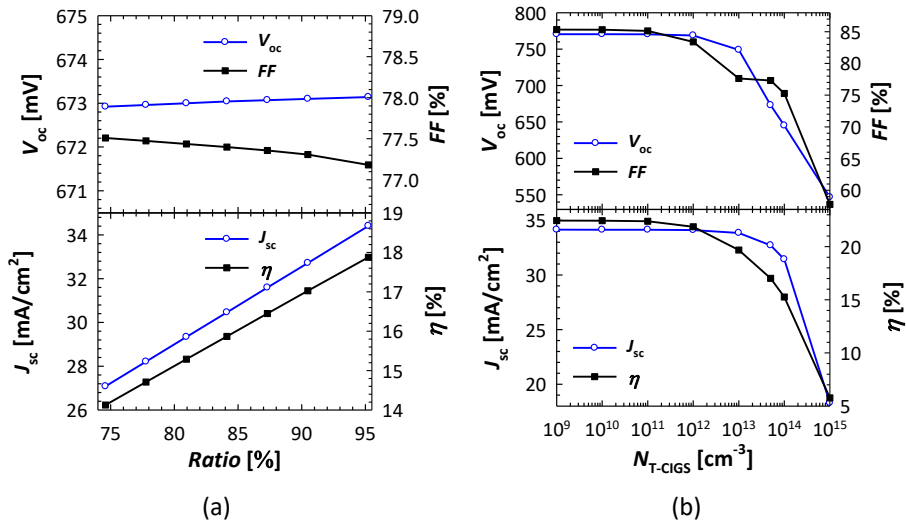


Figure 6.7: The external parameters as functions of a) $Ratio = W_{TCO}/Pitch$, and b) the bulk donor-type trap density in the absorber.

wide gap) to 17.34% (20-nm wide gap). From experimental point of view, this is of course more challenging than a 1- μ m wide gap. The significant role of the Al₂O₃ layer in the passivation of the contacts is exemplified in Figure 6.8. There, the electric field vectors are overlaid on the electron density colour plot of the IBC solar cell in equilibrium in two cases: (a) with and (b) without active negative fixed charges in the Al₂O₃ layer. The arrow size shows the intensity of the electric field. The direction of the electric field in case (a) indicates the repulsion of the electrons from the gap area, ensuring the field-effect passivation of the region. This is proved by the colour map of e density in both figures, showing a high density of electrons around the gap and the h-contact in case (b). In case (b), the resulting higher recombination rate degrades all the external parameters and reduces the efficiency from 17.34% to 14.42%.

6.5.7 Optimal IBC vs reference FBC

The J - V and EQE curves of the selected IBC design are compared to the reference FBC solar cell with $d_{CIGS} = 673$ nm. Note that in this case, the *optimal* design is different from the *ideal* designs studied in sections 6.5 and 6.6. The former is less experimentally challenging with 90% TCO coverage, 1 μ m *Gap* and the reference trap density in the absorber material. The improvement in all the external parameters is evident in Figure 6.9. The difference between EQE and internal quantum efficiency (IQE) curves of the IBC solar cell in Figure 6.9(b) is an indication of incomplete charge carrier collection that yet needs to be addressed. Nonetheless, the difference between the EQE spectra of the two structures is substantial. It should also be noted

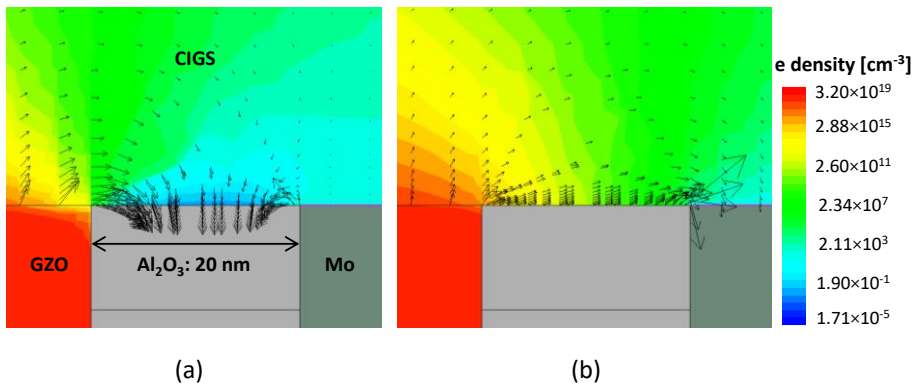


Figure 6.8: Colour plot: electron density, arrows: electric field in equilibrium for the IBC cell a) with negative fixed charges in the Al_2O_3 layer and b) without any fixed charges. The geometrical features of both figures are the same.

that unlike the optically optimized IBC structure in our previous work (**Chapter 5** [209]), the flat interface design of the IBC solar cell in this work results in lower values of IQE . Better light in-coupling can be achieved by a more effective ARC [181], [209].

6.6 Conclusion

We proposed and optimized an IBC structure for boosting the efficiency of a CIGS solar cell with a sub-micron thickness (precisely, 673 nm). In this configuration, the parasitic absorption of the front layers and the optical shading of the front-contact are prevented. We used 2-D opto-electrical simulations in TCAD Sentaurus environment to accurately model such solar cell architecture. The study of the band diagram shows a good electrical passivation at the front side of the absorber due to the negative charges in the Al_2O_3 layer. Also, the band bending in the CIGS / e-contact interface area is an indication of an effective electron-selective contact.

The study of the TCO width shows that the wider the TCO is, the less the electrical shading is and the higher the efficiency is. Increasing the absorber thickness, while keeping the electronic features constant, results in higher charge carrier recombination in the absorber bulk, and, hence, worse performance. This is because of a larger quasi-neutral region with respect to the total bulk area in thicker absorbers.

We showed that a bandgap grading with higher bandgap at the front side of the CIGS layer improves the efficiency by 1.1 abs.%, compared to the case with constant bandgap. However, because of the trade-off between the resulting drift and diffusion currents, there is an optimum grading for maximum efficiency. Note that the optimal grading can vary with the absorber thickness.

Our studies on the geometrical properties of the e- and h-contacts show that although a wider TCO and a narrower Mo (less than $1\ \mu\text{m}$) are more favourable for higher efficiencies, this complicates the fabrication of the Mo layer. This can be ad-

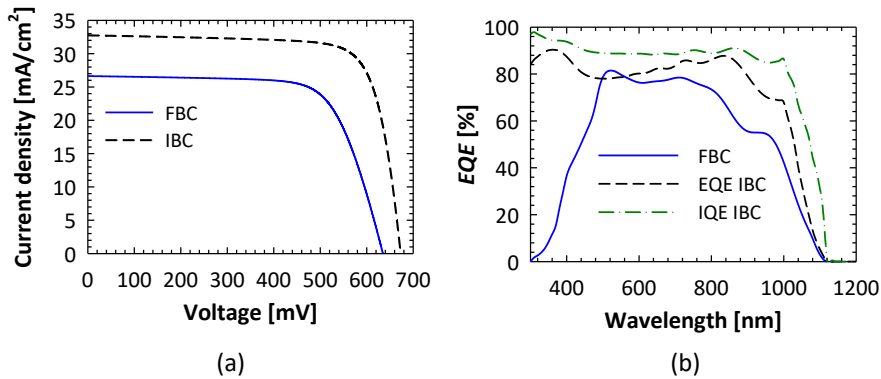


Figure 6.9: Comparison between the reference FBC and the optimized IBC solar cells. a) current density vs voltage and b) EQE and IQE .

dressed by reducing the TCO width (hence, widening Mo) from $30\ \mu\text{m}$ to $28.5\ \mu\text{m}$ at the expense of about 0.8 abs.% loss in efficiency. In this case, compared to 11.9% for the reference FBC solar cell, the IBC structure shows a conversion efficiency of 17%.

Since the quality of our simulated absorber from defect density point of view is lower than the state-of-the-art CIGS absorber material, we studied the effect of defect density on the cell performance. We observed that by reducing the bulk defect density from $5 \times 10^{13}\ \text{cm}^{-3}$ to $1 \times 10^{13}\ \text{cm}^{-3}$, the efficiency can be improved to 19.7%.

The sensitivity of the performance on the gap width was checked by changing Gap from 20 nm to $6\ \mu\text{m}$. The higher recombination with a wider gap reduces the current density. On the other hand, the performance improves as Gap is shrunk. The electric field map shows that the presence of negative fixed charges in the Al_2O_3 layer ensures the electrical passivation and low recombination at small Gap values.

We showed how an IBC structure with optimal bandgap grading and high absorber quality can help us achieve high efficiencies with sub-micron CIGS layers. Indeed, better optical performance is still possible by, for example, high aspect ratio ARC [209]. Although the proposed structure needs to answer many fabrication challenges, including potentially-costly patterning steps, it can pave the way towards high efficiency thin-film CIGS solar cells and their deployment in three- and four-terminal tandem devices.

7

Conclusion and Outlook

In this thesis, sub-micron CIGS solar cells were studied. The questions about the nature of optical losses at the back contact were answered and different light management schemes to reduce the optical losses were presented. A fast and accurate simulation optimization method was instrumental in designing a new anti-reflection coating (ARC) for CIGS solar cells and finally, with a new perspective, an interdigitated back-contacted (IBC) structure was proposed for CIGS solar cells for the first time.

7.1 Conclusions

In **Chapter 2**, first, the absorption benchmarks of CIGS solar cells (also known as Green absorption limit) as a function of absorber thickness and bandgap were studied. It was shown that for thin absorbers, the absorption limit is more dependent on wavelength, while for thicker absorbers ($> 1.5 \mu\text{m}$), it is more constant until an abrupt reduction near bandgap wavelength. We also showed that increasing the CIGS thickness more than a certain value has no additional gain on optical performance and hence, should be avoided for the sake of production cost and time. In the same chapter, different optical and electrical simulation tools (such as Ansys HFSS, CROWM, GenPro4, ASA, Quokka and Sentaurus TCAD), especially those employed in this thesis were introduced and compared to each other.

Optical losses at the rear contact of CIGS solar cells were studied in **Chapter 3**. A theoretical study shows that leaky surface waves can be excited at Mo / CIGS interface in wavelength ranges between 300 and 980 nm, contributing to dissipation of photons mostly in the Mo layer. From 980 to 1200 nm, the presence of as-grown nano-textures at the interface of interest provides sufficient conditions for the excitation of surface plasmon polaritons, which lead to the confinement of the photons to the interface without contribution to charge carrier generation. In this respect, a double-layer dielectric spacer with periodic point contacts was optimized in an optical modelling platform to quench the abovementioned losses. It was shown that for a 750-nm thick CIGS absorber, an Al_2O_3 / MgF_2 (10 and 100 nm thick, respectively) stack with point contacts covering 25% of the rear surface can potentially boost the photocurrent density, J_{ph} , by 5.27%. This improvement is with respect to the reference solar cell with the same absorber thickness and without light management.

Targeting reflection losses at the front side of the solar cell, in **Chapter 4**, we studied a porous-on-compact ARC based on MgF_2 . By introduction of porosity in MgF_2 , its refractive index can be tuned. This can be used in achieving a wide-band (effective in

a wide wavelength range) anti-reflection effect. Using effective medium approximation and sequential nonlinear programming (SNLP) algorithm in Ansys HFSS simulation environment, we established an optimization scheme for multi-layer ARCs' that can be applied to different structures. In case of a 750-nm thick absorber, the resulting ARC improves J_{ph} by 6.77% (compared to the cell with the same absorber thickness and no ARC). It also proves more resilient against the light's angle of incidence compared to the conventional single-layer MgF_2 anti-reflection coating. The study of J_{ph} and J_{Loss-R} (current density lost as a result of reflection, Equation 3.3) as two different optimization cost functions confirmed that indeed there is an opposite trend in the two parameters and an optimal ARC design can be achieved using either of the two cost functions. Joining this ARC at the front side of the solar cell to double-layer dielectric spacer at the rear side (studied in **Chapter 3**), a wide-band light management is achieved, reducing the optical losses in the whole spectrum of interest. The outcome is 11.3% improvement in J_{ph} of a 750-nm thick CIGS absorber from 28.04 mA/cm² to 31.22 mA/cm², which is even higher than J_{ph} of a 1600-nm thick absorber without applied light management.

In the rest of the thesis, the focus was turned from conventional front- and back-contacted (FBC) configuration to a novel (in CIGS field) interdigitated back-contacted (IBC) structure. The goal was to completely remove the parasitic losses that are inherent to the front buffer and window layers in typical FBC structures. In **Chapter 5**, the proposed IBC structure (see Figure 5.1 and 5.2) was probed for optical performance and the results were compared to the Green absorption benchmark (see Equation 5.1). The ARC effect was achieved with an Al_2O_3 / MgF_2 stack at the front side of the cell in two texturing configurations: i) high aspect ratio textures and ii) as-grown morphology of CIGS. At the rear side, the electron- and hole-contacts (e- and h-contacts, respectively) were separated by a dielectric spacer to avoid electrical shunts (also called Gap). We chose gallium-doped zinc oxide (GZO) for the e-contact (TCO in Figure 5.1), because of high carrier concentration, low free-carrier absorption and high thermal stability. Mo was selected as the h-contact material. Thin layers of Al_2O_3 covering the dielectric spacer and the front surface of CIGS ensure electrical passivation. The optimization variables for maximal J_{ph} were several geometrical parameters, such as the width and height of TCO and the thickness of the ARC layers. The reference cell was an FBC CIGS solar cell with a 750-nm thick absorber and without light management. The results showed that with high aspect ratio ARC, J_{ph} of a 750-nm thick absorber can be boosted by 41.55%, which is only 6.65% lower than the Green absorption benchmark. In case of as-grown CIGS morphology at the front side, also a small deviation from the Green benchmark (7.7%) was accomplished. This is significantly lower than the case of the reference FBC solar cell (33.4%). In summary, this optical study, emphasized the great potential of IBC configuration for CIGS solar cells and the research continued with electrical modellings.

The IBC structure proposed in **Chapter 5** was opto-electrically optimized utilizing the Sentaurus simulation environment and the results were covered in **Chapter 6**. At first, the model inputs were calibrated using the experimental measurements of FBC CIGS solar cells performed at Solliance for different absorber thickness. The bandgap grading of the CIGS layer was included in the models using an energy-shift model [23]. An FBC cell (Figure 6.1) with 673-nm thick absorber and 11.9% efficiency was selected

as the reference cell. Different geometrical and material properties (Figure 6.2), such as the widths of contacts and the gap region, the period of the unit cell, the absorber thickness and bandgap grading and the defect density in the absorber were investigated in **Chapter 6**. We showed that the electrical shading is less for wider TCO and also, that thicker absorber with the same material properties leads to more charge carrier recombination in the bulk. Also, higher Ga content (i.e. higher bandgap) at the rear side of the absorber is detrimental to the external parameters due to the formation of an electron barrier at the minority carrier contact (e-contact). This is in contrast with the typical Ga grading in FBC CIGS solar cells. On the other hand, the efficiency can be increased by more than 1 abs.% by increasing the bandgap towards the front interface (see Figure 6.5). The study of the Mo width (W_{Mo}) shows that wider Mo leads to the reduction of short-circuit current density, J_{SC} . A 2- μm wide Mo contact results in almost 17% efficiency. Also, a wider gap (the dielectric spacer between TCO and Mo) negatively affects J_{SC} due to the larger distance between the generation point of minority charge carriers (here, electrons) and the e-contact. In another study, the map of the electrostatic field in the vicinity of the gap (Figure 6.8) highlighted the significant role of the negative fixed charges of the Al_2O_3 layer in electrical passivation of the contacts. Finally, the current density vs voltage (J - V) and external quantum efficiency (EQE) curves of the reference FBC and the optimal IBC cells were compared and showed substantial improvements in all external parameters. Indeed, an improvement from 11.9% to 17% in efficiency indicates the high potential of the proposed IBC structure for high performance sub-micron CIGS solar cells. Although this structure still needs to overcome many practical issues at the experimental level, it can serve as a solid starting point for the research community, engaging in out-of-the-box CIGS solar cell architectures.

7.2 Outlook

As a result of the understandings obtained during this thesis, the following recommendations are offered for future research:

- Despite the high potential of CIGS as a highly absorptive, stable and opto-electrically tunable thin-film material, little theoretical research is being performed to deeply understand and analyze it. In-depth 3-D opto-electrical modelling of CIGS solar cells with the incorporation of grains, crystal orientations, material composition and the corresponding defects and doping concentrations is of great value for future research. Such theoretical study should progress hand-in-hand with advanced material characterizations. This not only will answer the fundamental questions related to the performance of the CIGS material in the solar cell structure, but also will spark new ideas on how to improve CIGS solar cells to avoid losses and recombination issues and to increase the charge carrier lifetime at material level.
- A prototype IBC CIGS solar cell (see Figure 6.2) can be fabricated in superstrate configuration. MgF_2 and Al_2O_3 ARC layers, respectively, can be deposited on a glass superstrate, followed by the co-evaporation of the CIGS layer. The

GZO contact will be sputtered on the CIGS layer. A lithography step will create periodic gaps for the dielectric stack. Then, this stack is formed by the deposition of a thin Al_2O_3 layer followed by the MgF_2 layer. A second lithography step will provide periodic spaces for the sputtering of the Mo contact. The charge carrier collection will be facilitated by two perpendicular busbars at different elevations with respect to the rear side of the CIGS layer. Of course, the proposed flowchart can change towards more practical and perhaps budget-friendly fabrication.

Bibliography

- [1] UN. (2019). World population prospects 2019, [Online]. Available: <https://population.un.org/wpp/Graphs/DemographicProfiles/Line/900> (visited on 05/29/2020).
- [2] Worldometer, *World population*. [Online]. Available: <https://www.worldometers.info/world-population/> (visited on 04/22/2020).
- [3] B. Petroleum, "BP Statistical Review of World Energy Report," *BP London, UK*, 2019.
- [4] R. E. N. Members, *Renewables 2019 Global Status Report*. 2019, p. 336.
- [5] H. R. Roser and Max, "CO₂ and Greenhouse Gas Emissions," *Our World Data*, 2020. [Online]. Available: <https://ourworldindata.org/co2-and-other-greenhouse-gas-emissions> (visited on 06/02/2020).
- [6] C. B. Field, *Climate change 2014–Impacts, adaptation and vulnerability: Regional aspects*. Cambridge University Press, 2014.
- [7] R. Perez and M. Perez, "A fundamental look at supply side energy reserves for the planet," *Int. Energy Agency SHC Program. Sol. Updat*, vol. 62, pp. 4–6, 2015.
- [8] A. Smets, K. Jäger, O. Isabella, R. van Swaij, and M. Zeman, *Solar Energy: The physics and engineering of photovoltaic conversion, technologies and systems*. UIT Cambridge Limited, 2016.
- [9] A.-E. Becquerel, "Recherches sur les effets de la radiation chimique de la lumiere solaire au moyen des courants electriques," *CR Acad. Sci*, vol. 9, pp. 145–149, 1839.
- [10] A. Einstein, "Über einen die Erzeugung und Verwandlung des Lichtes betreffenden heuristischen Gesichtspunkt," *Annalen der physik*, vol. 322, no. 6, pp. 132–148, 1905.
- [11] S. M. Sze and K. K. Ng, *Physics of semiconductor devices*. John wiley & sons, 2006.
- [12] M. A. Green, "Self-consistent optical parameters of intrinsic silicon at 300 K including temperature coefficients," *Solar Energy Materials and Solar Cells*, vol. 92, no. 11, pp. 1305–1310, 2008.
- [13] *Imec and SunPower's parent Total working on n-type PERT bi-facial cell technologies*. [Online]. Available: <https://www.pv-tech.org/news/imec-and-sunpowers-parent-total-working-on-n-type-pert-bi-facial-cell-techn> (visited on 04/28/2020).
- [14] M. A. Green, E. D. Dunlop, D. H. Levi, J. Hohl-Ebinger, M. Yoshita, and A. W. Ho-Baillie, "Solar cell efficiency tables (version 54)," *Progress in Photovoltaics: Research and Applications*, vol. 27, no. 7, pp. 565–575, 2019.

- [15] IRENA, "Future of Solar Photovoltaic: Deployment, investment, technology, grid integration and socio-economic aspects (A Global Energy Transformation: paper)," Tech. Rep., 2019.
- [16] A. Jäger-Waldau, *PV Status Report 2019*. Publications Office of the European Union, 2019, p. 336.
- [17] Simon Philipps. (2020). Photovoltaics Report, [Online]. Available: <https://www.ise.fraunhofer.de/content/dam/ise/de/documents/publications/studies/Photovoltaics-Report.pdf> (visited on 09/02/2020).
- [18] J. L. Shay, S. Wagner, and H. M. Kasper, "Efficient CuInSe₂/CdS solar cells," *Applied Physics Letters*, vol. 27, no. 2, pp. 89–90, 1975.
- [19] L. L. Kazmerski, F. R. White, and G. K. Morgan, "Thin-film CuInSe₂/CdS heterojunction solar cells," *Appl. Phys. Lett.*, vol. 29, no. 4, pp. 268–270, 1976.
- [20] R. A. Mickelsen, W. S. Chen, Y. R. Hsiao, and V. E. Lowe, "Polycrystalline thin-film CuInSe₂/CdZnS solar cells," *IEEE Transactions on Electron Devices*, vol. 31, no. 5, pp. 542–546, 1984.
- [21] A. M. Gabor, J. R. Tuttle, D. S. Albin, M. A. Contreras, R. Noufi, and A. M. Hermann, "High-efficiency CuIn_xGa_{1-x}Se₂ solar cells made from (In_x, Ga_{1-x})₂Se₃ precursor films," *Applied Physics Letters*, vol. 65, no. 2, pp. 198–200, 1994.
- [22] S. R. Kodigala, *Cu (In_{1-x}Ga_x) Se₂ Based thin film solar cells*. Academic Press, 2011, vol. 35.
- [23] S. Minoura, T. Maekawa, K. Kodera, A. Nakane, S. Niki, and H. Fujiwara, "Optical constants of Cu(In,Ga)Se₂ for arbitrary Cu and Ga compositions," *Journal of Applied Physics*, vol. 117, no. 19, 2015.
- [24] R. Scheer and H.-W. Schock, *Chalcogenide Photovoltaics*. 2011.
- [25] S. Kim, J. Nishinaga, Y. Kamikawa, S. Ishizuka, T. Nagai, T. Koida, H. Tampo, H. Shibata, K. Matsubara, and S. Niki, "Reduced recombination in a surface-sulfurized Cu(InGa)Se₂ thin-film solar cell," *Japanese Journal of Applied Physics*, vol. 57, no. 5, p. 055701, 2018.
- [26] M. Kovacic, J. Krc, B. Lipovsek, W. C. Chen, M. Edoff, P. J. Bolt, J. van Deelen, M. Zhukova, J. Lontchi, D. Flandre, P. Salomé, and M. Topic, "Light management design in ultra-thin chalcopyrite photovoltaic devices by employing optical modelling," *Solar Energy Materials and Solar Cells*, vol. 200, no. April, 2019.
- [27] M. Nakamura, K. Yamaguchi, Y. Kimoto, Y. Yasaki, T. Kato, and H. Sugimoto, "Cd-Free Cu(In,Ga)(Se,S)₂ Thin-Film Solar Cell With Record Efficiency of 23.35%," *IEEE Journal of Photovoltaics*, vol. 9, no. 6, pp. 1863–1867, Nov. 2019.
- [28] H. Sugimoto, "High efficiency and large volume production of CIS-based modules," in *2014 IEEE 40th Photovoltaic Specialist Conference (PVSC)*, IEEE, 2014, pp. 2767–2770.

-
- [29] *MiaSolé Breaks World Record Again: Large Area Flexible Photovoltaic Module with 18.64% Efficiency*. [Online]. Available: <http://miasole.com/miasole-breaks-world-record-again-large-area-flexible-photovoltaic-module-with-18-64-efficiency/> (visited on 06/02/2020).
- [30] J. de Wild, D. G. Buldu, T. Schnabel, M. Simor, T. Kohl, G. Birant, G. Brammertz, M. Meuris, J. Poortmans, and B. Vermang, "High V_{OC} upon KF Post-Deposition Treatment for Ultrathin Single-Stage Coevaporated $Cu(In,Ga)Se_2$ Solar Cells," *ACS Applied Energy Materials*, vol. 2, no. 8, pp. 6102–6111, 2019.
- [31] N. Naghavi, F. Mollica, J. Goffard, J. Posada, A. Duchatelet, M. Jubault, F. Donsanti, A. Cattoni, S. Collin, P. P. Grand, J. J. Greffet, and D. Lincot, "Ultrathin $Cu(In,Ga)Se_2$ based solar cells," *Thin Solid Films*, vol. 633, pp. 55–60, 2017.
- [32] G. Yin, M. Song, and M. Schmid, "Rear point contact structures for performance enhancement of semi-transparent ultrathin $Cu(In,Ga)Se_2$ solar cells," *Solar Energy Materials and Solar Cells*, vol. 195, no. December 2018, pp. 318–322, 2019.
- [33] L. M. Mansfield, A. Kanevce, S. P. Harvey, K. Bowers, C. Beall, S. Glynn, and I. L. Repins, "Efficiency increased to 15.2% for ultra-thin $Cu(In,Ga)Se_2$ solar cells," *Progress in Photovoltaics: Research and Applications*, vol. 26, no. 11, pp. 949–954, Nov. 2018.
- [34] J. Goffard, C. Colin, F. Mollica, A. Cattoni, C. Sauvan, P. Lalanne, J.-F. Guillemoles, N. Naghavi, and S. Collin, "Light trapping in ultrathin CIGS solar cells with nanostructured back mirrors," *IEEE Journal of Photovoltaics*, vol. 7, no. 5, pp. 1433–1441, 2017.
- [35] O. Poncelet, R. Kotipalli, B. Vermang, A. Macleod, L. A. Francis, and D. Flandre, "Optimisation of rear reflectance in ultra-thin CIGS solar cells towards > 20% efficiency," *Solar Energy*, vol. 146, pp. 443–452, Apr. 2017.
- [36] J. Krc, M. Sever, A. Campa, Z. Lokar, B. Lipovsek, and M. Topic, "Optical confinement in chalcopyrite based solar cells," *Thin Solid Films*, vol. 633, pp. 193–201, 2017.
- [37] L. Goullart, W.-c. Chen, A. Cattoni, J. Goffard, L. Riekehr, J. Keller, M. Jubault, N. Naghavi, M. Edoff, and S. Collin, "Reflective Back Contacts for Ultrathin $Cu(In,Ga)Se_2$ -Based Solar Cells," *IEEE Journal of Photovoltaics*, vol. PP, pp. 1–5, 2019.
- [38] A. J. Blanker, P. Berendsen, N. Phung, Z. Vroon, M. Zeman, and A. H. M. Smets, "Advanced light management techniques for two-terminal hybrid tandem solar cells," *Solar Energy Materials and Solar Cells*, vol. 181, no. September 2017, pp. 77–82, 2018.
- [39] L. Kronik, D. Cahen, and H. W. Schock, "Effects of sodium on polycrystalline $Cu(In,Ga)Se_2$ and its solar cell performance," *Adv. Mater.*, vol. 10, no. 1, pp. 31–36, 1998.

- [40] D. Rudmann, D. Brémaud, A. F. Da Cunha, G. Bilger, A. Strohm, M. Kaelin, H. Zogg, and A. N. Tiwari, "Sodium incorporation strategies for CIGS growth at different temperatures," *Thin Solid Films*, vol. 480, pp. 55–60, 2005.
- [41] P. Salomé, V. Fjällström, A. Hultqvist, and M. Edoff, "Na doping of CIGS solar cells using low sodium-doped Mo layer," *IEEE J. Photovoltaics*, vol. 3, no. 1, pp. 509–513, 2012.
- [42] K. Granath, M. Bodegård, and L. Stolt, "The effect of NaF on Cu(In,Ga)Se₂ thin film solar cells," *Sol. energy Mater. Sol. cells*, vol. 60, no. 3, pp. 279–293, 2000.
- [43] P. S. Vasekar and N. G. Dhere, "Effect of sodium addition on Cu-deficient CuIn_{1-x}Ga_xS₂ thin film solar cells," *Sol. energy Mater. Sol. cells*, vol. 93, no. 1, pp. 69–73, 2009.
- [44] P. Jackson, R. Wuerz, D. Hariskos, E. Lotter, W. Witte, and M. Powalla, "Effects of heavy alkali elements in Cu(In,Ga)Se₂ solar cells with efficiencies up to 22.6%," *physica status solidi (RRL)-Rapid Research Letters*, vol. 10, no. 8, pp. 583–586, 2016.
- [45] J. Chantana, D. Hironiwa, T. Watanabe, S. Teraji, and T. Minemoto, "Flexible Cu(In,Ga)Se₂ solar cell on stainless steel substrate deposited by multi-layer precursor method: its photovoltaic performance and deep-level defects," *Progress in Photovoltaics: Research and Applications*, 2016.
- [46] J. Trieschmann, S. Ries, N. Bibinov, P. Awakowicz, S. Mráz, J. M. Schneider, and T. Mussenbrock, "Combined experimental and theoretical description of direct current magnetron sputtering of Al by Ar and Ar/N₂ plasma," *Plasma Sources Science and Technology*, vol. 27, no. 5, p. 54 003, 2018.
- [47] K. Orgassa, H. W. Schock, and J. H. Werner, "Alternative back contact materials for thin film Cu(In,Ga)Se₂ solar cells," *Thin Solid Films*, vol. 431, pp. 387–391, 2003.
- [48] J.-H. Yoon, K.-H. Yoon, W. M. Kim, J.-K. Park, Y.-J. Baik, T.-Y. Seong, and J.-h. Jeong, "High-temperature stability of molybdenum (Mo) back contacts for CIGS solar cells: a route towards more robust back contacts," *Journal of Physics D: Applied Physics*, vol. 44, no. 42, p. 425 302, 2011.
- [49] J. Yoon, T. Seong, and J. Jeong, "Effect of a Mo back contact on Na diffusion in CIGS thin film solar cells," *Progress in Photovoltaics: Research and Applications*, vol. 21, no. 1, pp. 58–63, 2013.
- [50] L. Gouillart, A. Cattoni, J. Goffard, F. Donsanti, G. Patriarche, M. Jubault, N. Naghavi, and S. Collin, "Development of reflective back contacts for high-efficiency ultrathin Cu(In,Ga)Se₂ solar cells," *Thin Solid Films*, vol. 672, no. July 2018, pp. 1–6, 2019.
- [51] O. Dalstein, D. R. Ceratti, C. Boissière, D. Grosso, A. Cattoni, and M. Faustini, "Nanoimprinted, Submicrometric, MOF-Based 2D Photonic Structures: Toward Easy Selective Vapors Sensing by a Smartphone Camera," *Advanced Functional Materials*, vol. 26, no. 1, pp. 81–90, 2016.

-
- [52] S. Siebentritt, "Alternative buffers for chalcopyrite solar cells," *Solar energy*, vol. 77, no. 6, pp. 767–775, 2004.
- [53] S. Lee, E. S. Lee, T. Y. Kim, J. S. Cho, Y. J. Eo, J. H. Yun, and A. Cho, "Effect of annealing treatment on CdS/CIGS thin film solar cells depending on different CdS deposition temperatures," *Solar Energy Materials and Solar Cells*, vol. 141, pp. 299–308, 2015.
- [54] D. Hariskos, S. Spiering, and M. Powalla, "Buffer layers in Cu(In,Ga)Se₂ solar cells and modules," *Thin solid films*, vol. 480, pp. 99–109, 2005.
- [55] S. Merdes, V. Malinen, F. Ziem, I. Laueremann, M. Schüle, F. Stober, F. Hergert, N. Papathanasiou, and R. Schlatmann, "Zn(O,S) buffer prepared by atomic layer deposition for sequentially grown Cu(In,Ga)(Se,S)₂ solar cells and modules," *Solar Energy Materials and Solar Cells*, vol. 126, pp. 120–124, 2014.
- [56] W. Witte, S. Spiering, and D. Hariskos, "Substitution of the cds buffer layer in cigs thin-film solar cells: Status of current research and record cell efficiencies," *Vakuum in Forschung und Praxis*, vol. 26, no. 1, pp. 23–27, 2014.
- [57] M. R. De Guire, L. P. Bauermann, H. Parikh, and J. Bill, "Chemical bath deposition," in *Chemical Solution Deposition of Functional Oxide Thin Films*, Springer, 2013, pp. 319–339.
- [58] F. Larsson, O. Donzel-Gargand, J. Keller, M. Edoff, and T. Törndahl, "Atomic layer deposition of Zn(O,S) buffer layers for Cu(In,Ga)Se₂ solar cells with KF post-deposition treatment," *Solar Energy Materials and Solar Cells*, vol. 183, no. March, pp. 8–15, 2018.
- [59] E. Fortunato, D. Ginley, H. Hosono, and D. C. Paine, "Transparent Conducting Oxides for Photovoltaics," *MRS Bulletin*, vol. 32, no. 3, pp. 242–247, 2007.
- [60] M. Theelen and F. Daume, "Stability of Cu(In,Ga)Se₂ solar cells: A literature review," *Solar Energy*, vol. 133, pp. 586–627, 2016.
- [61] M. Warasawa, A. Kaijo, and M. Sugiyama, "Advantages of using amorphous indium zinc oxide films for window layer in Cu(In,Ga)Se₂ solar cells," *Thin Solid Films*, vol. 520, no. 6, pp. 2119–2122, 2012.
- [62] T. Minami, "Transparent conducting oxide semiconductors for transparent electrodes," *Semiconductor Science and Technology*, vol. 20, no. 4, 2005.
- [63] T. Jäger, Y. E. Romanyuk, S. Nishiwaki, B. Bissig, F. Pianezzi, P. Fuchs, C. Gretener, M. Döbeli, and A. N. Tiwari, "Hydrogenated indium oxide window layers for high-efficiency Cu(In,Ga)Se₂ solar cells," *Journal of Applied Physics*, vol. 117, no. 20, pp. 1–8, 2015.
- [64] *MiaSolé*. [Online]. Available: <http://miasole.com/> (visited on 06/02/2020).
- [65] M. Pinarbasi, S. Aksu, J. Freitag, T. Boone, H. Zolla, J. Vasquez, D. Nayak, E. Lee, T. Wang, J. Abushama, and B. Metin, "Flexible cells and modules produced using roll-to-roll electroplating approach," *Conference Record of the IEEE Photovoltaic Specialists Conference*, pp. 169–174, 2010.

- [66] P. Reinhard, A. Chirila, P. Blosch, F. Pianezzi, S. Nishiwaki, S. Buecheler, and A. N. Tiwari, "Review of Progress Toward 20% Efficiency Flexible CIGS Solar Cells and Manufacturing Issues of Solar Modules," *IEEE Journal of Photovoltaics*, vol. 3, no. 1, pp. 572–580, Jan. 2013.
- [67] K. Ramanathan, M. A. Contreras, C. L. Perkins, S. Asher, F. S. Hasoon, J. Keane, D. Young, M. Romero, W. Metzger, and R. Noufi, "Properties of 19.2% efficiency ZnO/CdS/CuInGaSe₂ thin-film solar cells," *Progress in Photovoltaics: Research and Applications*, vol. 11, no. 4, pp. 225–230, 2003.
- [68] I. Repins, M. A. Contreras, B. Egaas, C. DeHart, J. Scharf, C. L. Perkins, B. To, and R. Noufi, "19.9%-efficient ZnO/CdS/CuInGaSe₂ solar cell with 81.2% fill factor," *Progress in Photovoltaics: Research and applications*, vol. 16, no. 3, pp. 235–239, 2008.
- [69] H. K. Raut, V. A. Ganesh, A. S. Nair, and S. Ramakrishna, "Anti-reflective coatings: A critical, in-depth review," *Energy & Environmental Science*, vol. 4, no. 10, pp. 3779–3804, 2011.
- [70] A. Čampa, J. Krč, J. Malmström, M. Edoff, F. Smole, and M. Topič, "The potential of textured front ZnO and flat TCO/metal back contact to improve optical absorption in thin Cu(In,Ga)Se₂ solar cells," *Thin Solid Films*, vol. 515, no. 15, pp. 5968–5972, 2007.
- [71] O. Isabella, R. Vismara, D. N. Linssen, K. X. Wang, S. Fan, and M. Zeman, "Advanced light trapping scheme in decoupled front and rear textured thin-film silicon solar cells," *Solar Energy*, vol. 162, no. January, pp. 344–356, 2018.
- [72] C. Onwudinanti, R. Vismara, O. Isabella, L. Grenet, F. Emieux, and M. Zeman, "Advanced light management based on periodic textures for Cu(In,Ga)Se₂ thin-film solar cells," *Optics Express*, vol. 24, no. 6, A693, 2016.
- [73] H. A. Atwater and A. Polman, "Plasmonics for improved photovoltaic devices," in *Materials For Sustainable Energy: A Collection of Peer-Reviewed Research and Review Articles from Nature Publishing Group*, World Scientific, 2011, pp. 1–11.
- [74] W. Ohm, W. Riedel, Ü. Askünger, M. D. Heinemann, C. A. Kaufmann, J. L. López-García, V. Izquierdo, X. Fontané, T. Goislard, M. C. Lux-Steiner, and S. Gledhill, "An overview of technological aspects of Cu(In,Ga)Se₂ solar cell architectures incorporating ZnO nanorod arrays," *Physica Status Solidi (A) Applications and Materials Science*, vol. 212, no. 1, pp. 76–87, 2015.
- [75] M. Schmid, "Review on light management by nanostructures in chalcopyrite solar cells," *Semiconductor Science and Technology*, vol. 32, no. 4, p. 43003, 2017.
- [76] S. Siebentritt, "What limits the efficiency of chalcopyrite solar cells?" *Solar Energy Materials and Solar Cells*, vol. 95, no. 6, pp. 1471–1476, 2011.

-
- [77] P. M. Salome, B. Vermang, R. Ribeiro-Andrade, J. P. Teixeira, J. M. Cunha, M. J. Mendes, S. Haque, J. Borme, H. Águas, E. Fortunato, *et al.*, "Passivation of interfaces in thin film solar cells: Understanding the effects of a nanostructured rear point contact layer," *Advanced Materials Interfaces*, vol. 5, no. 2, p. 1701101, 2018.
- [78] J. Melskens, B. W. Van De Loo, B. Macco, L. E. Black, S. Smit, and W. M. Kessels, "Passivating Contacts for Crystalline Silicon Solar Cells: From Concepts and Materials to Prospects," *IEEE Journal of Photovoltaics*, vol. 8, no. 2, pp. 373–388, 2018.
- [79] L. Mazzarella, S. Kirner, B. Stannowski, L. Korte, B. Rech, and R. Schlatmann, "P-type microcrystalline silicon oxide emitter for silicon heterojunction solar cells allowing current densities above 40 mA/cm²," *Applied Physics Letters*, vol. 106, no. 2, 2015.
- [80] B. Vermang, V. Fjällström, J. Pettersson, P. Salomé, and M. Edoff, "Development of rear surface passivated Cu(In,Ga)Se₂ thin film solar cells with nanosized local rear point contacts," *Solar Energy Materials and Solar Cells*, vol. 117, pp. 505–511, 2013.
- [81] B. Vermang, V. Fjällström, X. Gao, and M. Edoff, "Improved Rear Surface Passivation of Cu(In,Ga)Se₂ Solar Cells: A Combination of an Al₂O₃ Rear Surface Passivation Layer and Nanosized Local Rear Point Contacts," *IEEE Journal of Photovoltaics*, vol. 4, no. 1, pp. 486–492, 2014.
- [82] B. Vermang, J. T. Wätjen, V. Fjällström, F. Rostvall, M. Edoff, R. Gunnarsson, I. Pilch, U. Helmersson, R. Kotipalli, F. Henry, and D. Flandre, "Highly reflective rear surface passivation design for ultra-thin Cu(In,Ga)Se₂ solar cells," *Thin Solid Films*, vol. 582, pp. 300–303, 2015.
- [83] S. Suresh, J. de Wild, T. Kohl, D. G. Buldu, G. Brammertz, M. Meuris, J. Poortmans, O. Isabella, M. Zeman, and B. Vermang, "A study to improve light confinement and rear-surface passivation in a thin-Cu(In,Ga)Se₂ solar cell," *Thin Solid Films*, vol. 669, no. July 2018, pp. 399–403, 2019.
- [84] P. Casper, R. Hünig, G. Gomard, O. Kiowski, C. Reitz, U. Lemmer, M. Powalla, and M. Hetterich, "Optoelectrical improvement of ultra-thin Cu(In,Ga)Se₂ solar cells through microstructured MgF₂ and Al₂O₂ back contact passivation layer," *physica status solidi (RRL)-Rapid Research Letters*, vol. 10, no. 5, pp. 376–380, 2016.
- [85] T.-H. Cheng, W. Hsu, C. Huang, J.-A. Lu, J. Chen, and C. Liu, "Photoluminescence characterization and passivation of cigs absorber," *ECS Transactions*, vol. 33, no. 17, p. 191, 2011.
- [86] F. Mollica, J. Goffard, M. Jubault, F. Donsanti, S. Collin, A. Cattoni, L. Lombez, N. Naghavi, R. Edf, I. Umr, and D. Renaissance, "Comparative study of patterned TiO₂ and Al₂O₂ layers as passivated back-contact for ultra-thin Cu(In,Ga)Se₂ solar cells," in *Photovoltaic Specialists Conference (PVSC), 2016 IEEE 43rd*, IEEE, 2016, pp. 6–10.

- [87] B. Vermang, J. T. Wätjen, V. Fjällström, F. Rostvall, M. Edoff, R. Kotipalli, F. Henry, and D. Flandre, "Employing Si solar cell technology to increase efficiency of ultra-thin Cu(In,Ga)Se₂ solar cells," *Progress in Photovoltaics: Research and Applications*, vol. 22, no. 10, pp. 1023–1029, 2014.
- [88] NREL, *Reference solar spectral irradiance: air mass 1.5*. [Online]. Available: <https://www.nrel.gov/grid/solar-resource/spectra.html> (visited on 06/02/2020).
- [89] W. Shockley and H. J. Queisser, "Detailed balance limit of efficiency of p-n junction solar cells," *Journal of Applied Physics*, vol. 32, no. 3, pp. 510–519, 1961.
- [90] M. Topic, R. M. Geisthardt, and J. R. Sites, "Performance limits and status of single-junction solar cells with emphasis on CIGS," *IEEE Journal of Photovoltaics*, vol. 5, no. 1, pp. 360–365, 2015.
- [91] A. Richter, M. Hermle, and S. W. Glunz, "Reassessment of the limiting efficiency for crystalline silicon solar cells," *IEEE Journal of Photovoltaics*, vol. 3, no. 4, pp. 1184–1191, 2013.
- [92] T. Tiedje, E. Yablonovitch, G. Cody, and B. Brooks, "Limiting efficiency of silicon solar cells," *IEEE Transactions on Electron Devices*, vol. 31, no. 5, pp. 711–716, 1984.
- [93] E. Yablonovitch and G. Cody, "Intensity enhancement in textured optical sheets for solar cells," *IEEE Transactions on Electron Devices*, vol. 29, no. 2, pp. 300–305, Feb. 1982.
- [94] M. A. Green, "Lambertian light trapping in textured solar cells and light-emitting diodes: Analytical solutions," *progress in Photovoltaics: Research and Applications*, vol. 10, no. 4, pp. 235–241, 2002.
- [95] M. Elbar, S. Tobbeche, and A. Merazga, "Effect of top-cell CGS thickness on the performance of CGS/CIGS tandem solar cell," *Solar Energy*, vol. 122, pp. 104–112, 2015.
- [96] A. Taflove and S. C. Hagness, *Computational electrodynamics: the finite-difference time-domain method*. Artech house, 2005.
- [97] J. Kupec and B. Witzigmann, "Computational electromagnetics for nanowire solar cells," *Journal of Computational Electronics*, vol. 11, no. 2, pp. 153–165, 2012.
- [98] R. J. Luebbers and F. Hunsberger, "FDTD for N th-order dispersive media," *IEEE transactions on Antennas and Propagation*, vol. 40, no. 11, pp. 1297–1301, 1992.
- [99] Z. Yang, J. Wang, Z. Cheng, H. Yin, W. Wang, Y. Huang, and X. Ren, "Reducing light reflection of CIGS solar cells with SiO₂ sandwiched by a metal nanoparticle structure," *OSA Continuum*, vol. 1, no. 4, p. 1313, 2018.
- [100] K. G. Ong, O. K. Varghese, G. K. Mor, K. Shankar, and C. A. Grimes, "Application of finite-difference time domain to dye-sensitized solar cells: The effect of nanotube-array negative electrode dimensions on light absorption," *Solar Energy Materials and Solar Cells*, vol. 91, no. 4, pp. 250–257, 2007.

-
- [101] R. Dewan and D. Knipp, "Light trapping in thin-film silicon solar cells with integrated diffraction grating," *Journal of Applied Physics*, vol. 106, no. 7, 2009.
- [102] J. Lacombe, O. Sergeev, K. Chakanga, K. Von Maydell, and C. Agert, "Three dimensional optical modeling of amorphous silicon thin film solar cells using the finite-difference time-domain method including real randomly surface topographies," *Journal of Applied Physics*, vol. 110, no. 2, 2011.
- [103] M. Moharam and T. Gaylord, "Rigorous coupled-wave analysis of planar-grating diffraction," *JOSA*, vol. 71, no. 7, pp. 811–818, 1981.
- [104] O. Isabella, S. Solntsev, D. Caratelli, and M. Zeman, "3-D optical modeling of thin-film silicon solar cells on diffraction gratings," *Progress in Photovoltaics: Research and Applications*, vol. 21, no. 1, pp. 94–108, 2013.
- [105] Y.-J. Lee, D. S. Ruby, D. W. Peters, B. B. McKenzie, and J. W. P. Hsu, "ZnO nanostructures as efficient antireflection layers in solar cells," *Nano letters*, vol. 8, no. 5, pp. 1501–1505, 2008.
- [106] L. Zhao, Y. H. Zuo, C. L. Zhou, H. L. Li, H. W. Diao, and W. J. Wang, "A highly efficient light-trapping structure for thin-film silicon solar cells," *Solar energy*, vol. 84, no. 1, pp. 110–115, 2010.
- [107] T. Weiland, "A discretization model for the solution of Maxwell's equations for six-component fields," *Archiv Elektronik und Uebertragungstechnik*, vol. 31, pp. 116–120, 1977.
- [108] B. Krietenstein, R. Schuhmann, P. Thoma, T. Weiland, and D. Darmstadt, "the Perfect Boundary Approximation Technique Facing the Big Challenge of High Precision Field Computation," *Microwave Theory and Techniques, IEEE Transactions on*, vol. 52, no. 8, pp. 860–862, 1983.
- [109] H. Stiebig, C. Haase, C. Zahren, B. Rech, and N. Senoussaoui, "Thin-film silicon solar cells with grating couplers - An experimental and numerical study," *Journal of Non-Crystalline Solids*, vol. 352, no. 9-20 SPEC. ISS. Pp. 1949–1952, 2006.
- [110] C. Haase and H. Stiebig, "Optical properties of thin-film silicon solar cells with grating couplers," *Progress in Photovoltaics: Research and Applications*, vol. 14, no. 7, pp. 629–641, 2006.
- [111] Z. Rahimi and C. Pflaum, "Simulation of the scattering effect of randomly textured surfaces on the efficiency of thin film tandem solar cell," *Physics, Simulation, and Photonic Engineering of Photovoltaic Devices III*, vol. 8981, no. March 2014, 89811E, 2014.
- [112] C. C. Katsidis and D. I. Siapkas, "Systems With Coherent , Partially Coherent , and Incoherent Interference," *Applied Optics*, vol. 41, no. 19, pp. 3978–3987, 2002.
- [113] M. Topič, M. Sever, B. Lipovšek, A. Čampa, and J. Krč, "Approaches and challenges in optical modelling and simulation of thin-film solar cells," *Solar Energy Materials and Solar Cells*, vol. 135, pp. 57–66, 2015.

- [114] R. Siegel, "Net radiation method for transmission through partially transparent plates," *Solar Energy*, vol. 15, no. 3, pp. 273–276, 1973.
- [115] R. Santbergen, A. H. Smets, and M. Zeman, "Optical model for multilayer structures with coherent, partly coherent and incoherent layers," *Optics Express*, vol. 21, no. S2, A262, 2013.
- [116] R. Santbergen, T. Meguro, T. Suezaki, G. Koizumi, K. Yamamoto, and M. Zeman, "GenPro4 optical model for solar cell simulation and its application to multijunction solar cells," *IEEE Journal of Photovoltaics*, vol. 7, no. 3, pp. 919–926, 2017.
- [117] R. Courant, *Variational methods for the solution of problems of equilibrium and vibrations*. Verlag nicht ermittelbar, 1943.
- [118] J.-M. Jin, *The finite element method in electromagnetics*. John Wiley & Sons, 2014.
- [119] H. Shen, P. Bienstman, and B. Maes, "Plasmonic absorption enhancement in organic solar cells with thin active layers," *Journal of Applied Physics*, vol. 106, no. 7, 2009.
- [120] K. Ho-Le, "Finite element mesh generation methods: a review and classification," *Computer-aided design*, vol. 20, no. 1, pp. 27–38, 1988.
- [121] G. Yin, A. Steigert, P. Andrae, M. Goebelt, M. Latzel, P. Manley, I. Lauermann, S. Christiansen, and M. Schmid, "Integration of plasmonic Ag nanoparticles as a back reflector in ultra-thin Cu(In,Ga)Se₂ solar cells," *Applied Surface Science*, vol. 355, pp. 800–804, 2015.
- [122] G. Yin, P. Manley, and M. Schmid, "Light trapping in ultrathin CuIn_{1-x}Ga_xSe₂ solar cells by dielectric nanoparticles," *Solar Energy*, vol. 163, no. January, pp. 443–452, 2018.
- [123] M. Schmid, G. Yin, M. Song, S. Duan, B. Heidmann, D. Sancho-Martinez, S. Kämmer, T. Köhler, P. Manley, and M. C. Lux-Steiner, "Concentrating light in Cu(In,Ga)Se₂ solar cells," *Journal of Photonics for Energy*, vol. 7, no. 1, p. 018001, 2017.
- [124] J. van Deelen, A. Omar, and M. Barink, "Optical design of textured thin-film CIGS solar cells with nearly-invisible nanowire assisted front contacts," *Materials*, vol. 10, no. 4, p. 392, 2017.
- [125] N. Bednar, N. Severino, and N. Adamovic, "Front grid optimization of Cu(In,Ga)Se₂ solar cells using hybrid modeling approach," *Journal of Renewable and Sustainable Energy*, vol. 7, no. 1, 2015.
- [126] W. Wang, S. Wu, R. J. Knize, K. Reinhardt, Y. Lu, and S. Chen, "Enhanced photon absorption and carrier generation in nanowire solar cells," *Optics Express*, vol. 20, no. 4, p. 3733, 2012.
- [127] U. Malm and M. Edoff, "Simulating material inhomogeneities and defects in CIGS thin-film solar cells," *Progress in Photovoltaics: Research and Applications*, vol. 17, no. 5, pp. 306–314, 2009.

-
- [128] R. Vismara, C. Onwudinanti, L. Grenet, F. Emieux, O. Isabella, and M. Zeman, "Optical analysis of CIGS solar cells on periodic gratings," in *Optical Nanostructures and Advanced Materials for Photovoltaics*, Optical Society of America, 2015, PTu4B–5.
- [129] C. Simovski, D. Morits, P. Voroshilov, M. Guzha, P. Belov, and Y. Kivshar, "Enhanced efficiency of light-trapping nanoantenna arrays for thin-film solar cells," *Optics express*, vol. 21, no. 104, A714–A725, 2013.
- [130] K. Jäger, D. N. P. Linssen, O. Isabella, and M. Zeman, "Ambiguities in optical simulations of nanotextured thin-film solar cells using the finite-element method," *Optics Express*, vol. 23, no. 19, A1060–A1071, 2015.
- [131] ANSYS HFSS official website. [Online]. Available: <http://www.ansys.com/products/Electronics/ANSYS-HFSS> (visited on 06/02/2020).
- [132] ASA simulator website. [Online]. Available: <https://asa.ewi.tudelft.nl/> (visited on 06/02/2020).
- [133] D. Zhang, I. A. Digdaya, R. Santbergen, R. A. Van Swaaij, P. Bronsveld, M. Zeman, J. A. M. Van Roosmalen, and A. W. Weeber, "Design and fabrication of a SiO_x/ITO double-layer anti-reflective coating for heterojunction silicon solar cells," *Solar Energy Materials and Solar Cells*, vol. 117, pp. 132–138, 2013.
- [134] A. M. Dagamseh, B. Vet, P. Šutta, and M. Zeman, "Modelling and optimization of a-Si:H solar cells with ZnO:Al back reflector," *Solar Energy Materials and Solar Cells*, vol. 94, no. 12, pp. 2119–2123, 2010.
- [135] L. Han, I. A. Digdaya, T. W. Buijs, F. F. Abdi, Z. Huang, R. Liu, B. Dam, M. Zeman, W. A. Smith, and A. H. Smets, "Gradient dopant profiling and spectral utilization of monolithic thin-film silicon photoelectrochemical tandem devices for solar water splitting," *Journal of Materials Chemistry A*, vol. 3, no. 8, pp. 4155–4162, 2015.
- [136] M. Zeman, O. Isabella, S. Solntsev, and K. Jäger, "Modelling of thin-film silicon solar cells," *Solar Energy Materials and Solar Cells*, vol. 119, pp. 94–111, 2013.
- [137] P. Bras, C. Frisk, A. Tempez, E. Niemi, and C. Platzer-Björkman, "Ga-grading and Solar Cell Capacitance Simulation of an industrial Cu(In,Ga)Se₂ solar cell produced by an in-line vacuum, all-sputtering process," *Thin Solid Films*, vol. 636, pp. 367–374, 2017.
- [138] M. Burgelman, K. Decock, S. Khelifi, and A. Abass, "Advanced electrical simulation of thin film solar cells," *Thin Solid Films*, vol. 535, no. 1, pp. 296–301, 2013.
- [139] R. Kotipalli, B. Vermang, J. Joel, R. Rajkumar, M. Edoff, and D. Flandre, "Investigating the electronic properties of Al₂O₃ /Cu(In,Ga)Se₂ interface," *AIP Advances*, vol. 5, no. 10, p. 107101, 2015.
- [140] W. Hsu, C. M. Sutter-Fella, M. Hettick, L. Cheng, S. Chan, Y. Chen, Y. Zeng, M. Zheng, H.-P. Wang, and C.-C. Chiang, "Electron-Selective TiO₂ Contact for Cu(In,Ga)Se₂ Solar Cells," *Scientific reports*, vol. 5, 2015.

- [141] U. Rau and M. Schmidt, "Electronic properties of ZnO/CdS/Cu(In,Ga)Se₂ solar cells - Aspects of heterojunction formation," *Thin Solid Films*, vol. 387, no. 1-2, pp. 141–146, 2001.
- [142] S. Bose, J. M. Cunha, J. Borme, W. C. Chen, N. S. Nilsson, J. P. Teixeira, J. Gaspar, J. P. Leitão, M. Edoff, P. A. Fernandes, and P. M. Salomé, "A morphological and electronic study of ultrathin rear passivated Cu(In,Ga)Se₂ solar cells," *Thin Solid Films*, vol. 671, no. December 2018, pp. 77–84, 2019.
- [143] D. S. Chen, J. Yang, F. Xu, P. H. Zhou, H. W. Du, J. W. Shi, Z. S. Yu, Y. H. Zhang, B. Bartholomeusz, and Z. Q. Ma, "Effect of rapid thermal annealing on the compositional ratio and interface of Cu(In,Ga)Se₂ solar cells by XPS," *Applied Surface Science*, vol. 264, pp. 459–463, 2013.
- [144] J. Song, S. S. Li, C. H. Huang, O. D. Crisalle, and T. J. Anderson, "Device modeling and simulation of the performance of Cu(In_{1-x},Ga_x)Se₂ solar cells," *Solid-State Electronics*, vol. 48, no. 1, pp. 73–79, 2004.
- [145] M. Schmidt, L. Korte, A. Laades, R. Stangl, C. Schubert, H. Angermann, E. Conrad, and K. v. Maydell, "Physical aspects of a-Si:H/c-Si hetero-junction solar cells," *Thin Solid Films*, vol. 515, no. 19 SPEC. ISS. Pp. 7475–7480, 2007.
- [146] *Silvaco official website*. [Online]. Available: <https://www.silvaco.com/> (visited on 06/02/2020).
- [147] J. M. Delgado-Sanchez, J. M. López-González, A. Orpella, E. Sánchez-Cortezon, M. D. Alba, C. López-López, and R. Alcubilla, "Front contact optimization of industrial scale CIGS solar cells for low solar concentration using 2D physical modeling," *Renewable Energy*, vol. 101, pp. 90–95, 2017.
- [148] S. Sharbati, S. H. Keshmiri, J. T. McGoffin, and R. Geisthardt, "Improvement of CIGS thin-film solar cell performance by optimization of Zn(O,S) buffer layer parameters," *Applied Physics A: Materials Science and Processing*, vol. 118, no. 4, pp. 1259–1265, 2014.
- [149] *Quokka3 official website*. [Online]. Available: <http://quokka3.com/Features.html> (visited on 06/02/2020).
- [150] E. Franklin, K. Fong, K. McIntosh, A. Fell, A. Blakers, T. Kho, D. Walter, D. Wang, N. Zin, M. Stocks, E.-C. Wang, N. Grant, Y. Wan, Y. Yang, X. Zhang, Z. Feng, and P. J. Verlinden, "Design, fabrication and characterisation of a 24.4% efficient interdigitated back contact solar cell," *Progress in Photovoltaics: Research and Applications*, vol. 24, no. 4, pp. 411–427, Apr. 2016.
- [151] *Synopsys official website*. [Online]. Available: <https://www.synopsys.com/> (visited on 06/02/2020).
- [152] Synopsys, *Sentaurus Device User*, September. 2014.
- [153] G. Sozzi, R. Menozzi, N. Cavallari, M. Bronzoni, F. Annoni, M. Calicchio, and M. Mazzer, "On the temperature behavior of shunt-leakage currents in Cu(In,Ga)Se₂ solar cells: The role of grain boundaries and rear Schottky contact," *2015 IEEE 42nd Photovoltaic Specialist Conference, PVSC 2015*, 2015.

-
- [154] G. Sozzi, S. Di Napoli, R. Menozzi, R. Carron, E. Avancini, B. Bissig, S. Buecheler, and A. N. Tiwari, "Analysis of Ga grading in CIGS absorbers with different Cu content," *2017 IEEE 44th Photovoltaic Specialist Conference, PVSC 2017*, pp. 1–4, 2018.
- [155] W. K. Metzger, I. L. Repins, M. Romero, P. Dippo, M. Contreras, R. Noufi, and D. Levi, "Recombination kinetics and stability in polycrystalline Cu(In,Ga)Se₂ solar cells," *Thin Solid Films*, vol. 517, no. 7, pp. 2360–2364, 2009.
- [156] N. Rezaei, O. Isabella, Z. Vroon, and M. Zeman, "Quenching Mo optical losses in CIGS solar cells by a point contacted dual-layer dielectric spacer: a 3-D optical study," *Optics Express*, vol. 26, no. 2, A39, Jan. 2018.
- [157] D. Herrmann, P. Kratzert, S. Weeke, M. Zimmer, J. Djordjevic-Reiss, R. Hunger, P. Lindberg, E. Wallin, O. Lundberg, and L. Stolt, "CIGS module manufacturing with high deposition rates and efficiencies," in *2014 IEEE 40th Photovoltaic Specialist Conference (PVSC)*, IEEE, 2014, pp. 2775–2777.
- [158] C. van Lare, G. Yin, A. Polman, and M. Schmid, "Light coupling and trapping in ultrathin Cu(In,Ga)Se₂ solar cells using dielectric scattering patterns," *ACS nano*, vol. 9, no. 10, pp. 9603–9613, 2015.
- [159] J. Pettersson, T. Törndahl, C. Platzer-Björkman, A. Hultqvist, and M. Edoff, "The Influence of Absorber Thickness on Cu(In,Ga)Se₂ Solar Cells With Different Buffer Layers," *IEEE Journal of Photovoltaics*, vol. 3, no. 4, pp. 1376–1382, 2013.
- [160] Z. Jehl, F. Erfurth, N. Naghavi, L. Lombez, I. Gerard, M. Bouttemy, P. Tran-Van, A. Etcheberry, G. Voorwinden, and B. Dimmler, "Thinning of CIGS solar cells: Part II: Cell characterizations," *Thin solid films*, vol. 519, no. 21, pp. 7212–7215, 2011.
- [161] E. Jarzembowski, M. Maiberg, F. Oberegner, K. Kaufmann, S. Krause, and R. Scheer, "Optical and electrical characterization of Cu(In,Ga)Se₂ thin film solar cells with varied absorber layer thickness," *Thin Solid Films*, vol. 576, pp. 75–80, 2015.
- [162] T. Hara, T. Maekawa, S. Minoura, Y. Sago, S. Niki, and H. Fujiwara, "Quantitative assessment of optical gain and loss in submicron-textured CuIn_{1-x}Ga_xSe₂ solar cells fabricated by three-stage coevaporation," *Physical Review Applied*, vol. 2, no. 3, p. 34 012, 2014.
- [163] Z. C. Holman, A. Descoeurdes, S. De Wolf, and C. Ballif, "Record infrared internal quantum efficiency in silicon heterojunction solar cells with dielectric/metal rear reflectors," *IEEE Journal of Photovoltaics*, vol. 3, no. 4, pp. 1243–1249, 2013.
- [164] V. Demontis, C. Sanna, J. Melskens, R. Santbergen, A. H. Smets, A. Damiano, and M. Zeman, "The role of oxide interlayers in back reflector configurations for amorphous silicon solar cells," *Journal of Applied Physics*, vol. 113, no. 6, p. 64 508, 2013.

- [165] Z. C. Holman, S. De Wolf, and C. Ballif, "Improving metal reflectors by suppressing surface plasmon polaritons: a priori calculation of the internal reflectance of a solar cell," *Light: Science & Applications*, vol. 2, no. 10, e106, 2013.
- [166] B. Vermang, J. T. Wätjen, C. Frisk, V. Fjällström, F. Rostvall, M. Edoff, P. Salomé, J. Borme, N. Nicoara, and S. Sadewasser, "Introduction of Si PERC Rear Contacting Design to Boost Efficiency of Cu(In,Ga)Se₂ Solar Cells," *IEEE Journal of Photovoltaics*, vol. 4, no. 6, pp. 1644–1649, 2014.
- [167] M. Burghoorn, B. Kniknie, J. van Deelen, M. Xu, Z. Vroon, R. van Ee, R. van de Belt, and P. Buskens, "Improving the efficiency of copper indium gallium (Di-) selenide (CIGS) solar cells through integration of a moth-eye textured resist with a refractive index similar to aluminum doped zinc oxide," *AIP Advances*, vol. 4, no. 12, p. 127154, 2014.
- [168] O. Lundberg, M. Bodegård, J. Malmström, and L. Stolt, "Influence of the Cu(In,Ga)Se₂ thickness and Ga grading on solar cell performance," *Progress in Photovoltaics: Research and Applications*, vol. 11, no. 2, pp. 77–88, Mar. 2003.
- [169] H. Raether, *Surface plasmons on smooth surfaces*. Springer, 1988.
- [170] S. A. Maier, *Plasmonics: fundamentals and applications*. Springer Science & Business Media, 2007.
- [171] L. Novotny and B. Hecht, *Principles of nano-optics*. Cambridge university press, 2012.
- [172] F. J. Haug, T. Söderström, O. Cubero, V. Terrazoni-Daudrix, and C. Ballif, "Influence of the ZnO buffer on the guided mode structure in Si/ZnO/Ag multilayers," *Journal of Applied Physics*, vol. 106, no. 4, p. 44502, 2009.
- [173] J.-H. Yoon, S. Cho, W. M. Kim, J.-K. Park, Y.-J. Baik, T. S. Lee, T.-Y. Seong, and J.-h. Jeong, "Optical analysis of the microstructure of a Mo back contact for Cu(In,Ga)Se₂ solar cells and its effects on Mo film properties and Na diffusivity," *Solar Energy Materials and Solar Cells*, vol. 95, no. 11, pp. 2959–2964, 2011.
- [174] R. Santbergen, H. Tan, M. Zeman, and A. H. M. Smets, "Enhancing the driving field for plasmonic nanoparticles in thin-film solar cells," *Optics express*, vol. 22, no. 104, A1023–A1028, 2014.
- [175] G. Dingemans and W. M. M. Kessels, "Status and prospects of Al₂O₃ -based surface passivation schemes for silicon solar cells," *Journal of Vacuum Science & Technology A: Vacuum, Surfaces, and Films*, vol. 30, no. 4, p. 040802, 2012.
- [176] M. J. Dodge, "Refractive properties of magnesium fluoride," *Applied Optics*, vol. 23, no. 12, pp. 1980–1985, 1984.
- [177] Z. C. Holman, M. Filipič, A. Descoedres, S. De Wolf, F. Smole, M. Topič, and C. Ballif, "Infrared light management in high-efficiency silicon heterojunction and rear-passivated solar cells," *Journal of Applied Physics*, vol. 113, no. 1, p. 13107, 2013.

-
- [178] F. J. Haug, T. Söderström, O. Cubero, V. Terrazoni-Daudrix, and C. Ballif, "Plasmonic absorption in textured silver back reflectors of thin film solar cells," *Journal of Applied Physics*, vol. 104, no. 6, p. 64509, 2008.
- [179] G. Brown, V. Faifer, A. Pudov, S. Anikeev, E. Bykov, M. Contreras, and J. Wu, "Determination of the minority carrier diffusion length in compositionally graded Cu(In,Ga)S₂ solar cells using electron beam induced current," *Applied Physics Letters*, vol. 96, no. 2, p. 22104, 2010.
- [180] O. Isabella, *Light management in thin-film silicon solar cells*. TU Delft, Delft University of Technology, 2013.
- [181] N. Rezaei, O. Isabella, Z. Vroon, and M. Zeman, "Optical optimization of a multi-layer wideband anti-reflection coating using porous MgF₂ for sub-micron-thick CIGS solar cells," *Solar Energy*, vol. 177, no. August 2018, pp. 59–67, 2019.
- [182] J. H. Werner, J. Mattheis, and U. Rau, "Efficiency limitations of polycrystalline thin film solar cells: case of Cu(In,Ga)Se₂," *Thin Solid Films*, vol. 480, pp. 399–409, 2005.
- [183] H. A. Macleod, *Thin-film optical filters*. CRC press, 2017.
- [184] A. Chirilă, P. Reinhard, F. Pianezzi, P. Bloesch, A. R. Uhl, C. Fella, L. Kranz, D. Keller, C. Gretener, and H. Hagendorfer, "Potassium-induced surface modification of Cu(In,Ga)Se₂ thin films for high-efficiency solar cells," *Nature Materials*, vol. 12, no. 12, pp. 1107–1111, 2013.
- [185] P. Jackson, D. Hariskos, R. Wuerz, W. Wischmann, and M. Powalla, "Compositional investigation of potassium doped Cu(In,Ga)Se₂ solar cells with efficiencies up to 20.8%," *physica status solidi (RRL)–Rapid Research Letters*, vol. 8, no. 3, pp. 219–222, 2014.
- [186] S. Mertin, L. Marot, C. S. Sandu, R. Steiner, J. L. Scartezzini, and P. Murralt, "Nanocrystalline Low-Refractive Magnesium Fluoride Films Deposited by Reactive Magnetron Sputtering: Optical and Structural Properties," *Advanced Engineering Materials*, vol. 17, no. 11, pp. 1652–1659, 2015.
- [187] J. D. Bass, C. Boissiere, L. Nicole, D. Grosso, and C. Sanchez, "Thermally Induced Porosity in CSD MgF₂-Based Optical Coatings: An Easy Method to Tune the Refractive Index," *Chemistry of Materials*, vol. 20, no. 17, pp. 5550–5556, Sep. 2008.
- [188] L. Rayleigh, "On reflection of vibrations at the confines of two media between which the transition is gradual," *Proceedings of the London Mathematical Society*, vol. 1, no. 1, pp. 51–56, 1879.
- [189] A. Ingenito, O. Isabella, and M. Zeman, "Nano-cones on micro-pyramids : modulated surface textures for maximal spectral response and high- efficiency solar cells," no. February, pp. 1649–1659, 2015.
- [190] N. Dahan, Z. Jehl, T. Hildebrandt, J.-J. Greffet, J.-F. Guillemoles, D. Lincot, and N. Naghavi, "Optical approaches to improve the photocurrent generation in Cu(In,Ga)Se₂ solar cells with absorber thicknesses down to 0.5 μm," *Journal of Applied Physics*, vol. 112, no. 9, p. 94902, 2012.

- [191] A. Han, Y. Zhang, W. Song, B. Li, W. Liu, and Y. Sun, "Structure, morphology and properties of thinned Cu(In,Ga)Se₂ films and solar cells," *Semiconductor Science and Technology*, vol. 27, no. 3, p. 35 022, 2012.
- [192] K. Shimazaki, M. Imaizumi, and K. Kibe, "SiO₂ and Al₂O₃/SiO₂ coatings for increasing emissivity of Cu(In,Ga)Se₂ thin-film solar cells for space applications," *Thin Solid Films*, vol. 516, no. 8, pp. 2218–2224, 2008.
- [193] S. Strehlke, S. Bastide, J. Guillet, and C. Levy-Clement, "Design of porous silicon antireflection coatings for silicon solar cells," *Materials Science and Engineering: B*, vol. 69, pp. 81–86, 2000.
- [194] C. Ballif, J. Dicker, D. Borchert, and T. Hofmann, "Solar glass with industrial porous SiO₂ antireflection coating: measurements of photovoltaic module properties improvement and modelling of yearly energy yield gain," *Solar energy materials and solar cells*, vol. 82, no. 3, pp. 331–344, 2004.
- [195] H. K. Raut, A. S. Nair, S. S. Dinachali, V. A. Ganesh, T. M. Walsh, and S. Ramakrishna, "Porous SiO₂ anti-reflective coatings on large-area substrates by electrospinning and their application to solar modules," *Solar Energy Materials and Solar Cells*, vol. 111, pp. 9–15, 2013.
- [196] A. Dabirian, M. Morales-Masis, F.-J. Haug, S. De Wolf, and C. Ballif, "Optical Evaluation of the Rear Contacts of Crystalline Silicon Solar Cells by Coupled Electromagnetic and Statistical Ray-Optics Modeling," *IEEE Journal of Photovoltaics*, vol. 7, no. 3, pp. 718–726, 2017.
- [197] D. Karthik, S. Pendse, S. Sakthivel, E. Ramasamy, and S. V. Joshi, "High performance broad band antireflective coatings using a facile synthesis of ink-bottle mesoporous MgF₂ nanoparticles for solar applications," *Solar Energy Materials and Solar Cells*, vol. 159, pp. 204–211, 2017.
- [198] D. Grosso, C. Boissière, and C. Sanchez, "Ultralow-dielectric-constant optical thin films built from magnesium oxyfluoride vesicle-like hollow nanoparticles," *Nature Materials*, vol. 6, no. 8, p. 572, 2007.
- [199] V. D. A. G. Bruggeman, "Berechnung verschiedener physikalischer Konstanten von heterogenen Substanzen. I. Dielektrizitätskonstanten und Leitfähigkeiten der Mischkörper aus isotropen Substanzen," *Annalen der physik*, vol. 416, no. 7, pp. 636–664, 1935.
- [200] K. O. Hara, Y. Nakagawa, T. Suemasu, and N. Usami, "Simple vacuum evaporation route to BaSi₂ thin films for solar cell applications," *Procedia Engineering*, vol. 141, pp. 27–31, 2016.
- [201] M. Kumar, N. Umezawa, and M. Imai, "BaSi₂ as a promising low-cost, earth-abundant material with large optical activity for thin-film solar cells: A hybrid density functional study," *Applied Physics Express*, vol. 7, no. 7, p. 71 203, 2014.
- [202] L. Mazzarella, M. Werth, K. Jäger, M. Jošt, L. Korte, S. Albrecht, R. Schlattmann, and B. Stannowski, "Infrared photocurrent management in monolithic perovskite/silicon heterojunction tandem solar cells by using a nanocrystalline silicon oxide interlayer," *Optics express*, vol. 26, no. 10, A487–A497, 2018.

-
- [203] A. Čampa, A. Valla, K. Brecl, F. Smole, D. Munoz, and M. Topič, "Multiscale Modeling and Back Contact Design of Bifacial Silicon Heterojunction Solar Cells," *IEEE Journal of Photovoltaics*, vol. 8, no. 1, pp. 89–95, 2018.
- [204] T. K. Chong, T. P. White, and K. Weber, "Optical Modelling of MAE textured Nanoporous Silicon," in *Optical Nanostructures and Advanced Materials for Photovoltaics*, Optical Society of America, 2014, PTu2C–6.
- [205] N. Tucher, O. Höhn, J. Christoph Goldschmidt, B. Bläsi, R. Cariou, J. Benick, F. Feldmann, O. Höhn, H. Hauser, P. Beutel, N. Razek, M. Wimplinger, B. Bläsi, D. Lackner, M. Hermle, G. Siefer, S. W. Glunz, A. W. Bett, F. Dimroth, K. A. Bush, A. F. Palmstrom, Z. J. Yu, M. Boccard, R. Cheacharoen, J. P. Mailoa, D. P. McMeekin, R. L. Z Hoyer, C. D. Bailie, T. Leijtens, I. M. Peters, M. C. Minichetti, N. Rolston, R. Prasanna, S. Sofia, D. Harwood, W. Ma, F. Moghadam, H. J. Snaith, T. Buonassisi, Z. C. Holman, S. F. Bent, M. D. McGehee, J. C. Goldschmidt, and B. Bläsi, "Optical modeling of structured silicon-based tandem solar cells and module stacks," *Optics Express*, vol. 26, no. 18, A761–A768, 2018.
- [206] E. V. Astrova and V. A. Tolmachev, "Effective refractive index and composition of oxidized porous silicon films," *Materials Science and Engineering: B*, vol. 69–70, no. Supplement C, pp. 142–148, 2000.
- [207] ANSYS Electromagnetics Suite 17.0, *ANSYS ELECTRONICS DESKTOP ONLINE HELP*.
- [208] H. Savin, P. Repo, G. Von Gastrow, P. Ortega, E. Calle, M. Garín, and R. Alcubilla, "Black silicon solar cells with interdigitated back-contacts achieve 22.1% efficiency," *Nature Nanotechnology*, vol. 10, no. 7, pp. 624–628, 2015.
- [209] N. Rezaei, O. Isabella, P. Procel, Z. Vroon, and M. Zeman, "Optical study of back-contacted CIGS solar cells," *Optics Express*, vol. 27, no. 8, A269, 2019.
- [210] R. Kaczynski, J. Lee, J. v. Alsborg, B. Sang, U. Schoop, and J. Britt, "In-line Potassium Fluoride Treatment of CIGS Absorbers Deposited on Flexible Substrates in a Production-Scale Process Tool," *Ieee Pvsoc*, pp. 1455–1458, 2017.
- [211] M. D. Lammert and R. J. Schwartz, "The interdigitated back contact solar cell: a silicon solar cell for use in concentrated sunlight," *IEEE Transactions on Electron Devices*, vol. 24, no. 4, pp. 337–342, 1977.
- [212] P. Procel, A. Ingenito, R. De Rose, S. Pierro, F. Crupi, M. Lanuzza, G. Corullo, O. Isabella, and M. Zeman, "Opto-electrical modelling and optimization study of a novel IBC c-Si solar cell," *Progress in Photovoltaics: Research and Applications*, vol. 25, no. 6, pp. 452–469, Jun. 2017.
- [213] G. Yang, P. Guo, P. Procel, G. Limodio, A. Weeber, O. Isabella, and M. Zeman, "High-efficiency black IBC c-Si solar cells with poly-Si as carrier-selective passivating contacts," *Solar Energy Materials and Solar Cells*, vol. 186, pp. 9–13, 2018.

- [214] D. D. Smith, G. Reich, M. Baldrias, M. Reich, N. Boitnott, and G. Bunea, "Silicon solar cells with total area efficiency above 25%," in *Photovoltaic Specialists Conference (PVSC), 2016 IEEE 43rd*, IEEE, 2016, pp. 3351–3355.
- [215] P. Wagner, J.-C. Stang, M. Mews, A. B. Morales-Vilches, B. Stannowski, B. Stegemann, and L. Korte, "Interdigitated back contact silicon heterojunction solar cells: Towards an industrially applicable structuring method," in *AIP Conference Proceedings*, vol. 1999, 2018, p. 060 001.
- [216] A. Tomasi, B. Paviet-Salomon, Q. Jeangros, J. Haschke, G. Christmann, L. Barraud, A. Descoedres, J. P. Seif, S. Nicolay, M. Despeisse, S. De Wolf, and C. Ballif, "Simple processing of back-contacted silicon heterojunction solar cells using selective-area crystalline growth," *Nature Energy*, vol. 2, p. 17 062, Apr. 2017.
- [217] K. Yoshikawa, H. Kawasaki, W. Yoshida, T. Irie, K. Konishi, K. Nakano, T. Uto, D. Adachi, M. Kanematsu, H. Uzu, and K. Yamamoto, "Silicon heterojunction solar cell with interdigitated back contacts for a photoconversion efficiency over 26%," *Nature Energy*, vol. 2, p. 17 032, Mar. 2017.
- [218] F. Haase, C. Hollemann, S. Schäfer, A. Merkle, M. Rienäcker, J. Krügener, R. Brendel, and R. Peibst, "Laser contact openings for local poly-Si-metal contacts enabling 26.1%-efficient POLO-IBC solar cells," *Solar Energy Materials and Solar Cells*, vol. 186, pp. 184–193, 2018.
- [219] K. Masuko, M. Shigematsu, T. Hashiguchi, D. Fujishima, M. Kai, N. Yoshimura, T. Yamaguchi, Y. Ichihashi, T. Mishima, N. Matsubara, T. Yamanishi, T. Takahama, M. Taguchi, E. Maruyama, and S. Okamoto, "Achievement of more than 25% conversion efficiency with crystalline silicon heterojunction solar cell," *IEEE Journal of Photovoltaics*, vol. 4, no. 6, pp. 1433–1435, 2014.
- [220] J. Nakamura, N. Asano, T. Hieda, C. Okamoto, H. Katayama, and K. Nakamura, "Development of heterojunction back contact Si solar cells," *IEEE Journal of Photovoltaics*, vol. 4, no. 6, pp. 1491–1495, 2014.
- [221] H. Fujiwara and M. Kondo, "Effects of carrier concentration on the dielectric function of ZnO:Ga and In₂O₃:Sn studied by spectroscopic ellipsometry: Analysis of free-carrier and band-edge absorption," *Physical Review B - Condensed Matter and Materials Physics*, vol. 71, no. 7, pp. 1–10, 2005.
- [222] K. X. Wang, Z. Yu, V. Liu, Y. Cui, and S. Fan, "Absorption enhancement in ultrathin crystalline silicon solar cells with antireflection and light-trapping nanocone gratings," *Nano letters*, vol. 12, no. 3, pp. 1616–1619, 2012.
- [223] C. S. Schuster, A. Bozzola, L. C. Andreani, and T. F. Krauss, "How to assess light trapping structures versus a Lambertian Scatterer for solar cells?" *Optics Express*, vol. 22, no. S2, A542, 2014.
- [224] S. R. Thomas, C.-W. Chen, M. Date, Y.-C. Wang, H.-W. Tsai, Z. M. Wang, and Y.-L. Chueh, "Recent developments in the synthesis of nanostructured chalcopyrite materials and their applications: a review," *RSC Adv.*, vol. 6, no. 65, pp. 60 643–60 656, 2016.

-
- [225] C. H. Liu, C. H. Chen, S. Y. Chen, Y. T. Yen, W. C. Kuo, Y. K. Liao, J. Y. Juang, H. C. Kuo, C. H. Lai, L. J. Chen, and Y. L. Chueh, "Large scale single-crystal Cu(In,Ga)Se₂ nanotip arrays for high efficiency solar cell," *Nano Letters*, vol. 11, no. 10, pp. 4443–4448, 2011.
- [226] W. N. Shafarman, R. S. Huang, and S. H. Stephens, "Characterization of Cu(InGa)Se₂ solar cells using etched absorber layers," *Conference Record of the 2006 IEEE 4th World Conference on Photovoltaic Energy Conversion, WCPEC-4*, vol. 1, pp. 420–423, 2007.
- [227] R. Vismara, O. Isabella, A. Ingenito, F. T. Si, and M. Zeman, "Geometrical optimisation of core-shell nanowire array for enhanced absorption in thin crystalline silicon heterojunction solar cells," *Beilstein Journal of Nanotechnology*, no. to be published, 2019.
- [228] K. Ramanathan, R. Noufi, B. To, D. L. Young, R. Bhattacharya, M. A. Contreras, R. G. Dhere, and G. Teeter, "Processing and properties of sub-micron CIGS solar cells," *Conference Record of the 2006 IEEE 4th World Conference on Photovoltaic Energy Conversion, WCPEC-4*, vol. 1, pp. 380–383, 2006.
- [229] R. Kotipalli, O. Poncelet, G. Li, Y. Zeng, L. A. Francis, B. Vermang, and D. Flandre, "Addressing the impact of rear surface passivation mechanisms on ultra-thin Cu(In,Ga)Se₂ solar cell performances using SCAPS 1-D model," *Solar Energy*, vol. 157, no. September, pp. 603–613, 2017.
- [230] T. M. Friedlmeier, P. Jackson, A. Bauer, D. Hariskos, O. Kiowski, R. Menner, R. Wuerz, and M. Powalla, "High-efficiency Cu(In,Ga)Se₂ solar cells," *Thin Solid Films*, vol. 633, pp. 13–17, 2017.
- [231] D. D. Smith, P. J. Cousins, A. Masad, S. Westerberg, M. Defensor, R. Ilaw, T. Dennis, R. Daquin, N. Bergstrom, A. Leygo, X. Zhu, B. Meyers, B. Bourne, M. Shields, and D. Rose, "SunPower's Maxeon Gen III solar cell: High efficiency and energy yield," *Conference Record of the IEEE Photovoltaic Specialists Conference*, pp. 908–913, 2013.
- [232] H. Sivaramakrishnan Radhakrishnan, M. D. Uddin, M. Xu, J. Cho, M. Ghanam, I. Gordon, J. Szlufcik, and J. Poortmans, "A novel silicon heterojunction IBC process flow using partial etching of doped a-Si:H to switch from hole contact to electron contact in situ with efficiencies close to 23%," *Progress in Photovoltaics: Research and Applications*, vol. 27, no. 11, pp. 959–970, 2019.
- [233] H. Takagishi, H. Noge, K. Saito, and M. Kondo, "Fabrication of interdigitated back-contact silicon heterojunction solar cells on a 53 μm-thick crystalline silicon substrate by using the optimized inkjet printing method for etching mask formation," *Japanese Journal of Applied Physics*, vol. 56, no. 4, 2017.
- [234] P. Procel, G. Yang, O. Isabella, and M. Zeman, "Theoretical evaluation of contact stack for high efficiency IBC-SHJ solar cells," *Solar Energy Materials and Solar Cells*, vol. 186, no. May, pp. 66–77, 2018.

- [235] C. Frisk, C. Platzer-Björkman, J. Olsson, P. Szaniawski, J. T. Wätjen, V. Fjällström, P. Salomé, and M. Edoff, "Optimizing Ga-profiles for highly efficient Cu(In,Ga)Se₂ thin film solar cells in simple and complex defect models," *Journal of Physics D: Applied Physics*, vol. 47, no. 48, 2014.
- [236] P. G. Snyder, J. A. Woollam, S. A. Alterovitz, and B. Johs, "Modeling Al_xGa_{1-x}As optical constants as functions of composition," *Journal of Applied Physics*, vol. 68, no. 11, pp. 5925–5926, Dec. 1990.
- [237] T. M. Friedlmeier, P. Jackson, A. Bauer, D. Hariskos, O. Kiowski, R. Wuerz, and M. Powalla, "Improved photocurrent in Cu(In,Ga)Se₂ solar cells: from 20.8% to 21.7% efficiency with CdS buffer and 21.0% Cd-free," *IEEE Journal of Photovoltaics*, vol. 5, no. 5, pp. 1487–1491, 2015.
- [238] O. Isabella, H. Sai, M. Kondo, and M. Zeman, "Full-wave optoelectrical modeling of optimized flattened light-scattering substrate for high efficiency thin-film silicon solar cells," *Progress in Photovoltaics: Research and Applications*, vol. 22, no. 6, pp. 671–689, 2014.
- [239] M. Hermle, F. Granek, O. Schultz-Wittmann, and S. W. Glunz, "Shading effects in back-junction back-contacted silicon solar cells," *Conference Record of the IEEE Photovoltaic Specialists Conference*, pp. 10–13, 2008.
- [240] K. Nakada, t. Kobayashi, T. Shimoyama, and A. Yamada, "Analysis of growth mechanism in Ga-rich Cu(In,Ga)Se₂," in *36th European PV Solar Energy Conference and Exhibition*, 2019.
- [241] K. Kim, H. Park, W. K. Kim, G. M. Hanket, and W. N. Shafarman, "Effect of reduced Cu(InGa)(SeS)₂ thickness using three-step H₂Se/Ar/H₂S reaction of Cu-In-Ga metal precursor," *IEEE Journal of Photovoltaics*, vol. 3, no. 1, pp. 446–450, 2013.

Acknowledgements

January 2016 was the start of an extraordinary change in my life. I started a new life in the Netherlands. My passion for learning and working on a peaceful and sustainable topic brought me to Delft University of Technology. I owe this to the trust that my promoters Dr.ir. Olindo Isabella and Prof.dr. Miro Zeman put in me. Olindo helped me communicate my research results better, was eager to talk about different topics and was almost always available to consult. I can't forget our three and a half-hour discussion on a subsection of my first paper on a Friday afternoon. It was so rewarding! At a personal level, he introduced me to his family that made me feel less lonely in a new country. He also encouraged me to improve my time management skills. I'm still working on it. Miro's advice on different occasions made me look at the topic from a different perspective and try to make my points as clear as possible. He also generously lent me books from his library, of which I really liked "The history of the world in 100 objects".

I was lucky to be financially supported by TNO/Solliance. This opened a window of opportunity to attend CIGS review meetings, receive updates on ongoing projects on CIGS, meet new people in the field and occasionally, present my work. I should especially thank Dr. Zeger Vroon for facilitating my communication with TNO and supporting my work. I had helpful discussions with Dr. Mirjam Theelen, Hans Linden, Dr. Marcel Simor and Dr. Joop van Deelen.

My special thanks go to the graduation committee, Prof. Martina Schmid, Prof. Bart Vermang, Prof. Arthur Weeber, Prof. Marco Topič, Dr. Zeger Vroon, Prof.dr. Miro Zeman and Dr.ir. Olindo Isabella. I appreciate the time you spent on evaluating this thesis and providing me with helpful feedback.

Life in PVMD group has been very fruitful for me. I was lucky to have inspiring discussions with Johan Blanker, Robin Vismara, Dr. Fai Tong Si, Dr. Rudi Santbergen, Dr. Paul Procel Moya and Dr. Ravi Vasudevan. I especially thank Fai Tong for the \LaTeX template I have used for this thesis. It was an honor to work with Stefaan Heirman, Martijn Tijssen, Remko Koornneef, Dr. René van Swaaij, Prof.dr. Arno Smets, Prof.dr. Arthur Weeber, Dr. Hesam Ziar, Dr. Patrizio Manganiello, Dr. Hamed Ahmadpanahi, Dr. Dimitris Deligiannis, Dr. Martijn van Sebille, Dr. Luana Mazzarella, Dr. Guangtao Yang, Dr. Gianluca Limodio, Dr. Paula Perez Rodriguez, Thierry de Vrijer, Anna Rita Bento Montes, Juan Camilo Ortiz Lizcano, Dr. Engin Özkol, Dr. Daniele Scirè, Dr. Carlos Ruiz Tobon, Can Han, Andres Calcabrini, Yilei Tian, Klaas Bakker (special thanks for providing CIGS samples), Manvika Sing, Yifeng Zhao, Arturo Martinez, Yilong Zhou, Yuan Gao, Andrea Illiberi, Dr. Malte Vogt, Dr. Mirco Muttillio, Maarten Verkou and Dr. Zameer Ahmad. Many of my close friendships started as just-peers in PVMD group and gradually developed into deeper connections, especially with my officemates. Ravi and I, the American and the Iranian, the vegan and the non-vegetarian, became good friends. Dimitris always arrived late, but compensated the delay with enjoyable long company and engaging in philosophical conversations. Paul is always a wonderful friend and a patient teacher. I'm still waiting for Lord of the rings extended version movie day(s) with him. The office was never

boring with Thierry around. He always had new pictures and videos of Sam ready to bring fun to me. No one is safe from his jokes. Luana is a good friend of mine, with whom I shared many good memories from our spontaneous dinners and various conversations. I shared my frustrations and worries, as well as many happy moments with Rita, Andres, Robin and Paula. Their care and comfort is invaluable to me.

Brian Carlsen, Rosa Erlina Rosa Evasari and Sunil Suresh, it was a pleasure to work with you. I wish you all a successful career and a joyous life.

My friends from Iran have not only made good memories in Iran for me, but also continued to cheer me up in Delft. Zohreh, Hoda, Niloufar, Fatemeh, Omidreza, Samira, Alika and Arezou, thank you for everything. I also met many new friends outside work environment that enlightened my life and looked after me. You Guys are wonderful! Ghazaleh, Michele, Kimia, Amir, Nasibeh, Maisa, Luca, Valeria, Elisa, Samuele, Anarita, Carmine, Satoshi, Alferio, Emmanouela, Quirine, Sam, Anna, Chiara, Raffaele, Fabrizio, Margherita, Fatima, Erfan, Mike, Joelle and Toktam, I have shared lovely memories with you. Thank you for them.

The presence of my fiancé at my side has brought so much happiness to my life. Wladick, your love, support and encouragement helped me keep up and successfully finish my PhD. I love you and I cannot wait to continue our journey together.

The last but not least is the priceless love of my family in Iran. I can't find enough words to describe how blessed I have been to be born in this family. It was heartbreaking to be away from them and yet, my parents gave me their full support and endure the distance. My extended family's passion is beyond words too.

بابا و مامان خوبم، این دنیا با شما زیباست. مهربانی، از خودگذشتگی و دل‌گرمی شما بود که من رو تا اینجا رسوند. متشکرم که به من یاد دادید مستقل باشم، به خودم تکیه کنم، از پا ننشینم و مهم‌تر از همه اینکه زن و مرد برابرند. ممنونم برای اینکه برخلاف سنت‌ها به من آزادی دادید تا خودم تجربه کنم.

زهرا، محمدمین و نازنین عزیزم، شما بهترین خواهرها و برادر دنیایید. هنوز اولین روزهایی که به جمع کوچک ما اضافه شدید، اولین قدم‌هایی که برداشتید، اولین روزهایی که به مدرسه رفتید رو در ذهنم مرور می‌کنم و پر از شور و شادی می‌شم. شادی و موفقیت شما بزرگ‌ترین هدیه برای منه. همیشه خودتون باشید و به توانایی‌هاتون ایمان داشته باشید.

صبا وقت سحر بوی زلف یار می آورد	دل شوریده ما را به بو در کار می آورد
من آن شکل صنوبر را ز باغ دیده برکندم	که هر گل کز غمش بشکفت محنت بار می آورد
فروغ ماه می‌دیدم ز بام قصر او روشن	که رو از شرم آن خورشید در دیوار می آورد

List of Publications

Articles on peer-reviewed journals

1. **N. Rezaei**, P. Procel, M. Simor, Z. Vroon, M. Zeman and O. Isabella, "Interdigitated back-contacted structure: a different approach towards high efficiency ultra-thin CIGS solar cells," *Progress in Photovoltaics*, doi:10.1002/pip.3296, in production.
2. **N. Rezaei**, O. Isabella, P. Procel, Z. Vroon, and M. Zeman, "Optical study of back-contacted CIGS solar cells," *Optics Express*, vol. 27, no. 8, A269, 2019. doi: 10.1364/oe.27.00a269.
3. **N. Rezaei**, O. Isabella, Z. Vroon, and M. Zeman, "Optical optimization of a multi-layer wideband anti-reflection coating using porous MgF_2 for sub-micron thick CIGS solar cells," *Solar Energy*, vol. 177, no. August 2018, pp. 59–67, 2019. doi: 10.1016/j.solener.2018.11.015.
4. **N. Rezaei**, O. Isabella, Z. Vroon, and M. Zeman, "Quenching Mo optical losses in CIGS solar cells by a point contacted dual-layer dielectric spacer: a 3-D optical study," *Optics Express*, vol. 26, no. 2, A39, Jan. 2018. doi: 10.1364/OE.26.000A39.
5. O. Isabella, R. Vismara, A. Ingenito, **N. Rezaei**, and M. Zeman, "Decoupled front/back dielectric textures for flat ultra-thin c-Si solar cells," *Optics Express*, vol. 24, no. 6, A708-A719, 2016. doi: 10.1364/OE.24.00A708.

Oral presentations at conferences

1. **N. Rezaei**, P. Procel, M. Simor, Z. Vroon, O. Isabella and M. Zeman, "Submicron CIGS solar cells: feasibly towards the absorption limit," in *36th European PV Solar Energy Conference and Exhibition*, Marseille, France, September 2019.
2. **N. Rezaei**, O. Isabella, P. Procel, Z. Vroon and M. Zeman, "An optical study of back contacted CIGS solar cells," in *The OSA Light, Energy and the Environment Congress*, Sentosa Island, Singapore, November 2018.
3. **N. Rezaei**, O. Isabella, P. Procel, Z. Vroon and M. Zeman, "Hybrid opto-electrical modelling of advanced light management techniques in ultra-thin CIGS solar cells," in *E-MRS Spring Meeting*, Strasbourg, France, June 2018.
4. **N. Rezaei**, O. Isabella, Z. Vroon and M. Zeman, "Optical optimization of a wideband antireflection coating using porous MgF_2 for ultrathin CIGS solar cells," in *SPIE Photonics Europe*, Strasbourg, France, April 2018.
5. **N. Rezaei**, O. Isabella and M. Zeman, "Optical analysis of dielectric spacers for quenching Mo losses in CIGS solar cells," in *The OSA Light, Energy and the Environment Congress*, Leipzig, Germany, November 2016.

Poster presentations at conferences

1. **N. Rezaei**, P. Procel, M. Simor, Z. Vroon, **O. Isabella** and M. Zeman, "Numerical study and design of back-contacted CIGS solar cells," in *29th International Photovoltaic Science and Engineering Conference (PVSEC-29)*, Xi'an, China, November 2019.
2. R. Santbergen, C.R. Tobon, P. Procel, M. Singh, **N. Rezaei**, A. Calcabrini, M. Zeman and O. Isabella "ASA Software for Opto-Electrical Simulation of Silicon, CIGS and Perovskite Solar Cells," in *29th International Photovoltaic Science and Engineering Conference (PVSEC-29)*, Xi'an, China, November 2019.
3. **N. Rezaei**, P. Procel, M. Simor, Z. Vroon, **O. Isabella** and M. Zeman, "Numerical study and design of back-contacted CIGS solar cells," in *Sunday*, Bussum, the Netherlands, November 2019.
4. **N. Rezaei**, O. Isabella, P. Procel, Z. Vroon, and M. Zeman, "Optical optimization of CIGS solar cells based on rear dual-layer dielectric spacer and point-contact scheme," in *Sunday*, Bussum, the Netherlands, November 2017.
5. **N. Rezaei**, O. Isabella, Z. Vroon and M. Zeman, "Optical optimization of CIGS solar cells based on rear dual-layer dielectric spacer and point-contact scheme," in *33rd European PV Solar Energy Conference and Exhibition*, Amsterdam, the Netherlands, September 2017.
6. A.J. Blanker, **N. Rezaei**, Z. Vroon, A. Illiberi, O. Isabella, A.H.M. Smets and M. Zeman, "Advances Towards Ultra-thin CIGS PV solar cells," in *Sunday*, Veldhoven, the Netherlands, November 2016.

Curriculum Vitae

Nasim Rezaei was born in Iran on 23 April 1989. In 2011, she received her B.Sc. degree in Electrical, Electronics Engineering from Shiraz university, Shiraz, Iran. She continued her studies at Shiraz University with an M.Sc. degree in Electrical, Communications Engineering, where she performed research on optical fiber sensors. In 2016, she joined the Photovoltaic Materials and Devices group at Delft University of Technology to obtain her doctorate degree. The focus of her PhD project was light management in copper indium gallium (di)selenide (CIGS) solar cells, using optical as well as electrical modelling.

Contact

Email: nasim.rezaei89@gmail.com

LinkedIn: <https://www.linkedin.com/in/nasim-rezaei-527716190/>